Inviscid Disturbance Dynamics in Barotropic Shear Flows

Gerald B. Smith, II and Michael T. Montgomery

Research Supported by the Office of Naval Research
Grant # ONR N00014-93-1-0456
And by the National Science Foundation
Grant # NSF ATM-9312655.

Colorado State University

DEPARTMENT OF ATMOSPHERIC SCIENCE

PAPER NO. 561

INVISCID DISTURBANCE DYNAMICS IN BAROTROPIC SHEAR FLOWS

Gerald B. Smith, II and Michael T. Montgomery

Research Supported by the Office of Naval Research grant # ONR N00014-93-1-0456 and by the National Science Foundation grant # NSF ATM-9312655

Principal Investigator: Michael T. Montgomery

Department of Atmospheric Science

Colorado State University

Fort Collins, CO 80523

June 1994

Atmospheric Science Paper No. 561

ABSTRACT

INVISCID DISTURBANCE DYNAMICS IN BAROTROPIC SHEAR FLOWS

The inviscid nature of disturbance evolution in shear flows is investigated as an initial-value problem within the framework of nondivergent vorticity dynamics. To ensure a basic understanding of physical processes, disturbance evolution is first considered in a rectilinear system of simple shear. Particular emphasis is placed on identifying how the disturbance evolution depends on the zonal wavenumber and on the meridional structure of the initial conditions.

Insight acquired from the rectilinear problem is then applied to a bounded Rankine vortex. Here, the dependency of disturbance evolution on the azimuthal wavenumber is of special interest. Recent development of a low-frequency balance theory for rapidly rotating vortices has provided observational evidence that the low azimuthal wavenumber asymmetries, especially wavenumber one, are dominant in the near-vortex region. The results of this work provide further theoretical evidence of an inviscid wavenumber selection mechanism that preferentially damps the higher wavenumber asymmetries.

The radial structure and location of the initial conditions are found to be critical factors in determining how rapidly a disturbance is compressed or elongated. This in turn controls the rate of disturbance growth or decay. For swirling flows, a definition of an effective shear that accounts for both the radial variations in the initial conditions as well as the radial variation in the angular velocity is proposed. Using the reciprocal of this effective shear, time scales for a disturbance to decay to half its initial energy, the half-life time, are calculated for initial conditions and symmetric wind profiles that are found in hurricanes.

Simple shear flow and the bounded Rankine vortex do not admit discrete modal solutions since there is no mean state vorticity gradient to support them. The unbounded Rankine vortex is briefly considered in order to investigate how the presence of discrete neutral modes modifies the nonmodal solutions presented in this work.

ACKNOWLEDGEMENTS

We are indebted to many people for their support during the research, preparation, and writing of this work. We would especially like to thank the following individuals: Wayne Schubert, Michael Kirby, James Edwards, Randall Kallenbach, and John Persing. This work was sponsored by the National Science Foundation under grant ATM-9312655, by the Office of Naval Research under grant N00014-93-1-0456, and by the Air Force through the AFIT program. Numerical computations were performed using Hewlett Packard (HP) Apollo series computers belonging to the Montgomery Research Project. Programs were written in HP Fortran 9000.

TABLE OF CONTENTS

CHAPTER 1

INTRODUCTION

Intense vortices observed in the atmosphere and ocean exhibit a high degree of axisymmetry, although they are subject to persistent asymmetric forcing. In hurricanes, the interaction between the vortex and environmental asymmetries has implications for spiral band dynamics (Willoughby, 1977; Guinn and Schubert, 1993), intensification (or weakening) processes (Molinari, 1992), and storm motion (Shapiro and Ooyama, 1990; Shapiro, 1992; and Smith and Weber, 1993). Thus, understanding the asymmetric dynamics of intense vortices is critical for understanding the physical mechanisms controlling vortex evolution.

Until recently, the full primitive equations have been the favored tool for investigating the three-dimensional asymmetric dynamics of intense vortices. Formulation of a low-frequency balance theory, in which high-frequency gravity and inertial waves are filtered while retaining the pertinent aspects of advection, is complicated for rapidly rotating vortices since the time scale of the tangential advection is comparable to that of the gravity and inertial waves on the vortex. Shapiro and Montgomery (1993, hereafter SM) proposed a three-dimensional asymmetric balance (AB) theory that includes the full inertial effects of the rapidly rotating region while filtering the gravity and inertial waves. In the vortex environment, AB theory reduces to the quasi-geostrophic balance theory. In the absence of asymmetries, AB theory reduces to Eliassen's axisymmetric balance model (Eliassen, 1951) throughout the vortex.

SM were able to separate the advective processes from the inertial and gravity waves by defining a local Rossby number that accounted for the varying rotation in an intense vortex. This local Rossby number was given as the ratio of the orbital frequency to the inertial frequency multiplied by the azimuthal wavenumber. Based on observations from Hurricane Gloria (1985), SM showed that the square of the local Rossby number is generally less than unity only for wavenumber one

in the rapidly rotating region of an intense vortex. A goal in this work is to further explore the wavenumber selection mechanism that provides the basis for AB theory.

To aid in understanding the fundamental physical processes of axisymmetrization, previous works using quasi-geostrophic shallow water models and nondivergent barotropic models are now reviewed. Melander et al. (1987) studied the axisymmetrization in a quasi-geostrophic shallow water model using a pseudospectral formulation. The model was initialized using finite-amplitude elliptical vortices with modified 'tophat' radial profiles. In that paper, axisymmetrization was identified with the shedding of vorticity filaments outside the nearly axisymmetric vortex core. Rather than decompose the results into radial and azimuthal components, the vortex evolution was diagnosed by plotting the aspect ratio of vorticity isolines as a function of time. At early times (t less than a few orbital periods), all aspect ratios decreased towards unity and then began small-amplitude oscillations. Melander et al. identified this initial transition with axisymmetrization.

For the majority of cases they considered, representation of dissipative processes at small scales was parameterized using a hyperviscosity formulation in the potential vorticity evolution equation. This could conceivably have played a role in the axisymmetrization process. However, by increasing the value of the hyperviscosity used in their model, Melander et al. convincingly demonstrated the inviscid nature of the axisymmetrization process.

In a complementary approach, McCalpin (1987) used a reduced-gravity quasi-geostrophic model to study axisymmetrization in Gulf Stream rings. The vortex model consisted of finite-amplitude azimuthal mode 2 or mode 3 perturbations superposed on an axisymmetric Gaussian basic state. McCalpin found that nearly all of the perturbation energy was transferred to the basic state on time scales on the order of an orbital period. While only weakly dependent on the perturbation strength, the decay time scales were found to be strongly dependent on the strength of the mean flow and the azimuthal wavenumber. In particular, the decay time scale for wavenumber three was found to be 60% faster than that of wavenumber two.

Like Melander et al., McCalpin parameterized dissipative processes with a hyperviscosity formulation. However, he provided only a limited discussion regarding the effects of diffusion on the

symmetrization process. McCalpin calculated a diffusion time scale that appears to be based on L^4/A_B, where L is the characteristic horizontal scale and A_B is the hyperviscosity coefficient. For deformation radius scale waves, his diffusion time scale was found to be 80 years. However, since the differential rotation in the vortex rapidly reduces the radial scale of the asymmetries (SM; also Sutyrin, 1989), one must not neglect this effect when estimating the diffusion time scale.

In terms of McCalpin's model parameters, an estimate of the diffusion time scale that incorporates the differential rotation is

$$t_d \sim \frac{1}{A_B[(4\pi^2 m^2 n^2 + n^2)/r^2]^2} \qquad (B1.1)$$

where m is the number of orbits traversed by a fluid parcel at the radius of maximum winds (r) and n is the azimuthal wavenumber. For $A_B = 5 \times 10^9$ m^{4}s^{-1}, $m = 1$, $n = 2$, and $r = 50$ km, t_d is found to be approximately 13 hours. In calculating t_d, it is assumed that the differential rotation has already decreased the radial scale of an asymmetry to render basic state quantities effectively constant in a first approximation. Based on the results of Melander et al., this occurs in roughly a few orbital periods. For a typical run, McCalpin found the perturbation decay time scale to be 1.5 orbital periods. This suggests that any viscous influence was likely insignificant.

Both McCalpin and Melander et al. simulated asymmetric vortex evolution using fully nonlinear numerical models that generally prevent analytical solutions. While their results represent important and meaningful contributions to our understanding of axisymmetrization, basic physical processes may be masked by the presence of nonlinear dynamics, diffusion, and the β-effect.

Sutyrin (1989) developed a formal solution for linear disturbance evolution in a quasi-geostrophic shallow water model on an f-plane. In this model, the disturbance potential vorticity was conserved following fluid particles. For regions where the basic state potential vorticity was identically zero, Sutyrin showed that the nonmodal component of the disturbance potential vorticity became oscillatory in radius with the oscillations controlled by the differential rotation of the fluid. In addition, the radial gradient of the nonmodal disturbance potential vorticity was shown to increase linearly with time. Sutyrin asserted that a similar nonmodal disturbance evolution would be observed in regions with a continuous and monotonic basic state potential vorticity profile.

The linear increase with time of the nonmodal disturbance potential vorticity gradient was fundamentally due to the reduction of the radial scale of the disturbance. Sutyrin concluded, then, that the symmetrization process was due to the differential rotation of the fluid and was analogous to perturbation decay in rectilinear simple shear flow (Case, 1960).

Like Melander et al., Sutyrin did not examine the possibility of an inviscid azimuthal wavenumber selection mechanism nor did he investigate the energy transfer between the asymmetries and the circularly symmetric basic state. Identification of these processes is complicated in Sutyrin's model since the solution is expressed in terms of an infinite function space operator.

Carr and Williams (1989, hereafter CW) studied axisymmetrization using an inviscid nondivergent barotropic vortex model. Their evolutionary model consisted of small-amplitude perturbations superposed on a steady axisymmetric Rankine flow. CW were primarily interested in the asymmetry inducing influences of β and environmental wind shear.

CW asserted that the damping rate of perturbations is proportional to the square of the azimuthal wavenumber. This conclusion was based on results derived from initial conditions in which both the azimuthal wavenumber and the radial structure changed simultaneously. CW asserted further that their result was analogous to the dependence of damping on the zonal wavenumber as described by Case for plane Couette flow. However, a careful review of Case did not reveal any discussion of how the perturbation damping rate and the zonal wavenumber are related. Since this relationship is potentially a fundamental aspect of an inviscid wavenumber selection mechanism in sheared flows, both Case and CW must be revisited to clarify this issue.

In this work, the axisymmetrization process will be studied as an initial-value problem within the framework of inviscid nondivergent vorticity dynamics. Since the curvature vorticity and the curvilinear coordinate system of the swirling problem may complicate understanding of the disturbance dynamics, the analogous rectilinear simple shear problem (Case; also Farrell, 1987) will be examined first. Identification of how the disturbance evolution depends on the zonal wavenumber and the meridional structure of the initial condition will be emphasized.

CHAPTER 2

ALGEBRAIC INSTABILITY IN UNBOUNDED SIMPLE SHEAR

2.1 Introduction

The purpose of this chapter is to examine the evolution of small-amplitude perturbations in simple shear as a first step in the understanding the evolution of asymmetries in a hurricane. Of particular interest is how the perturbation evolution depends on the zonal wavenumber and the meridional structure of an initial vorticity profile. The flow is assumed unbounded and the model employed is the two-dimensional inviscid Euler equations on an f-plane. Since the model is ultimately formulated at the level of the vorticity equation, the Coriolis parameter does not affect interpretation of results, but is retained for consistency with later chapters.

Linear perturbation theory is used to decompose the flow into a meridionally varying basic state and small perturbation field. Ultimately, the results of this chapter are extended to hurricanes. Since observations show that the asymmetric winds in hurricanes are small compared to the symmetric tangential wind (SM), the use of linear perturbation theory is justified on observational grounds.

2.2 Rectilinear Shear Model

The zonal and meridional momentum equations and continuity equation in Cartesian coordinates are, respectively,

$$\frac{\partial u}{\partial t} + u\frac{\partial u}{\partial x} + v\frac{\partial u}{\partial y} - fv = -\frac{\partial p}{\partial x}, \tag{2.1a}$$

$$\frac{\partial v}{\partial t} + u\frac{\partial v}{\partial x} + v\frac{\partial v}{\partial y} + fu = -\frac{\partial p}{\partial y}, \tag{2.1b}$$

$$\frac{\partial u}{\partial x} + \frac{\partial v}{\partial y} = 0, \tag{2.1c}$$

where x and y are the zonal and meridional coordinates, u and v are the zonal and meridional winds, f is the constant Coriolis parameter, and p is the pressure divided by constant density. The Coriolis

parameter and pressure may be removed as explicit variables by taking the horizontal curl of the momentum equations to give

$$\frac{\partial \zeta}{\partial t} + u\frac{\partial \zeta}{\partial x} + v\frac{\partial \zeta}{\partial y} = 0, \tag{B2.2}$$

where

$$\zeta = \frac{\partial v}{\partial x} - \frac{\partial u}{\partial y} \tag{B2.3}$$

is the vertical component of the vorticity. Equation ($B2.2$) states that the vorticity is conserved following fluid particles.

Perturbations are brought out explicitly by letting $u = \bar{u}(y) + u'$, $v = v'$, and $p = \bar{p} + p'$, where an overbar denotes the basic state and a prime denotes a perturbation. Neglecting products of primed quantities, the equations of motion and the vorticity equation become

$$\frac{\partial u'}{\partial t} + \bar{u}\frac{\partial u'}{\partial x} + v'\frac{d\bar{u}}{dy} - fv' = -\frac{\partial \bar{p}}{\partial x} - \frac{\partial p'}{\partial x}, \tag{2.4a}$$

$$\frac{\partial v'}{\partial t} + \bar{u}\frac{\partial v'}{\partial x} + f\bar{u} + fu' = -\frac{\partial \bar{p}}{\partial y} - \frac{\partial p'}{\partial y}, \tag{2.4b}$$

$$\frac{\partial u'}{\partial x} + \frac{\partial v'}{\partial y} = 0, \tag{2.4c}$$

$$\frac{\partial \zeta'}{\partial t} + \bar{u}\frac{\partial \zeta'}{\partial x} + v'\frac{d\bar{\zeta}}{dy} = 0. \tag{2.4d}$$

Since the basic state alone must be a solution to (2.1), the momentum equations ($2.1a$, b) give

$$\frac{\partial \bar{p}}{\partial x} = 0, \tag{2.5a}$$

$$f\bar{u} = -\frac{\partial \bar{p}}{\partial y}, \tag{2.5b}$$

while the continuity equation ($B2.1c$) and the vorticity equation ($B2.2$) are trivially satisfied. After cancelling the basic state contributions, the linearized system (2.4) becomes

$$\frac{\partial u'}{\partial t} + \bar{u}\frac{\partial u'}{\partial x} + v'\frac{d\bar{u}}{dy} - fv' = -\frac{\partial p'}{\partial x}, \tag{2.6a}$$

$$\frac{\partial v'}{\partial t} + \bar{u}\frac{\partial v'}{\partial x} + fu' = -\frac{\partial p'}{\partial y}, \tag{2.6b}$$

$$\frac{\partial u'}{\partial x} + \frac{\partial v'}{\partial y}, = 0, \tag{2.6c}$$

$$\frac{\partial \zeta'}{\partial t} + \bar{u}\frac{\partial \zeta'}{\partial x} + v'\frac{d\bar{\zeta}}{dy} = 0. \tag{2.6d}$$

For simple shear flow, the basic state wind is given by $\bar{u} = Sy$ where S is a constant shear (see figure 2.1). The basic state vorticity is then

$$\bar{\zeta} = -\frac{d\bar{u}}{dy} = -S. \tag{B2.7}$$

The equations of motion (2.6a)-(2.6c) become

$$\frac{\partial u'}{\partial t} + Sy\frac{\partial u'}{\partial x} + (S - f)v' = -\frac{\partial p'}{\partial x}, \tag{2.8a}$$

$$\frac{\partial v'}{\partial t} + Sy\frac{\partial v'}{\partial x} + fu' = -\frac{\partial p'}{\partial y}, \tag{2.8b}$$

$$\frac{\partial u'}{\partial x} + \frac{\partial v'}{\partial y} = 0, \tag{2.8c}$$

while the vorticity equation (2.6d) is

$$\frac{\partial \zeta'}{\partial t} + Sy\frac{\partial \zeta'}{\partial x} = 0. \tag{B2.9}$$

The linearized vorticity equation (B2.9) states that the perturbation vorticity is conserved following the basic state flow.

For notational simplicity, primes are now dropped. All quantities are understood to be perturbations unless they have an overbar. Boundary conditions must be specified before (B2.9) can be solved. In an infinite domain, u and v be must be bounded as $|x|$ or $|y|$ becomes arbitrarily large.

To satisfy continuity (B2.8c), a perturbation streamfunction may be defined such that

$$u = -\frac{\partial \psi}{\partial y}, \qquad v = \frac{\partial \psi}{\partial x}. \tag{B2.10}$$

Equation (B2.3) becomes

$$\zeta = \nabla^2 \psi \tag{B2.11}$$

where the Laplacian operator is defined by

$$\nabla^2 = \left(\frac{\partial^2}{\partial x^2} + \frac{\partial^2}{\partial y^2}\right). \tag{B2.12}$$

Equation (B2.9) is thus

$$\left(\frac{\partial}{\partial t} + Sy\frac{\partial}{\partial x}\right)\left(\frac{\partial^2}{\partial x^2} + \frac{\partial^2}{\partial y^2}\right)\psi = 0. \tag{B2.13}$$

There are several methods that can be used to solve ($B2.13$). The normal mode and initial-value approaches are considered below.

2.3 The Normal Mode Approach

In the normal mode approach, separable solutions of the form

$$\psi(x,y,t) = \Psi(y)e^{i(kx+\sigma t)} \tag{$B2.14$}$$

are assumed where k is a real zonal wavenumber, σ is the eigenfrequency, and $\Psi(y)$ is the eigenfunction. Substituting ($B2.14$) into ($B2.13$) and dividing out the common exponential term yields

$$(\sigma + kSy)\left(\frac{d^2}{dy^2} - k^2\right)\Psi = 0. \tag{$B2.15$}$$

If the factor $\sigma + kSy$ is naively divided out, then ($B2.15$) has a solution of the form

$$\Psi = c_1 e^{ky} + c_2 e^{-ky}. \tag{$B2.16$}$$

The boundary conditions for ($B2.16$) require that Ψ be bounded as $y \to \pm\infty$. The only way to satisfy these conditions is if $c_1 = c_2 = 0$. Thus, there are no normal modes associated with $\sigma + kSy \neq 0$ and the naive conclusion is that there are only trivial solutions to the problem. To see why this is incorrect, note that ($B2.15$) may also be satisfied if $\sigma + kSy = 0$. At such points, more information is needed to integrate ($B2.15$) for Ψ.

2.4 The Initial-Value Approach

An alternate solution strategy follows the methodology of Case (1960). Since the basic state flow only depends on y, the zonal dependence may be represented by a Fourier integral. The Fourier transform pair is given by

$$\hat{f}(k) = \int_{-\infty}^{\infty} f(x)e^{-ikx}\,dx, \tag{2.17a}$$

$$f(x) = \frac{1}{2\pi}\int_{-\infty}^{\infty} \hat{f}(k)e^{ikx}\,dk, \tag{2.17b}$$

where k is the zonal wavenumber. Examination of the initial-value problem associated with (B2.13) is of interest. This problem is formulated by using the Laplace transform pair, which is given by

$$f^{(q)}(q) = \int_0^\infty f(t)e^{-qt}\,dt, \tag{2.18a}$$

$$f(t) = \frac{1}{2\pi i}\oint_C f^{(q)}(q)e^{qt}\,dq, \tag{2.18b}$$

where q is the Laplace transform parameter (generally complex) and C denotes a line parallel to the imaginary axis that is positioned to the right of all singularities of $f^{(q)}(q)$.

The Fourier transform of (B2.13) is

$$\left(\frac{\partial}{\partial t} + ikSy\right)\left(\frac{\partial^2}{\partial y^2} - k^2\right)\hat{\psi} = 0 \tag{B2.19}$$

while the Laplace transform of (B2.19) is

$$(q + ikSy)\left(\frac{d^2}{dy^2} - k^2\right)\hat{\psi}^{(q)} = \left(\frac{d^2}{dy^2} - k^2\right)\hat{\psi}_o. \tag{B2.20}$$

The variable $\hat{\psi}_o$ is the meridional structure of the initial streamfunction for wavenumber k and the right side of (B2.20) is the initial vorticity. On dividing through by $(q + ikSy)$, equation (B2.20) may be written as

$$\left(\frac{\partial^2}{\partial y^2} - k^2\right)\hat{\psi}^{(q)} = \frac{\hat{\zeta}_o}{q + ikSy}. \tag{B2.21}$$

Noting that the Laplace transform of $\exp(-ikSyt)$ is $1/(q + ikSy)$, the inverse Laplace transform of (B2.21) is

$$\left(\frac{\partial^2}{\partial y^2} - k^2\right)\hat{\psi} = \hat{\zeta}_o e^{-ikSty}. \tag{B2.22}$$

The boundary conditions require that $\hat{\psi}$ be bounded as $|y| \to \infty$. Recalling the σ parameter from the normal mode approach, it is seen that $\sigma = -kSy$, or $\sigma + kSy = 0$. Unlike the separable normal mode solutions which maintain a constant structure in time, the initial-value problem has a time dependent meridional structure.

The differential equation (B2.22) is readily solved by the Green's function method. The Green's function is defined as the solution to

$$\left(\frac{\partial^2}{\partial y^2} - k^2\right)G(y, y_o) = \delta(y - y_o) \tag{B2.23}$$

where $\delta(y - y_o)$ is the Dirac delta function and $G(y, y_o)$ is bounded as $|y| \to \infty$. Using the one-dimensional form of Green's Identity, the solution to $(B2.22)$ is then

$$\hat{\psi}(k, y_o, t) = \int_{-\infty}^{\infty} G(y, y_o)\hat{\zeta}_o(k, y)e^{-ikSty}\, dy. \tag{B2.24}$$

The Green's function is now determined. For $y \neq y_o$, equation $(B2.23)$ is homogeneous and the general solution in each region is

$$G(y, y_o) = \begin{cases} Ae^{|k|y} + Ce^{-|k|y}, & y < y_o \\ De^{|k|y} + Be^{-|k|y}, & y > y_o. \end{cases} \tag{B2.25}$$

For simplicity, only the case $k \geq 0$ will be treated explicitly. Applying boundedness at infinity gives

$$G(y, y_o) = \begin{cases} Ae^{ky}, & y < y_o \\ Be^{-ky}, & y > y_o \end{cases}. \tag{B2.26}$$

Two other conditions are needed to uniquely define $G(y, y_o)$. Since $\hat{\psi}$ is continuous, the Green's function is required to be continuous at $y = y_o$. The second condition is found by integrating $(B2.23)$ over a small interval about y_o. This yields

$$\int_{y_o-\epsilon}^{y_o+\epsilon} \frac{\partial^2 G}{\partial y^2}(y, y_o)\, dy - k^2 \int_{y_o-\epsilon}^{y_o+\epsilon} G(y, y_o)\, dy = \int_{y_o-\epsilon}^{y_o+\epsilon} \delta(y - y_o)\, dy \tag{B2.27}$$

which becomes

$$\frac{\partial G}{\partial y}(y_o + \epsilon, y_o) - \frac{\partial G}{\partial y}(y_o - \epsilon, y_o) - k^2 \int_{y_o-\epsilon}^{y_o+\epsilon} G(y, y_o)\, dy = 1. \tag{B2.28}$$

Since $G(y, y_o)$ is a bounded function on the integration interval, the integral in $(B2.28)$ vanishes as ϵ goes to zero, yielding the jump condition

$$\frac{\partial G}{\partial y}(y_o^+, y_o) - \frac{\partial G}{\partial y}(y_o^-, y_o) = 1. \tag{B2.29}$$

The Green's function is now uniquely determined by imposing the continuity and jump conditions on $(B2.26)$, giving

$$G(y, y_o) = -\frac{1}{2k} \begin{cases} e^{k(y-y_o)}, & y \leq y_o \\ e^{-k(y-y_o)}, & y \geq y_o \end{cases}. \tag{B2.30}$$

Since $G(y, y_o) = G(y_o, y)$, equation $(B2.24)$ may be written as

$$\hat{\psi}(k, y, t) = \int_{-\infty}^{\infty} G(y, y_o)\hat{\zeta}_o(k, y_o)e^{-ikSty_o}\, dy_o. \tag{B2.31}$$

Equation (B2.31) is referred to as the continuous spectrum solution to equation (B2.13) since it results from integrating over all advective frequencies $-ik\bar{u}(y_o)$ spanned by the flow.

The solution is completed by applying the inverse Fourier transform, yielding

$$\psi(x,y,t) = \frac{1}{2\pi}\int_{-\infty}^{\infty} e^{ikx}\int_{-\infty}^{\infty} G(y,y_o)\hat{\zeta}_o(k,y_o)e^{-ikSy_o t}\,dy_o\,dk. \qquad (B2.32)$$

In this chapter and the next, attention is restricted to initial vorticity perturbations of the form $f(y)e^{ik_*x}$ where k_* is a pre-specified wavenumber. The Fourier transform of this initial condition is $\hat{f}(y)\delta(k_*-k)$, where $\delta(k_*-k)$ is again the Dirac delta function. When an initial condition of this form is substituted into (B2.32) and the integration is performed, the delta function maps every k into k_*. For simplicity, the delta function will not be explicit in any of the subsequent manipulations and k will be used to refer to the wavenumber in both physical and spectral space. With the above convention, the solution (B2.32) is written as

$$\psi_k(x,y,t) = \int_{-\infty}^{\infty} G(y,y_o)\hat{\zeta}_o(k,y_o)e^{ik(x-Sy_o t)}\,dy_o. \qquad (B2.33)$$

In (B2.33), the subscript k is a reminder that the delta function has filtered a particular wavenumber from the inverse Fourier transform integral.

Before examining the specific evolution of the perturbation streamfunction for various initial vorticity profiles, recall that the problem is inviscid. Thus, all processes are time-reversible. The convention will be to define $t=0$ as the initial time, $t>0$ as future times, and $t<0$ as past times.

2.5 The Plane Wave

In an infinite domain, a natural choice for an initial condition is one that is periodic. Let

$$\hat{\psi}_o = e^{il_o y} \qquad (B2.34)$$

where l_o is the initial meridional wavenumber. The initial vorticity is then

$$\hat{\zeta}_o = -(k^2+l_o^2)e^{il_o y}. \qquad (B2.35)$$

Substituting (B2.35) into (B2.33) and integrating yields

$$\psi_k = \frac{k^2+l_o^2}{k^2+(l_o-kSt)^2}\,e^{i[kx+(l_o-kSt)y]}. \qquad (B2.36)$$

Taking the real part of (B2.36) gives

$$\psi_k = \frac{k^2 + l_o^2}{k^2 + (l_o - kSt)^2} \cos[kx + (l_o - kSt)y]. \qquad (B2.37)$$

The quantity $l_o - kSt$ is a time dependent meridional wavenumber, l, which describes the ever-changing amplitude and meridional structure of the perturbation. The meridional wavenumber and time are negatively related so as t increases l decreases.

As an aid to understanding the evolution of the physical fields, consider the wave vector $\vec{m} = (k, l)$. The magnitude of the wave vector, $|\vec{m}|$, is the total wavenumber of the perturbation. The angle the wave vector makes with the zonal axis (measured in a counter clockwise sense from the positive x axis) is given by $\theta = \tan^{-1}(l/k)$. The wave vector is perpendicular to the perturbation contours, so θ ranges from $-\pi/2$ to $\pi/2$.

The streamfunction evolution described by (B2.37) is qualitatively considered for fixed k and l_o. The maximum streamfunction amplitude is $(k^2 + l_o^2)/k^2$ and occurs when $t = l_o/kS$ ($l = 0$). Thus, the streamfunction amplitude grows when $t < l_o/kS$ ($l > 0$) and it decays for $t > l_o/kS$ ($l < 0$). When the streamfunction amplitude is maximum, the streamfunction field is parallel to the meridional axis and the number of waves in the domain is given by k. Since t and l are negatively related, increasing t results in decreasing θ, so the streamfunction field rotates clockwise. However, increasing (decreasing) t results in $|\vec{m}|$ decreasing (increasing) when $t < l_o/kS$ ($t > l_o/kS$). Thus, when the streamfunction field is in the growth (decay) phase, the number of waves in the domain decreases (increases).

Figure 2.2 shows streamfunction contours for $k = l_o = 1$ at nondimensional times St = -10.0, -1.0, 1.0, and 10.0. When the streamfunction field is in the growth phase, the contours have a negative slope. When the streamfunction field is in the decay phase, the contours have a positive slope. The shear for this problem is positive and, thus, has a positive slope (figure 2.1). Comparing the slope of the streamfunction contours with the slope of the shear, the streamfunction field tilts against the shear in the growth phase while the streamfunction field tilts with the shear in the decay phase. When the streamfunction field is upright, its amplitude is maximum.

To further quantify the growth and decay, an expression for the perturbation kinetic energy

(KE) density is derived. Substituting (B2.37) into (B2.10) gives the zonal and meridional winds for the plane wave streamfunction. These are

$$u_k = \frac{(l_o - kSt)(k^2 + l_o^2)}{k^2 + (l_o - kSt)^2} \sin[kx + (l_o - kSt)y], \tag{2.38a}$$

$$v_k = -\frac{k(k^2 + l_o^2)}{k^2 + (l_o - kSt)^2} \sin[kx + (l_o - kSt)y]. \tag{2.38b}$$

The KE density is then $\rho(u^2 + v^2)/2$, which gives

$$E_k = \frac{(k^2 + l_o^2)^2}{2[k^2 + (l_o - kSt)^2]} \sin^2[kx + (l_o - kSt)y] \tag{B2.39}$$

where ρ has been set to one.

Equation (B2.39) gives a local measure of the KE density. A more useful measure which isolates the temporal evolution of the disturbances is an integrated KE. For the plane wave, the integration is performed over one wavelength zonally and meridionally since the integrated KE density over the entire plane is infinite. The integration yields

$$\langle E_k \rangle = \frac{(k^2 + l_o^2)^2}{4[k^2 + (l_o - kSt)^2]} \tag{B2.40}$$

where $\langle E_k \rangle$ is the KE per wave. This is maximum when $l_o - kSt = 0$, which gives

$$\langle E_k \rangle_{\max} = \frac{(k^2 + l_o^2)^2}{4k^2}. \tag{B2.41}$$

Thus, the normalized KE per wave (hereafter, the normalized KE) is

$$\frac{\langle E_k \rangle}{\langle E_k \rangle_{\max}} = \frac{k^2}{k^2 + (l_o - kSt)^2}. \tag{B2.42}$$

The normalization has been done with the maximum value of the normalized KE rather than the initial value so that the normalized KE ranges from zero to one. From (B2.42), the instantaneous growth (decay) rate is found to be

$$\frac{1}{\langle E_k \rangle} \frac{d\langle E_k \rangle}{dt} = \frac{2kS(l_o - kSt)}{k^2 + (l_o - kSt)^2}. \tag{B2.43}$$

Setting the time derivative of (B2.43) to zero gives the maximum growth (decay) rate which occurs at $St = \mp 1 + l_o/k$. This corresponds to $l = \pm k$, $\theta = \pm \pi/4$, and a normalized KE of 0.5 for both times.

This suggests a natural evolution time-scale for the perturbation energy to decay to half its maximum energy, the half-life time. For the plane wave perturbation, the half-life time is $1/S$. Interestingly, this is independent of k and l_o. Figures 2.3 and 2.4 show the normalized KE and the growth (decay) rate as functions of time for $k = 1$, $l_o = 1$; $k = 1$, $l_o = 2$; and $k = 2$, $l_o = 1$. These figures clearly demonstrate that changing k and l_o merely shifts the energy curve along the time axis, but do not change the structure of the energy curve.

The half-life time for sheared disturbances in mid-latitude cyclones, hurricanes, and tornados may be estimated as follows. Letting U and L denote typical horizontal and temporal scales, the half-life time is $\sim L/U$. In moderate mid-latitude cyclones, $U \sim 10$ ms^{-1} and $L \sim 1000$ km giving a horizonatal shear of 10^{-5} s^{-1} and a half-life time of about 1 day. In the eyewall of a hurricane, $U \sim 50$ ms^{-1} and $L \sim 50$ km. Thus, the horizontal shear is 10^{-3} s^{-1} and the half-life time is about 15 minutes. Finally, in a tornado, $U \sim 100$ ms^{-1} and $L \sim 100$ m yielding a horizontal shear of 1 s^{-1} and a half-life time of 1 second. These numbers are only approximate, but they serve to illustrate how the strength of the shear affects the evolution time-scale.

Perturbation growth and decay imply an energy transfer to and from the disturbance. Understanding of this process is obtained by examining the perturbation kinetic energy equation, which is formed by taking the dot product of (u, v) with equations $(B2.8a)$ and $(B2.8b)$. This yields

$$\frac{\partial E}{\partial t} + \bar{u}\frac{\partial E}{\partial x} + uv\frac{d\bar{u}}{dy} = -\frac{\partial (up)}{\partial x} - \frac{\partial (vp)}{\partial y}. \qquad (B2.44)$$

Integrating over the perturbation domain gives

$$\frac{\partial \langle E \rangle}{\partial t} = -\int\int_A uv\frac{d\bar{u}}{dy}\,dxdy. \qquad (B2.45)$$

When the perturbation grows, the left side of $(B2.45)$ is positive. For positive shear, the momentum flux term is negative and perturbation zonal wind is fluxed equatorward. The effect, then, is that the shear decreases and the basic state provides energy for the perturbation's growth. When the perturbation decays, the left side of $(B2.45)$ is negative. Here, the momentum flux is positive and perturbation zonal wind is fluxed poleward. The effect is that the shear increases and the basic state strengthens at the expense of the perturbation.

From (B2.45) it is seen that the perturbation energy tendency is a nonlinear process since it depends on uv. Thus, the perturbation energy is not conserved in the linear problem and the basic state energy is viewed as an infinite reservoir. It can be shown from the nonlinear momentum equations, though, that the total energy in this system is conserved.

For the remainder of this work, attention is restricted to disturbance decay, so $l_o = 0$. The equations developed in this section become

$$\hat{\zeta}_o = -k^2, \tag{B2.46}$$

$$\zeta_k = -k^2 \cos[k(x - Sty)], \tag{B2.47}$$

$$\psi_k = \frac{1}{1 + (St)^2} \cos[k(x - Sty)], \tag{B2.48}$$

$$u_k = \frac{-kSt}{1 + (St)^2} \sin[k(x - Sty)], \tag{B2.49}$$

$$v_k = \frac{-k}{1 + (St)^2} \sin[k(x - Sty)], \tag{B2.50}$$

$$E_k = \frac{k^2}{1 + (St)^2} \sin^2[k(x - Sty)], \tag{B2.51}$$

$$\frac{\langle E_k \rangle}{\langle E_k \rangle_o} = \frac{1}{1 + (St)^2}, \tag{B2.52}$$

$$\frac{1}{\langle E_k \rangle} \frac{d\langle E_k \rangle}{dt} = \frac{-2S^2 t}{1 + (St)^2}. \tag{B2.53}$$

The upright plane wave initial condition is formally equivalent to a constant initial vorticity profile. Thus, perturbations forced by either constant or periodic initial conditions in simple shear flow have global energy evolutions that are independent of the zonal wavenumber k.

2.6 Gaussian Initial Condition

The plane wave considered in the previous section provides analytical solutions for the perturbation evolution in simple shear. However, transient atmospheric forcings are more realistically represented as isolated disturbances. To simulate a short wave trough, a Gaussian initial vorticity profile is considered. This is given by

$$\hat{\zeta}_o(y) = e^{-\alpha y^2} \tag{B2.54}$$

where $1/\sqrt{\alpha}$ defines the characteristic e-folding length scale of the Gaussian. Unlike the plane wave initial condition, when (B2.54) is substituted into (B2.33), there are no closed form solutions

available.

Using the trapezoidal rule to evaluate the integral, figures 2.5 and 2.6 plot streamfunction and vorticity contours, respectively, for the initial vorticity profile $\hat{\zeta}_o = \exp(-y^2)$. The rows show zonal wavenumbers $k = 1$, 2, and 3, respectively, while the columns denote nondimensional times $St =$ 0.0, 1.0, 2.0, respectively. There are several differences between the Gaussian and the upright plane wave cases. For a fixed time, the streamfunction amplitude decreases with increasing k. In addition, the figure suggests that that higher wavenumber perturbations decay faster than lower wavenumber perturbations. In the upright plane wave, the streamfunction amplitude and the decay rate were independent of the zonal wavenumber. Finally, there is a suggestion that for large time, the plane wave solution emerges.

As with the plane wave perturbation, a global measure of the KE is desired. Here, though, the meridional integration is from $-\infty$ to $+\infty$. Figure 2.7 shows the normalized KE as a function of time for the initial vorticity profile $\hat{\zeta}_o = \exp(-y^2)$. As indicated in figure 2.5, higher wavenumber perturbations decay more rapidly than lower wavenumber perturbations. In addition, for increasing k or t, the normalized KE curves asymptote to the plane wave solution. Interestingly, the wavenumber $k = 1$ perturbation decays much slower than all higher wavenumber perturbations. This would not be surprising in a viscous fluid. However, in the above results, the viscosity is identically zero yet higher wavenumber disturbances still decay faster than smaller wavenumber disurbances. This suggests a truly inviscid decay mechanism that rapidly damps the higher wavenumbers leaving the lower wavenumbers behind.

To gain further understanding of the zonal wavenumber dependence in the evolution of meridionally confined initial vorticity disturbances, it is instructive to examine the interaction of the three terms comprising the integrand of (B2.33). Figure 2.8 shows the Green's function, $G(y, y_o)$; the phase function, $\cos(kSty_o)$; their product; and the initial vorticity $\hat{\zeta}_o = \exp(-y_o^2)$ as functions of y_o for zonal wavenumber $k = 1$. Figure 2.9 is the same plot for zonal wavenumber $k = 3$. In the figures, the Green's function is only considered at $y = 0$ and the $-1/2k$ factor is ignored since it is constant in the integration. In addition, the time is chosen so that $St = 1$. As k increases, the

Green's function narrows while the phase function oscillates more rapidly. The effect of increasing k, then, is for the product of the Green's function and the phase function to become more meridionally confined. For large enough k, the meridional scale of this product is so small that the initial vorticity appears effectively constant in the integration. This is reminiscent of the upright plane wave solution in which the initial vorticity profile is constant in the integration. Thus, while the meridional scale of the initial vorticity generally introduces a dependence on the zonal wavenumber in the shear dynamics, for large k the plane wave solution should emerge.

For increasing k, the plane wave solution may be recovered from a meridionally confined initial condition. This can be demonstrated analytically as follows. The streamfunction amplitude in Fourier space is

$$\hat{\psi}(y) = \int_{-\infty}^{\infty} G(y, y_o)\hat{\zeta}_o(y_o)e^{-ikSty_o}\, dy_o. \qquad (B2.55)$$

As k becomes large, the streamfunction amplitude can be approximated by

$$\hat{\psi}(y) \approx \hat{\zeta}_o(y) \int_{-\infty}^{\infty} G(y, y_o)e^{-ikSty_o}\, dy_o \qquad 1 \ll k < \infty. \qquad (B2.56)$$

This integral may be evaluated exactly giving the approximate streamfunction amplitude

$$\hat{\psi} = -\frac{\hat{\zeta}_o(y)}{k^2[1 + (St)^2]}e^{-ikSty}. \qquad (B2.57)$$

Upon applying the inverse Fourier transform and taking the real part, $(B2.57)$ becomes

$$\psi_k = -\frac{\hat{\zeta}_o(y)}{k^2[1 + (St)^2]}\cos[k(x - Sty)], \qquad (B2.58)$$

so the meridional velocity is

$$v_k = \frac{\hat{\zeta}_o(y)}{k[1 + (St)^2]}\sin[k(x - Sty)]. \qquad (B2.59)$$

Now, the zonal velocity is

$$u_k = -\frac{d\hat{\zeta}_o(y)}{dy}\frac{\cos[k(x - Sty)]}{k^2[1 + (St)^2]} - \frac{\hat{\zeta}_o(y)St}{k[1 + (St)^2]}\sin[k(x - Sty)]. \qquad (B2.60)$$

Assuming k large enough but finite such that the first term on the right side of $(B2.60)$ is small compared to the second term, the zonal velocity becomes

$$u_k \approx -\frac{\hat{\zeta}_o(y)St}{k[1 + (St)^2]}\sin[k(x - Sty)]. \qquad (B2.61)$$

The KE density is then approximated by

$$E_k = \frac{\hat{\zeta}_o^2(y)}{k^2[1+(St)^2]} \sin^2[k(x-Sty)] \qquad (B2.62)$$

where the density, ρ, has been set to one, while the integrated KE is given by

$$\langle E_k \rangle = \frac{\pi}{2k^3[1+(St)^2]} \int_{-\infty}^{\infty} \hat{\zeta}_o^2(y)\, dy. \qquad (B2.63)$$

Normalizing ($B2.63$) by its initial value

$$\langle E_k \rangle_o = \frac{\pi}{2k^3} \int_{-\infty}^{\infty} \hat{\zeta}_o^2(y)\, dy, \qquad (B2.64)$$

gives the normalized KE for large k

$$\frac{\langle E_k \rangle}{\langle E_k \rangle_o} = \frac{1}{1+(St)^2}. \qquad (B2.65)$$

This is the normalized KE for the upright plane wave. A physical interpretation for the zonal wavenumber dependence is presented at the end of this section.

Figure 2.5 shows the plane wave solution emerging for large time. As time increases, the phase function oscillates more rapidly while the Green's function and initial condition remain unchanged. For sufficiently large times, the half-wavelength scale of the phase function is narrow enough so that the initial condition appears locally constant which is analogous to the upright plane wave. Further, double integration by parts of ($B2.55$) subject to the boundary conditions reveals the t^{-2} dependence of the streamfunction amplitude at large times.

Figures 2.10 and 2.11 plot perturbation streamfunction and vorticity contours, respectively, for zonal wavenumber $k = 1$. The rows show the fields for initial vorticity profiles $\hat{\zeta}_o = \exp(-\alpha y^2)$ where $\alpha = 1$, 2, and 3, respectively, while the columns denote the fields at nondimensional times St = 0.0, 1.0, and 2.0, respectively. Figure 2.12 plots the corresponding normalized KE as a function of time and shows that decreasing the meridional scale of the initial condition results in slower energy decay. Since the energy decay is related to the half-wavelength scale of the phase function, decreasing the scale of the initial condition increases the time required for a given amount of energy decay. Thus, small-scale disturbances asymptote to the plane wave solution more slowly than large-scale disturbances.

Physically, disturbance evolution is governed by the conservation of disturbance vorticity so the meridional change in the zonal wind across a disturbance controls how rapidly a vorticity disturbance is elongated. Because the area of a fluid element does not change in nondivergent flow, an elongating vorticity patch implies an attendant decrease in the disturbance meridional scale. The decrease in the meridional scale is directly related to the decrease in disturbance energy. Disturbances of large meridional extent are elongated more rapidly than those of small meridional extent and, thus, decay more rapidly. Since the plane wave solution spans the domain, its meridional length scale is effectively infinite. Therefore, the plane wave always decays more rapidly than any meridionally localized disturbance.

In a similar fashion, the dependence on the zonal wavenumber may be explained. For an initially upright disturbance, the zonal wavenumber is inversely related to the initial zonal extent of a disturbance. Consider two disturbances with the same initial energy and meridional extent where one disturbances has twice the initial zonal extent of the other. In a given amount of time, the zonal elongation of both disturbances is the same. To conserve area, the change in the meridional scale of a disturbance with large zonal extent is less than that of a disturbance with small zonal extent. Therefore, a lower wavenumber disturbance decays slower than a higher wavenumber disturbance.

2.7 Summary

The evolution of disturbances in unbounded simple shear flow has been examined as a first step in understanding the evolution of asymmetries in hurricanes. The system was formulated as an initial value problem and two types of initial conditions were considered. For the plane wave initial vorticity profile, the disturbance evolution was only a function of time and decayed as t^{-2}. Since transient atmospheric forcings are more realistically represented by isolated disturbances, Gaussian initial vorticity profiles were considered. Unlike the plane wave, the evolution of these perturbations depended on both the meridional scale and the zonal wavenumber of the initial condition. The meridional scale determined how rapidly the disturbance was elongated. Large-scale disturbances elongated and, subsequently, decayed more rapidly than small-scale disturbances. The dependence

of the evolution on the zonal wavenumber illustrated a truly inviscid mechanism associated with differential advection that favors the decay of small-scale disturbances over large-scale disturbances.

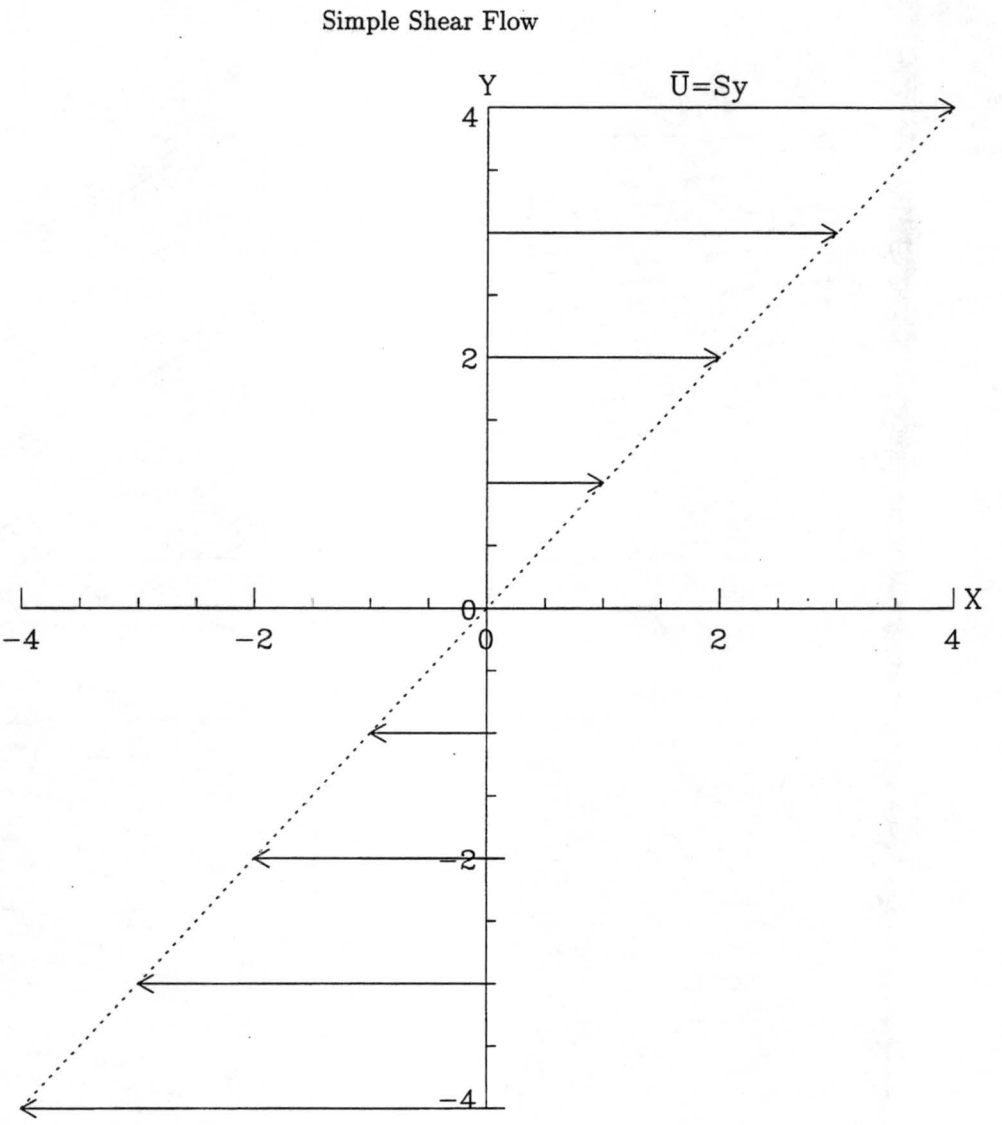

Fig. 2.1: Simple shear flow. Arrows show basic state zonal wind vectors, dashed line shows the shear ($S = 1$).

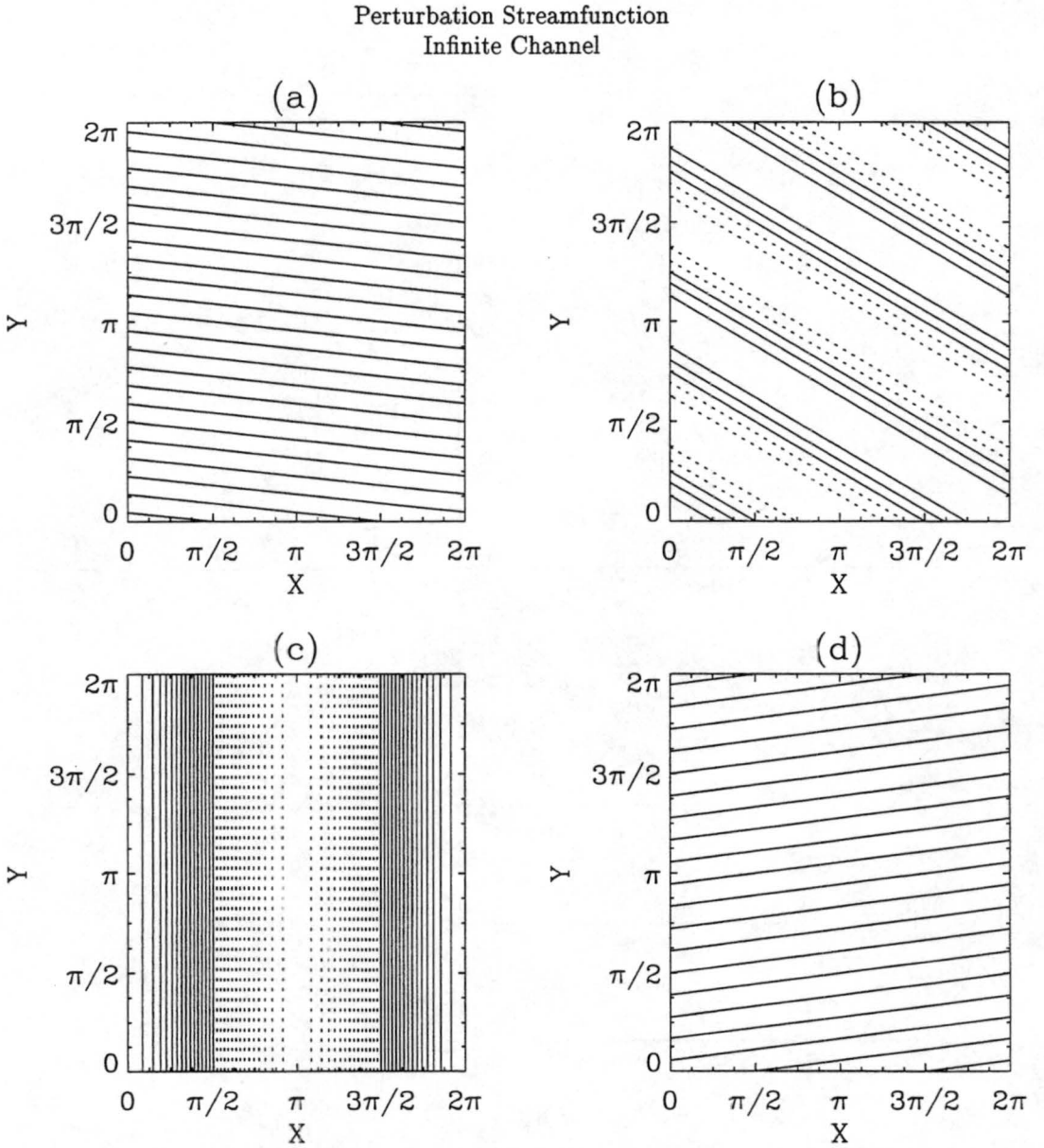

Fig. 2.2: Perturbation streamfunction for a plane wave initial vorticity profile with $k = l_o = 1$ and St = (a) -10.0, (b) -1.0, (c) 1.0, and (d) 10.0. The contour interval is 1.38×10^{-1} m^{2}s^{-1}. Solid lines denote $\psi \geq 0$, dotted lines $\psi < 0$.

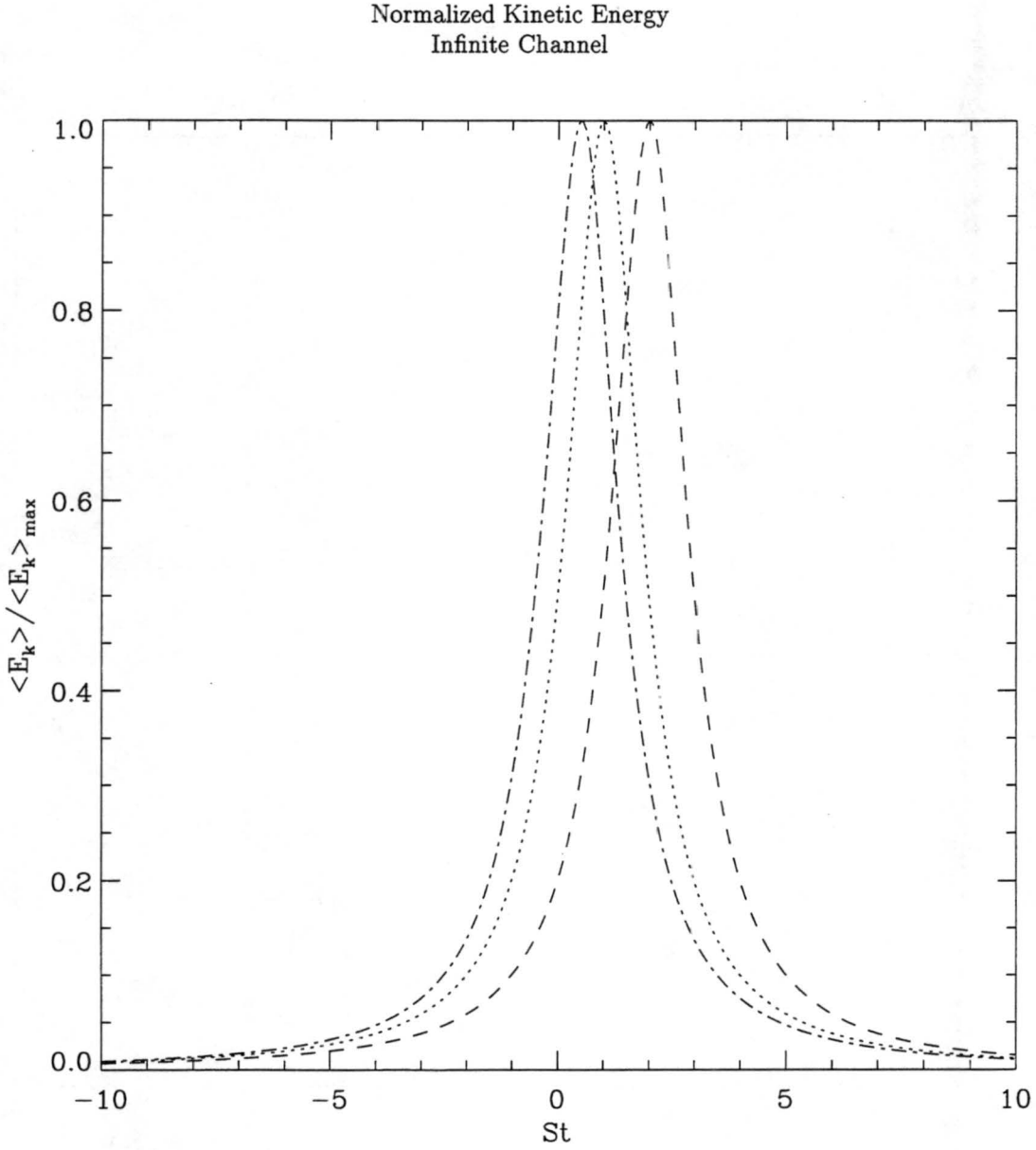

Fig. 2.3: Normalized kinetic energy for a plane wave initial vorticity profile with $k = 1$, $l_o = 1$ (dot); $k = 1$, $l_o = 2$ (dash); $k = 2$, $l_o = 1$ (dot dash).

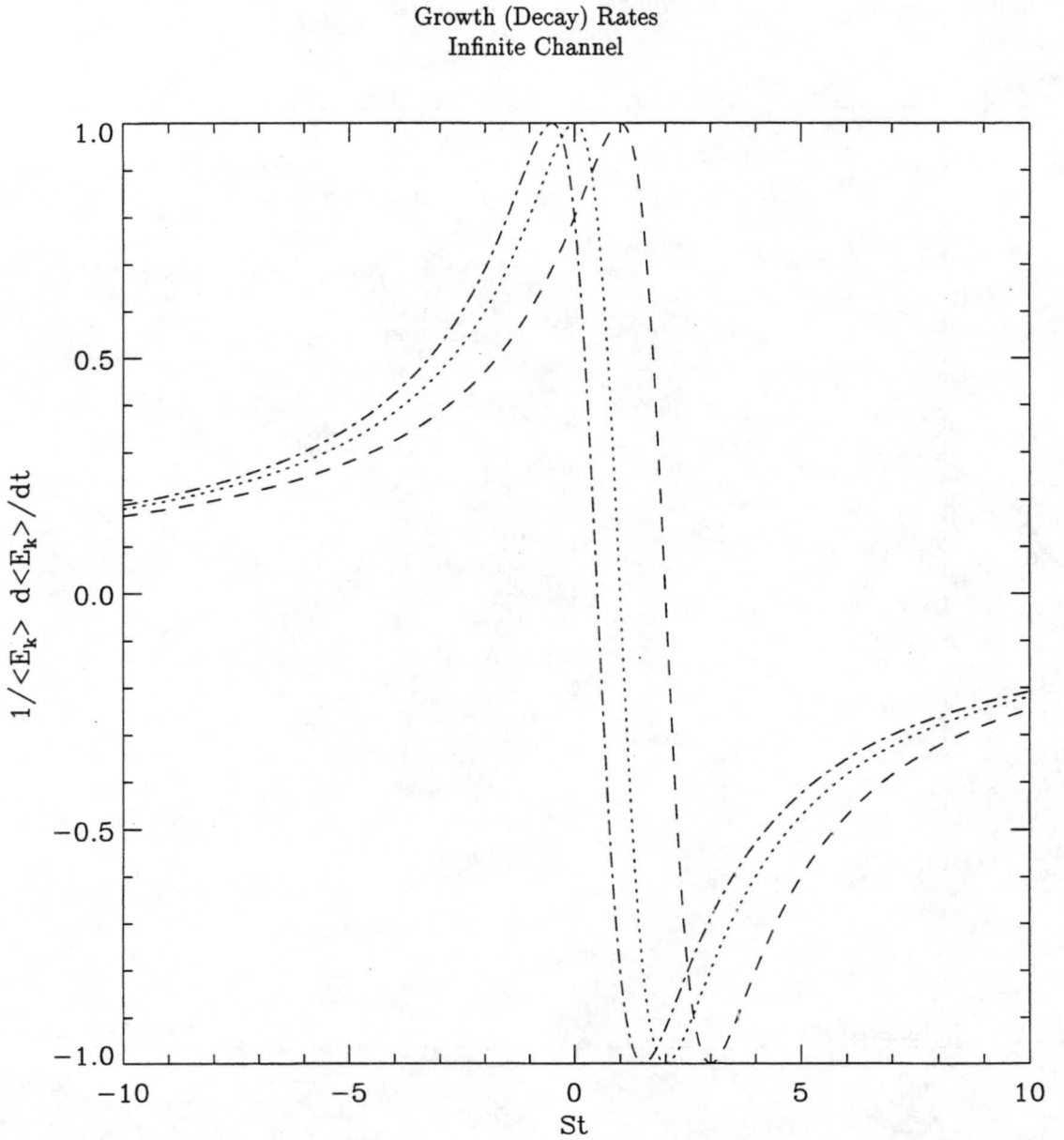

Fig. 2.4: Growth (decay) rates for a plane wave initial vorticity profile with $k = 1$, $l_o = 1$ (dot); $k = 1$, $l_o = 2$ (dash); $k = 2$, $l_o = 1$ (dot dash).

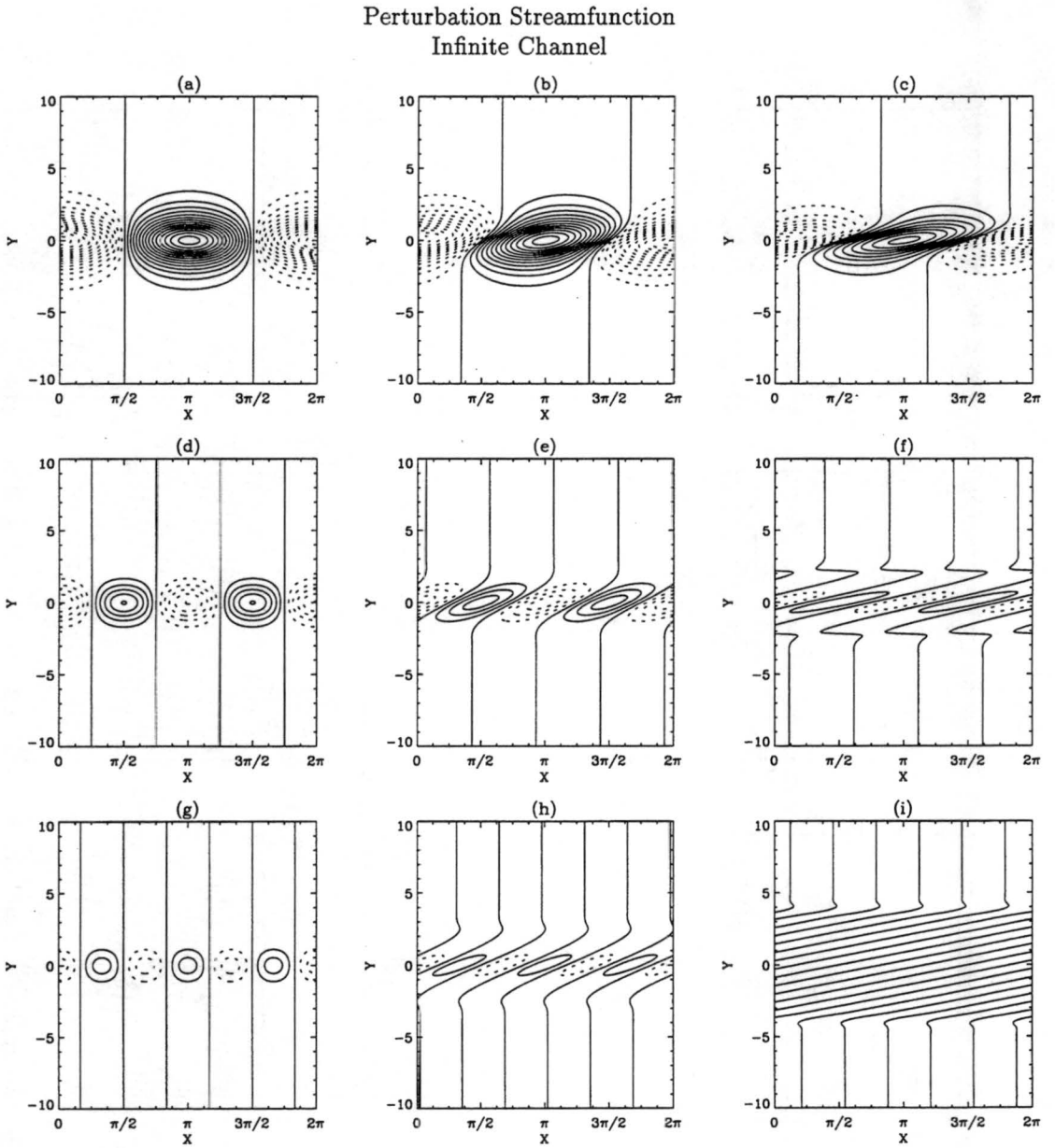

Fig. 2.5: Perturbation streamfunction for the Gaussian initial vorticity profile $\hat{\zeta}_o = \exp\left(-y^2\right)$. Panels (a)-(c) show contours for zonal wavenumber $k = 1$ at times $St = 0.0$, 1.0, and 2.0, respectively. Panels (d)-(f) show contours for $k = 2$ and panels (g)-(i) show contours for $k = 3$ at the same times. The contour interval is 3.76×10^{-2} $\mathrm{m^2 s^{-1}}$ in all panels. Solid contours denote $\psi_k \geq 0$, dotted contours $\psi_k < 0$.

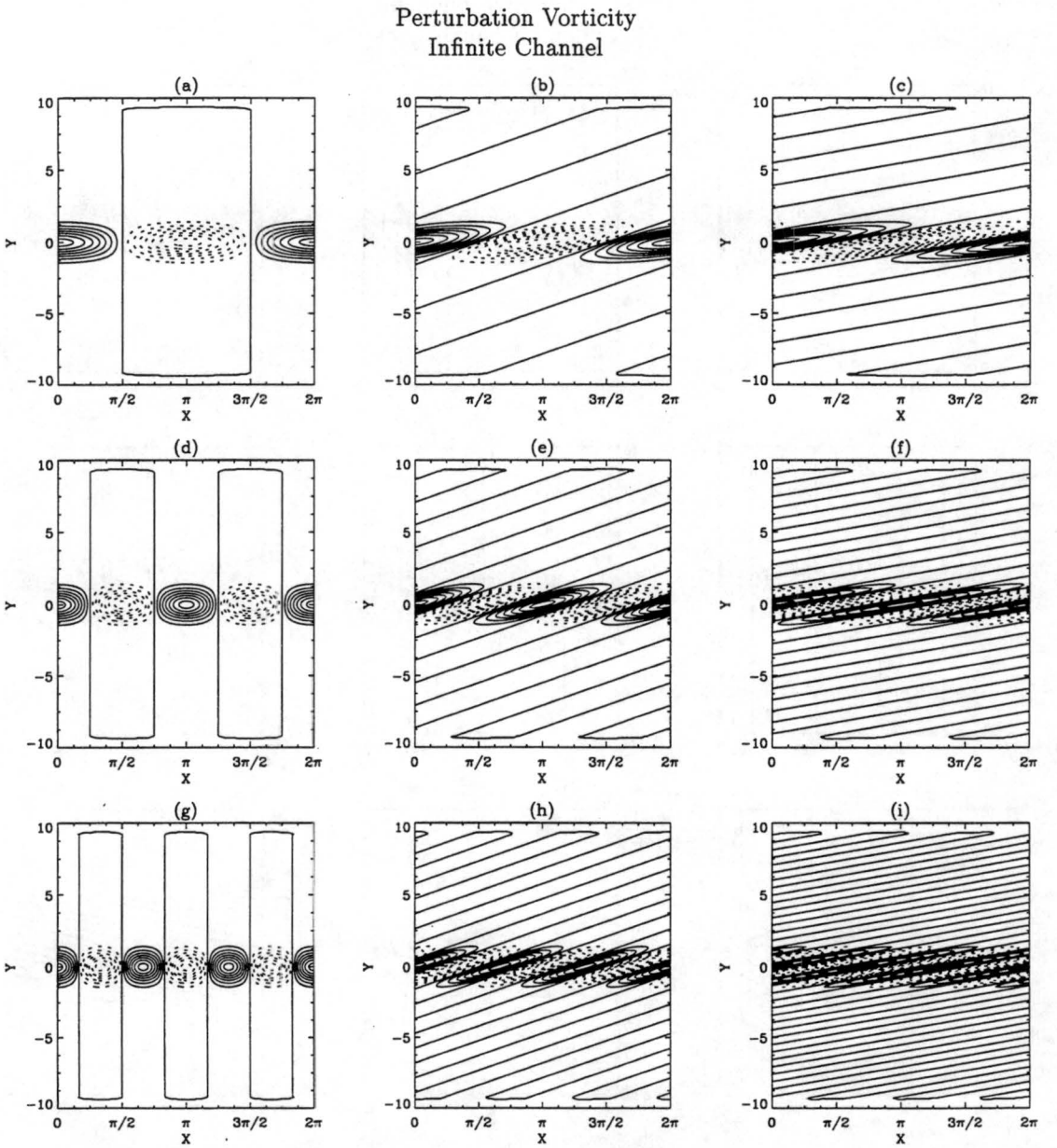

Fig. 2.6: Perturbation vorticity for the Gaussian initial vorticity profile $\hat{\zeta}_o = \exp\left(-y^2\right)$. The panels are the same as in figure 2.5. The contour interval is 1.33×10^{-1} s^{-1} in all panels.

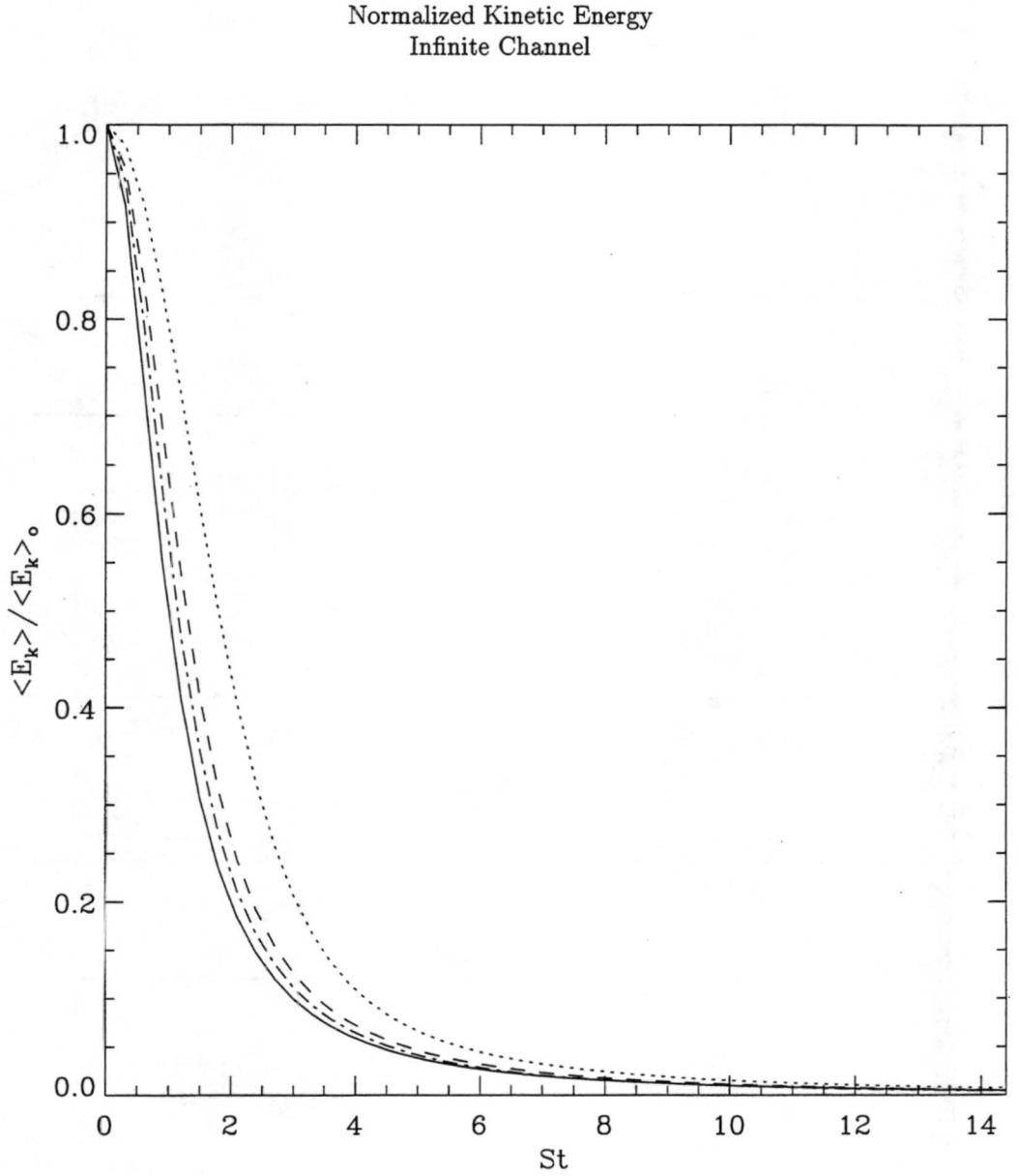

Fig. 2.7: Normalized kinetic energy for the Gaussian initial condition $\hat{\zeta}_o = \exp(-y^2)$ for $k = 1$ (dot), $k = 2$ (dash), and $k = 3$ (dot dash). The solid curve is the normalized kinetic energy for the upright plane wave.

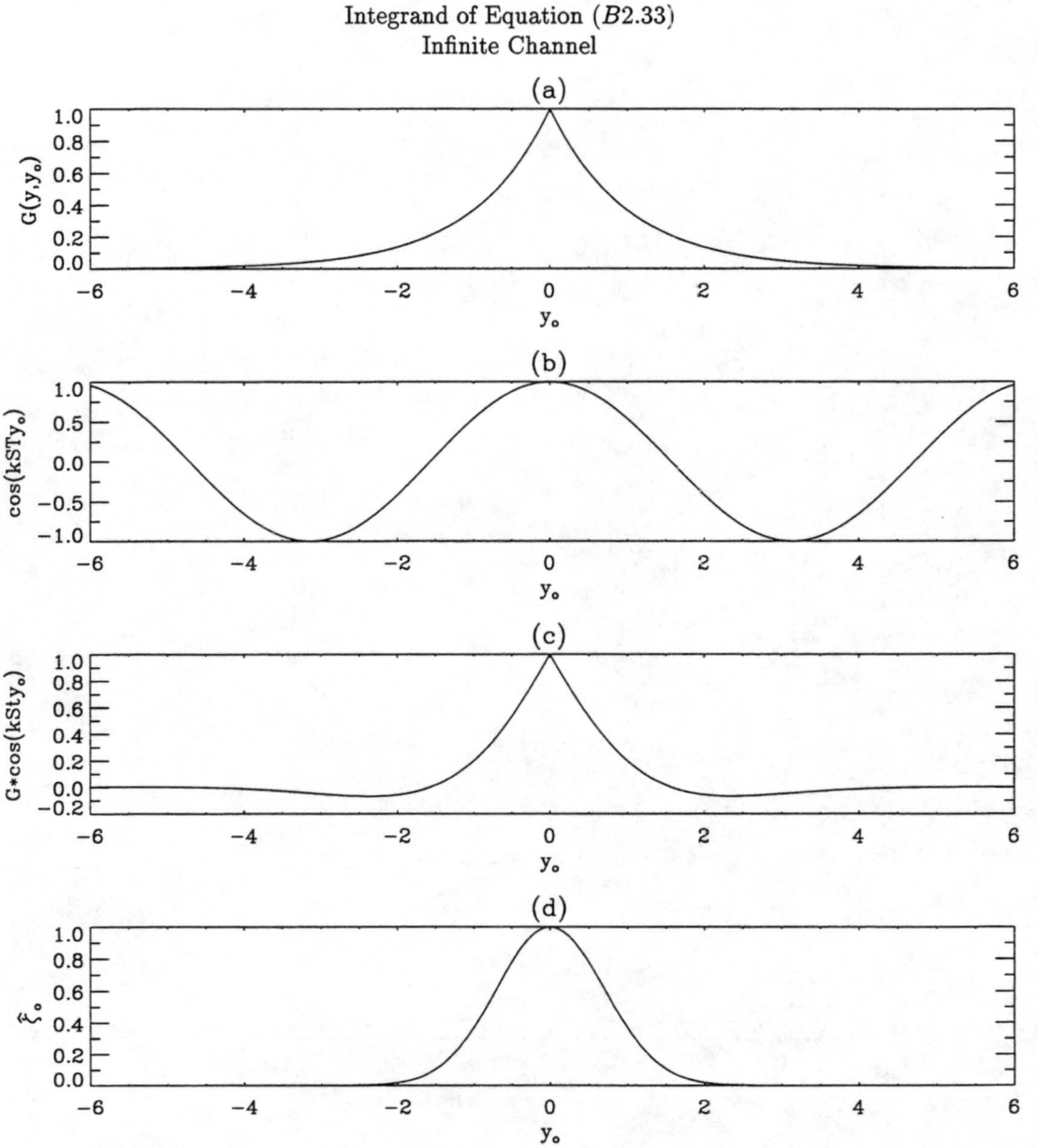

Fig. 2.8: The integrand of equation (B2.33) for $k = 1$, $y = 0$, and $St = 1.0$. (a) The Green's function. (b) The phase function. (c) The product of (a) and (b). (d) The initial vorticity profile $\hat{\zeta}_o = \exp(-y_o^2)$.

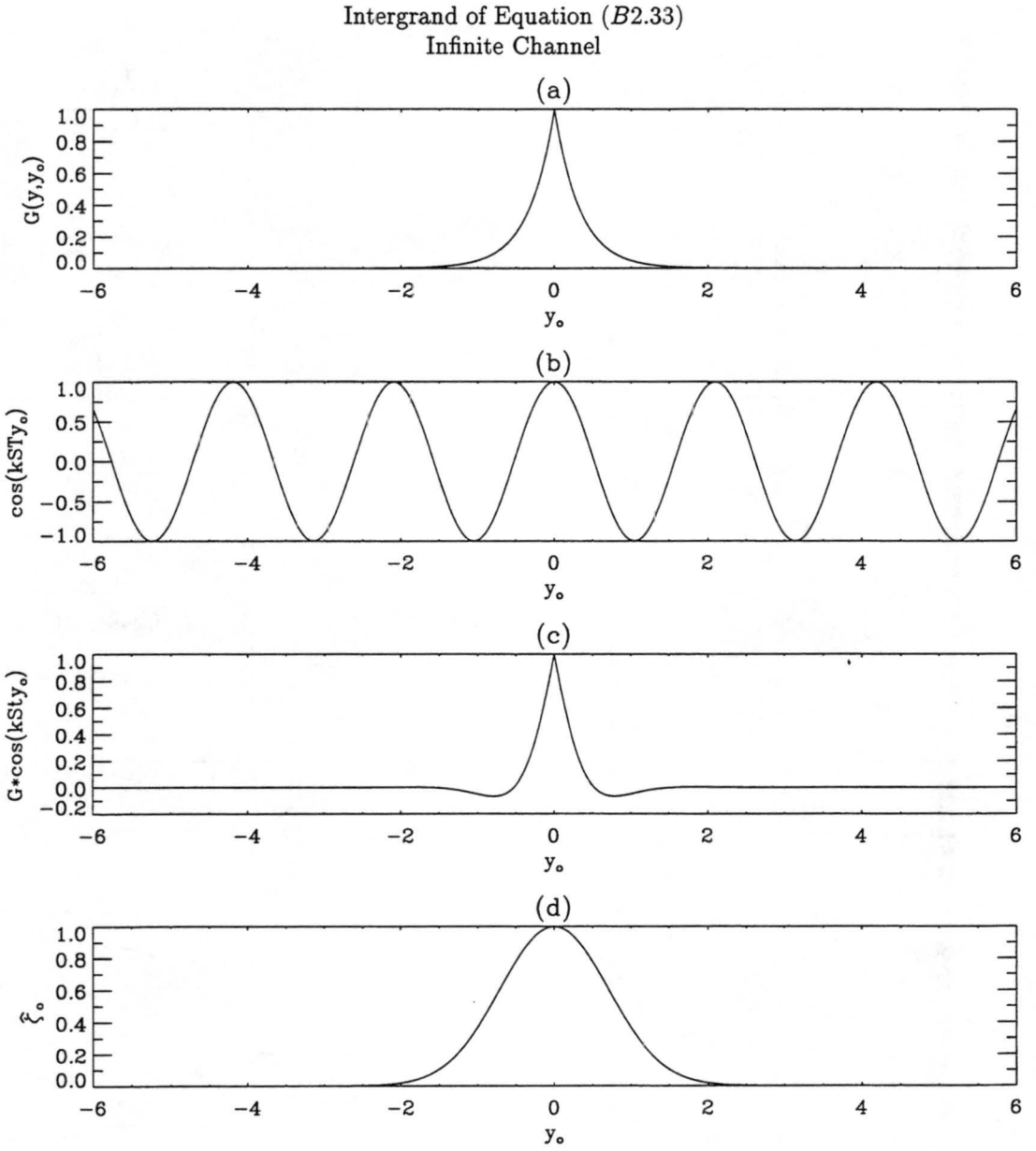

Fig. 2.9: Same as Fig. 2.8 except $k = 3$.

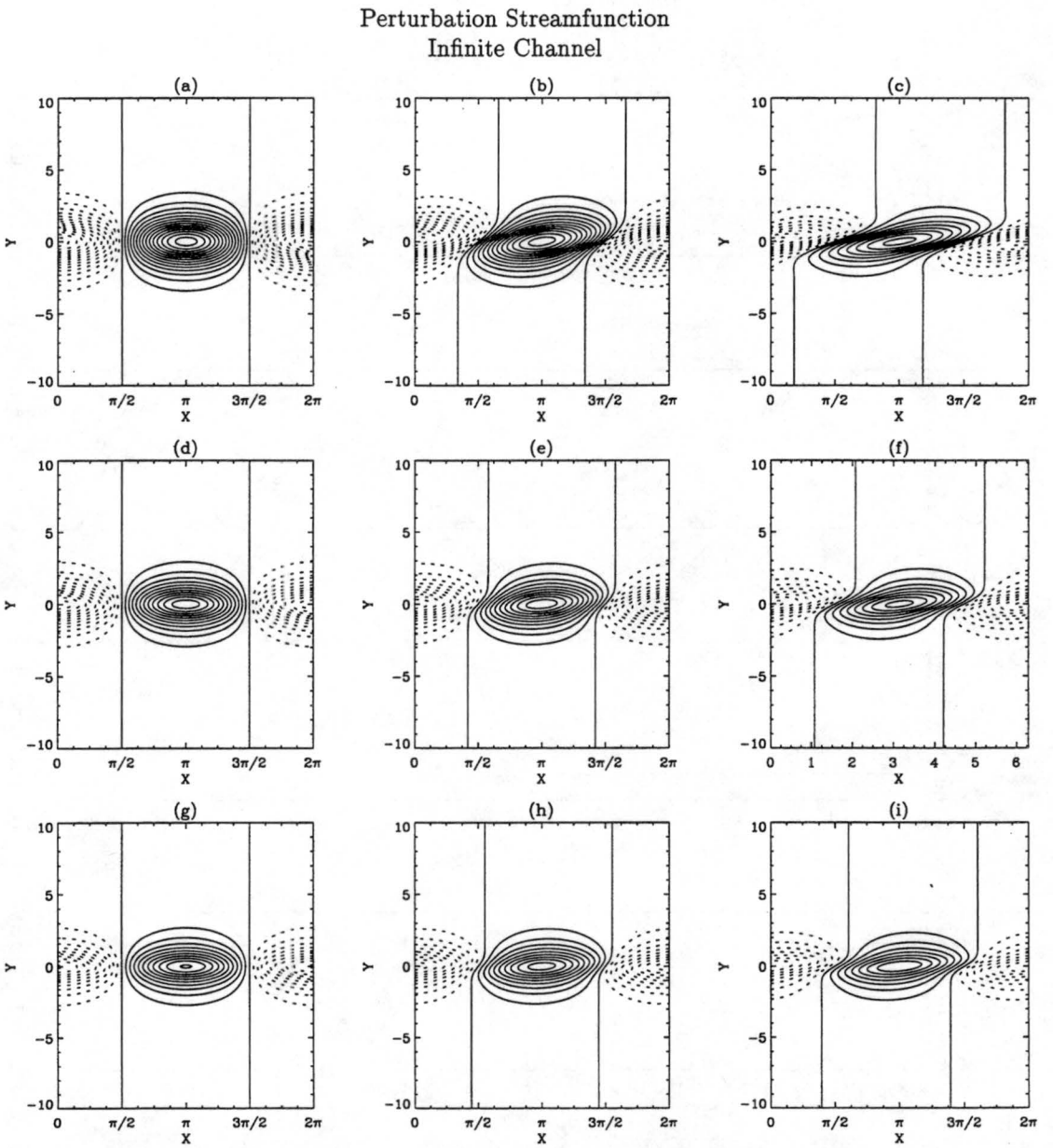

Fig. 2.10: Perturbation streamfunction for zonal wavenumber $k = 1$. Panels (a)-(c) show contours for the initial vorticity profile $\hat{\zeta}_o = \exp\left(-y^2\right)$ at times $St = 0.0$, 1.0, and 2.0, respectively. Panels (d)-(f) show contours for the initial vorticity profile $\hat{\zeta}_o = \exp\left(-2y^2\right)$ and panels (g)-(i) show contours for the initial vorticity profile $\hat{\zeta}_o = \exp\left(-3y^2\right)$ at the same times. The contour interval is 3.76×10^{-2} $\mathrm{m^2 s^{-1}}$ in all panels. Solid contours are $\psi_k \geq 0$, dotted contours $\psi_k < 0$.

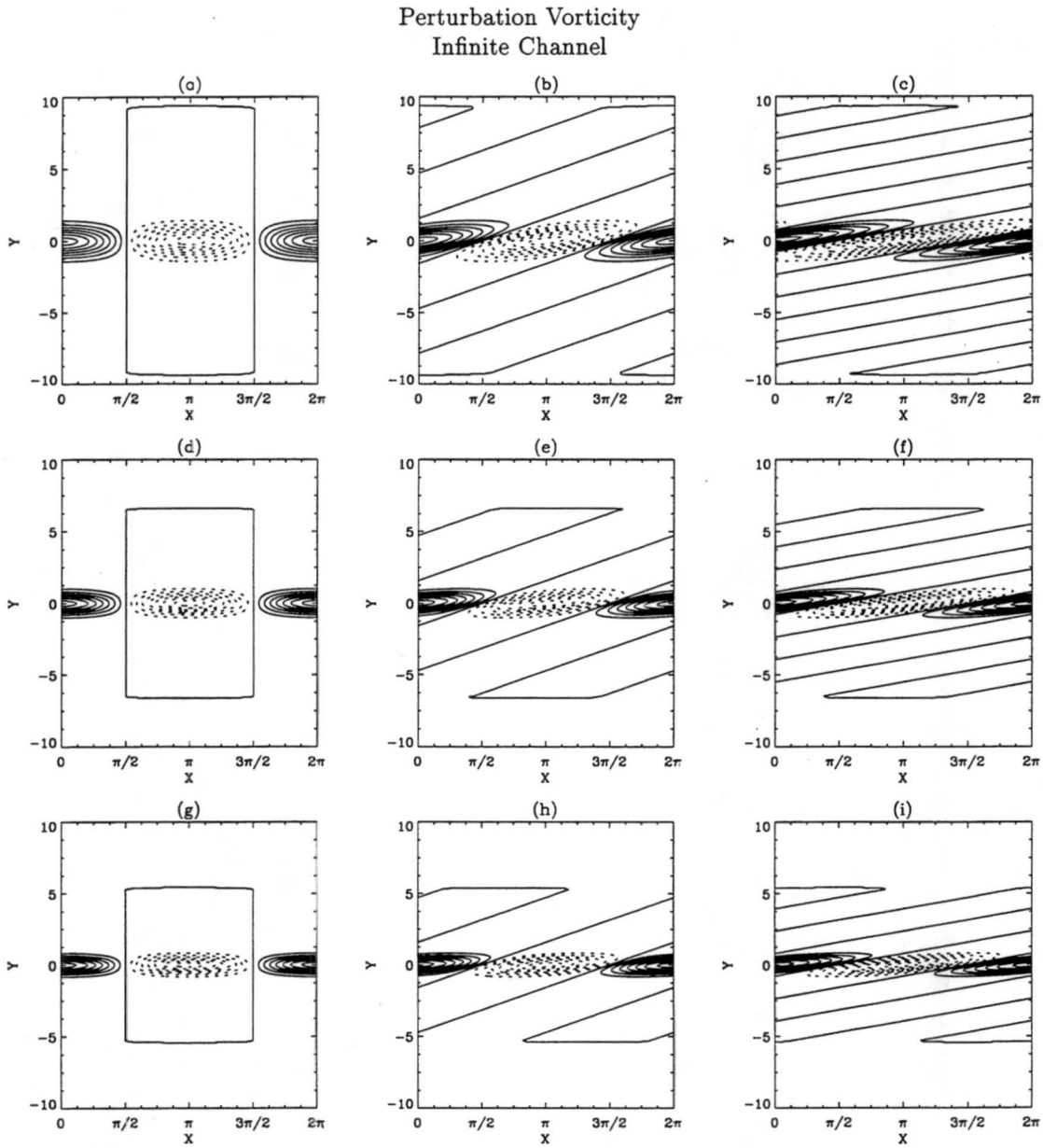

Fig. 2.11: Perturbation vorticity for zonal wavenumber $k = 1$. Panels are the same as in figure 2.10. Contour interval is 1.33×10^{-1} s^{-1} in all panels.

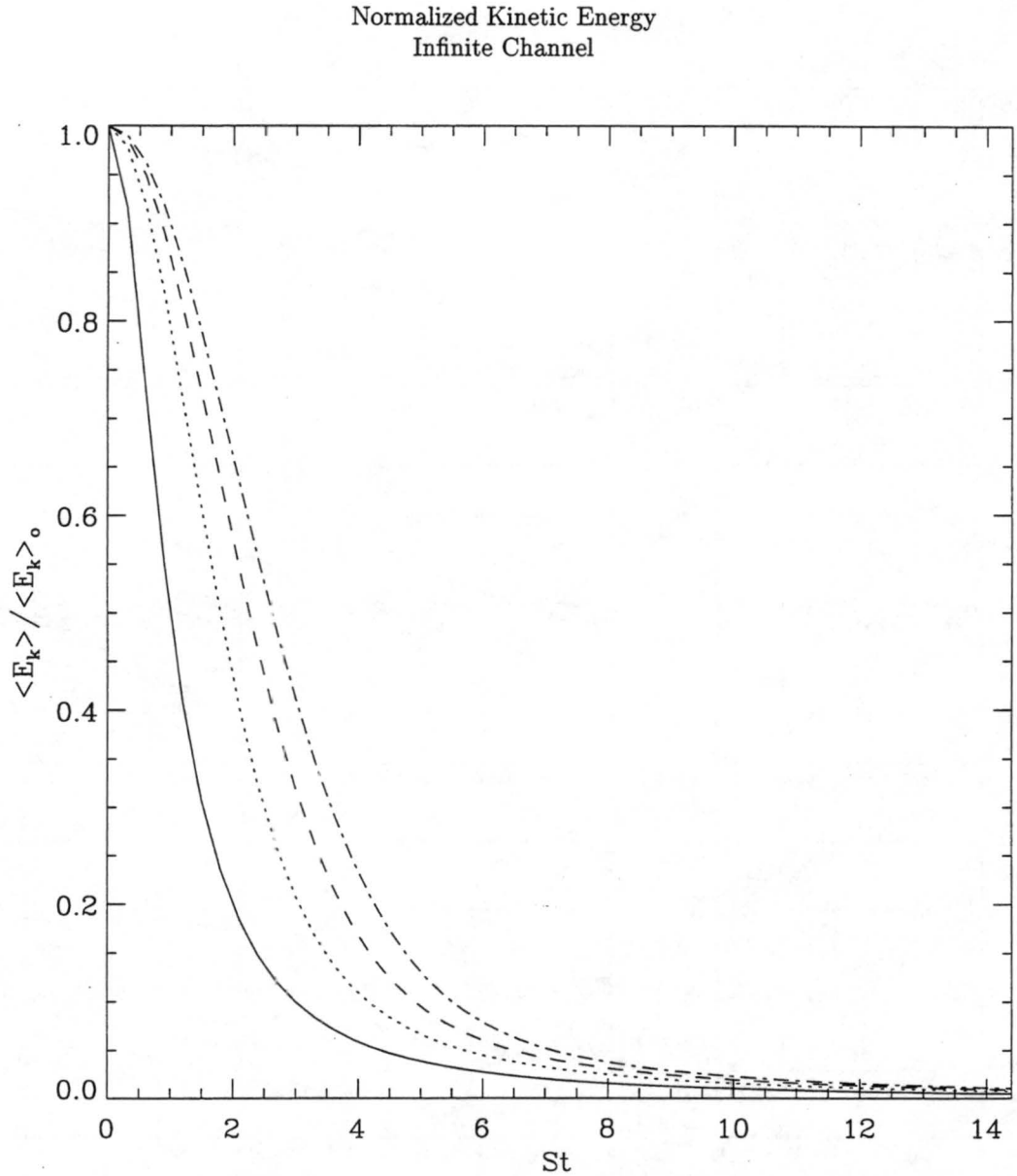

Fig. 2.12: Normalized perturbation kinetic energy for zonal wavenumber $k = 1$ for the Gaussian initial vorticity profiles $\hat{\zeta}_o = \exp(-y^2)$ (dot), $\hat{\zeta}_o = \exp(-2y^2)$ (dash), and $\hat{\zeta}_o = \exp(-3y^2)$ (dot dash). The solid curve is the normalized kinetic energy for the upright plane wave.

CHAPTER 3

ALGEBRAIC DECAY IN BOUNDED SIMPLE SHEAR

3.1 Introduction

The purpose of this chapter is to briefly examine how meridional boundaries alter the evolution of perturbations in simple shear flow. Since the evolution of asymmetries in a bounded vortex is the topic of the next chapter, investigating the effects of boundaries in the simple shear problem is a natural intermediate step.

3.2 Bounded Rectilinear Shear

The presence of boundaries does not alter the governing equations used in chapter 2. Nevertheless, meridional boundaries provide a convenient length scale that may be used to nondimensionalize the equations. Letting $(x, y) = L(\tilde{x}, \tilde{y})$, $\zeta = S\tilde{\zeta}$, and $t = \tilde{t}/S$ where L is the boundary separation and the tildes denote nondimensional quantities, the linearized vorticity equation $(B2.9)$ becomes

$$\frac{\partial \tilde{\zeta}}{\partial \tilde{t}} + \tilde{y}\frac{\partial \tilde{\zeta}}{\partial \tilde{x}} = 0. \qquad (B3.1)$$

Although the magnitude of the shear is no longer explicit in $(B3.1)$, the evolutionary time is scaled by the shear. Upon application of the Fourier-Laplace transforms defined in chapter 2, equation $(B3.1)$ becomes

$$\left(\frac{\partial^2}{\partial y^2} - k^2\right)\hat{\psi} = \hat{\zeta}_o e^{-ikty}. \qquad (B3.2)$$

For notational simplicity, the tildes have been dropped. Unless otherwise noted, all quantities are henceforth nondimensional.

Solutions to $(B3.2)$ depend on the choice of boundaries. Here, the meridional boundaries are assumed to be slippery walls at $y = a$ and $y = b$ where $a < b$. Thus, $v(a) = v(b) = 0$ to satisfy the no

normal flow condition. In terms of a Fourier perturbation streamfunction amplitude, the boundary conditions become $\hat{\psi}(a) = \hat{\psi}(b) = 0$.

The Green's function technique is used to solve ($B3.2$) subject to the boundary conditions. Imposing the continuity and jump conditions from the previous chapter along with the boundary conditions yields

$$G(y, y_o) = \frac{1}{k \sinh[k(b-a)]} \begin{cases} \sinh[k(y-a)] \sinh[k(y_o-b)], & a \le y \le y_o \\ \sinh[k(y-b)] \sinh[k(y_o-a)], & y_o \le y \le b \end{cases}. \tag{B3.3}$$

The solution to ($B3.2$) is then

$$\hat{\psi} = \int_a^b G(y, y_o) \hat{\zeta}_o e^{-ikty_o} \, dy_o. \tag{B3.4}$$

To complete the derivation, the inverse Fourier transform is applied to ($B3.4$) giving

$$\psi_k = \int_a^b G(y, y_o) \hat{\zeta}_o e^{ik(x-ty_o)} \, dy_o, \tag{B3.5}$$

where the subscript k is in accord with the convention of chapter 2.

3.3 Uniform Initial Condition

The initial vorticity given by $\hat{\zeta}_o = -k^2$, which corresponds to the upright plane wave of chapter 2, is considered first. Substituting $\hat{\zeta}_o$ into ($B3.5$) yields

$$\psi_k = \frac{1}{1+t^2} \left\{ \cos[k(x-ty)] + \frac{\sinh[k(y-b)] \cos[k(x-ta)] - \sinh[k(y-a)] \cos[k(x-tb)]}{\sinh[k(b-a)]} \right\}. \tag{B3.6}$$

The first term inside the braces is recognized as the infinite plane wave solution while the second term is the boundary correction that ensures $\psi_k(a) = \psi_k(b) = 0$. Figure 3.1 plots streamfunction contours for initial vorticity $\hat{\zeta} = -k^2$ and boundaries at $a = -1$, $b = 1$. The rows show $k = 1$, 2, and 3, respectively, while the columns denote $t = 0.0$, 2.0, and 4.0, respectively. The boundary correction in ($B3.6$) decreases the maximum streamfunction amplitude relative to the unbounded case since $\sinh[k(y-b)] \le 0$ and $-\sinh[k(y-a)] \le 0$ for all y, while $\sinh[k(b-a)] > 0$. As k increases for a given boundary separation, the magnitude of the boundary correction decreases and the maximum streamfunction amplitude increases since the hyperbolic sine in the denominator

increases faster than either of the hyperbolic sine terms in the numerator. In the limit $k \to \infty$, the boundary correction goes to zero and the plane wave solution is recovered.

The evolution of perturbations in a bounded channel forced by a uniform initial vorticity profile may be further analyzed by examining the integrated kinetic energy (KE) associated with (B3.6). This is given by

$$\begin{aligned}\langle E_k \rangle = \frac{k^2}{2(1+t^2)^2} \Bigg\{ & \frac{(1+t^2)}{2} + \frac{2\{\cos[kt(b-a)] - \cosh[k(b-a)]\}}{k(b-a)\sinh[k(b-a)]} \\ & - \frac{\cos[kt(b-a)]\cosh[k(b+a)]\{\sinh(2kb) - \sinh(2ka)\}}{2k(b-a)\sinh^2[k(b-a)]} \\ & + \frac{\cos[kt(b-a)]\sinh[k(b+a)]\{\cosh(2kb) - \cosh(2ka)\}}{2k(b-a)\sinh^2[k(b-a)]} \\ & + \frac{\sinh[2k(b-a)]}{2k(b-a)\sinh^2[k(b-a)]} \Bigg\}. \end{aligned} \qquad (B3.7)$$

The first term inside the braces is the energy of the infinite plane wave while the other terms describe how the perturbation energy is changed by the presence of boundaries. Since the first term decays as t^{-2} while the remaining terms decay as t^{-4}, the infinite plane wave solution emerges for increasing t. Figure 3.2 shows the normalized KE as a function of time for initial vorticity $\hat{\zeta}_o = -k^2$ for boundaries at $a = -1$, $b = 1$. Unlike the infinite plane wave case where the energy decay was independent of k, perturbations decay more rapidly with increasing wavenumber for a constant initial condition in a bounded channel. Moreover, the $k = 1$ perturbation decays significantly slower than the higher wavenumber perturbations. While very different from the infinite plane wave, disturbance evolution for a uniform initial vorticity profile in bounded shear is qualitatively similar to that of an unbounded Gaussian initial condition.

The similarities arise because each problem has a characteristic length scale. In the unbounded problem, the initial vorticity profile defined the length scale. For a constant initial condition in a bounded channel, the boundary separation defines the length scale. From (B3.6), it is seen that changing the boundary separation for a fixed k is equivalent to changing k for a fixed boundary separation. Thus, as $b - a$ increases, the boundary correction term decreases and the maximum streamfunction amplitude increases. As expected, in the limit of infinite boundary separation, the plane wave solution is recovered.

Similar arguments explain the effect of increasing boundary separation on the perturbation evolution as described by ($B3.7$). As $b-a$ increases, the denominators of the boundary terms increases more rapidly than the corresponding numerators and the perturbation decays more rapidly. In the limit of infinite boundary separation, the plane wave evolution is recovered. Figures 3.1 and 3.2 can be used to illustrate the described behavior if the plots for k in the figures are reinterpreted as plots for $b-a$. Physically, increasing the boundary separation increases the meridional scale of the perturbation. Thus, the perturbation is sheared more and decays more rapidly. This is analogous to changing the scale of the Gaussian initial condition of chapter 2.

3.4 The Gaussian

The evolution of perturbations forced by Gaussian initial vorticity profiles in a bounded channel is now considered. Since ($B3.5$) does not admit closed form solutions, the trapezoidal rule is used to evaluate the integral.

Figures 3.3 and 3.4 plot streamfunction and vorticity contours, respectively, for initial vorticity $\hat{\zeta}_o = \exp(-y^2)$ and zonal wavenumber $k = 1$. The rows show contours for boundary separation $b-a$ = 0.2, 2.0, and 20.0, respectively, while the columns show contours for time t = 0.0, 2.0, and 4.0, respectively. Note that the bottom row is virtually identical to the unbounded case. In terms of the two characteristic length scales, the rows represent $b-a \ll 1/\sqrt{\alpha}$, $b-a \sim 1/\sqrt{\alpha}$, and $b-a \gg 1/\sqrt{\alpha}$, respectively. As long as $b-a < 1/\sqrt{\alpha}$, the maximum streamfunction amplitude and the decay rate will be decreased relative to the unbounded case. For $b-a > 1/\sqrt{\alpha}$, the unbounded evolution may be recovered provided $b-a$ is sufficiently large to render boundary effects in the Green's function negligible.

Figure 3.5 shows the normalized KE as a function of time for initial vorticity $\hat{\zeta}_o = \exp(-y^2)$ and zonal wavenumber $k = 1$. As was seen for the constant initial condition in the bounded channel, increasing the boundary separation increases the decay rate since the perturbation is sheared more. The curve corresponding to $b-a = 20.0$ in figure 3.5 is the decay observed in the unbounded problem and does not change for further increases in the boundary separation. At this point, the meridional

scale of the perturbation is the characteristic length scale. For this curve to asymptote to the plane wave solution at small times, the zonal wavenumber must be increased.

3.5 Summary

The evolutionary decay of perturbations in bounded simple shear flow has been examined as an initial-value problem. The case of a uniform vorticity profile was considered first. Relative to the unbounded problem of chapter 2, the maximum streamfunction amplitude was smaller and the decay rate was slower because the presence of boundaries introduced a characteristic length scale. The infinite plane wave is not a localized disturbance and, thus, decays faster than any bounded disturbance. In the limits of large zonal wavenumber, boundary separation, and time, the infinite plane wave solution emerged.

The case of Gaussian initial vorticity profiles was then examined. For boundary separations smaller in scale than the meridional scale of the perturbation, the maximum streamfunction amplitude was smaller and the decay was slower relative to the unbounded case. The scale of the boundary separation was the characteristic length scale. When the boundary separation was greater than the scale of the perturbation, the unbounded evolution was recovered as long as the boundary separation was large enough to make the boundary effects in the Green's function negligible.

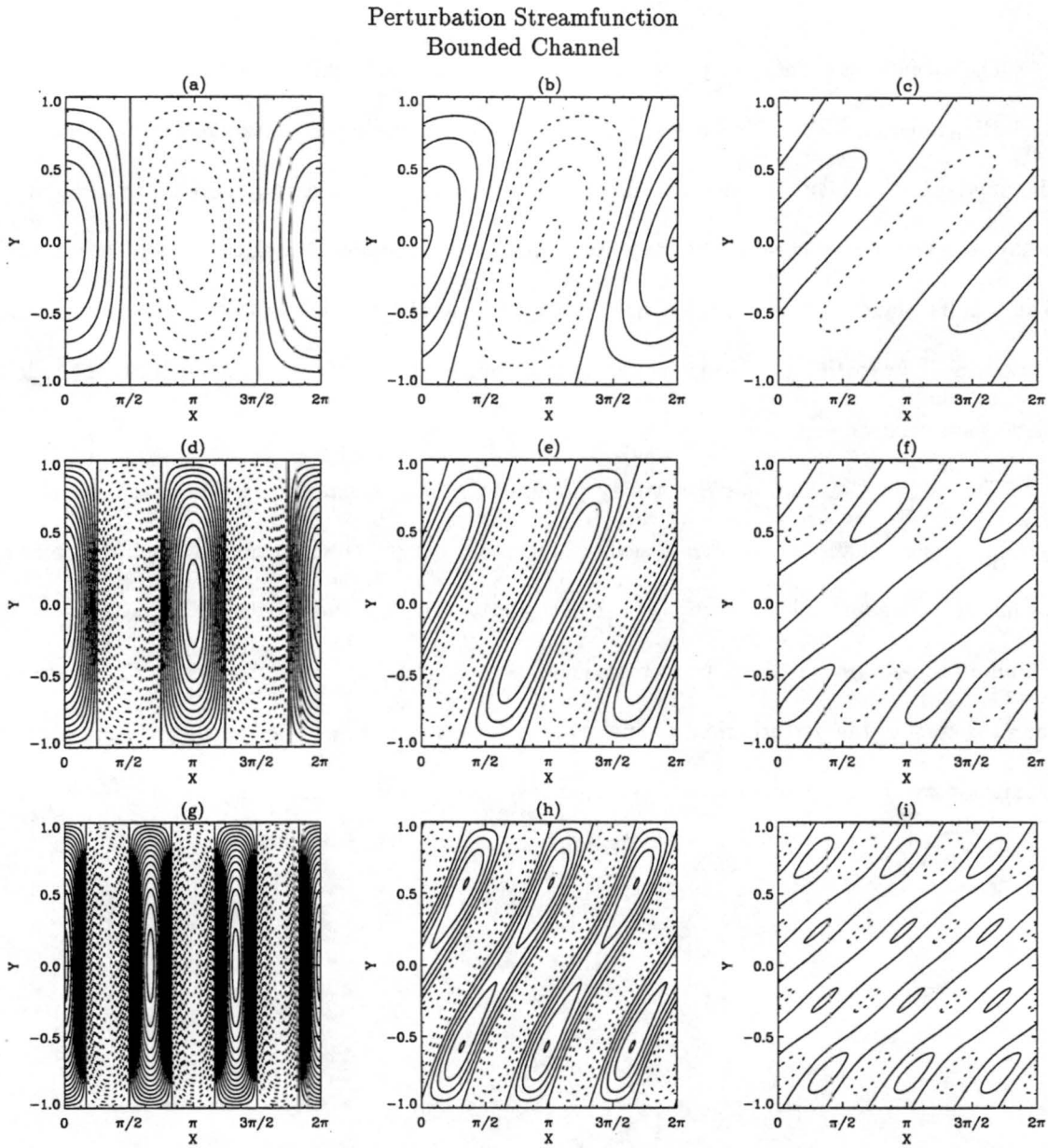

Fig. 3.1: Perturbation streamfunction contours for initial vorticity $\hat{\zeta}_o = -k^2$ and boundaries at $a = -1.0$, $b = 1.0$. Panels (a)-(c) show contours for zonal wavenumber $k = 1$ at times $t = 0.0$, 2.0, and 4.0, respectively. Panels (d)-(f) show contours for $k = 2$ and panels (g)-(i) show contours for $k = 3$ at the same times. The contour interval is 6.21×10^{-2} in all panels. Solid lines denote $\psi_k \geq 0$, dotted lines $\psi_k < 0$.

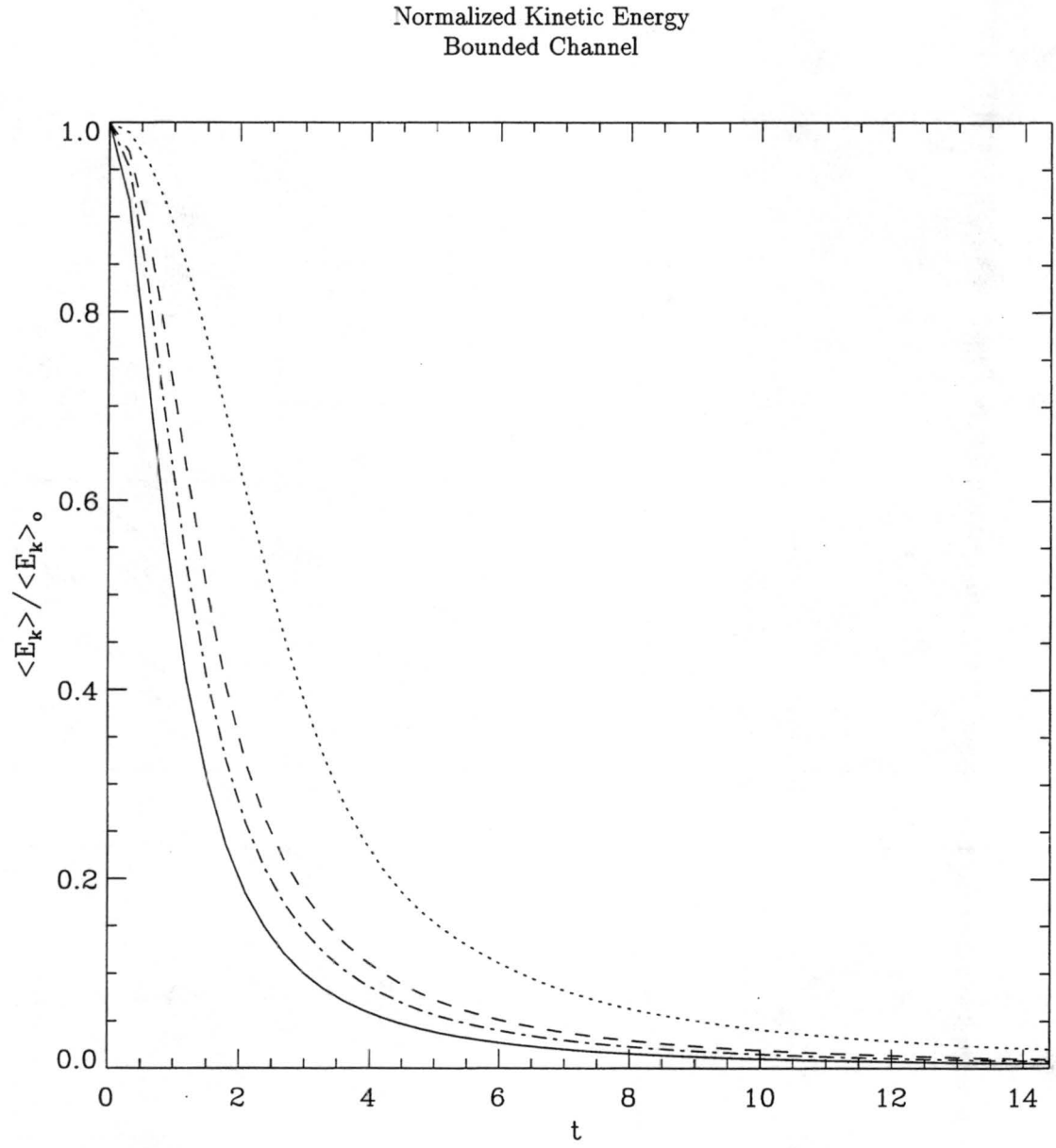

Fig. 3.2: Normalized kinetic energy for initial vorticity $\hat{\zeta}_o = -k^2$ and boundaries at $a = -1.0$, $b = 1.0$. The curves are the energy decay for $k = 1$ (dot), $k = 2$ (dash), and $k = 3$ (dot dash). The solid curve is the energy decay for the upright plane wave.

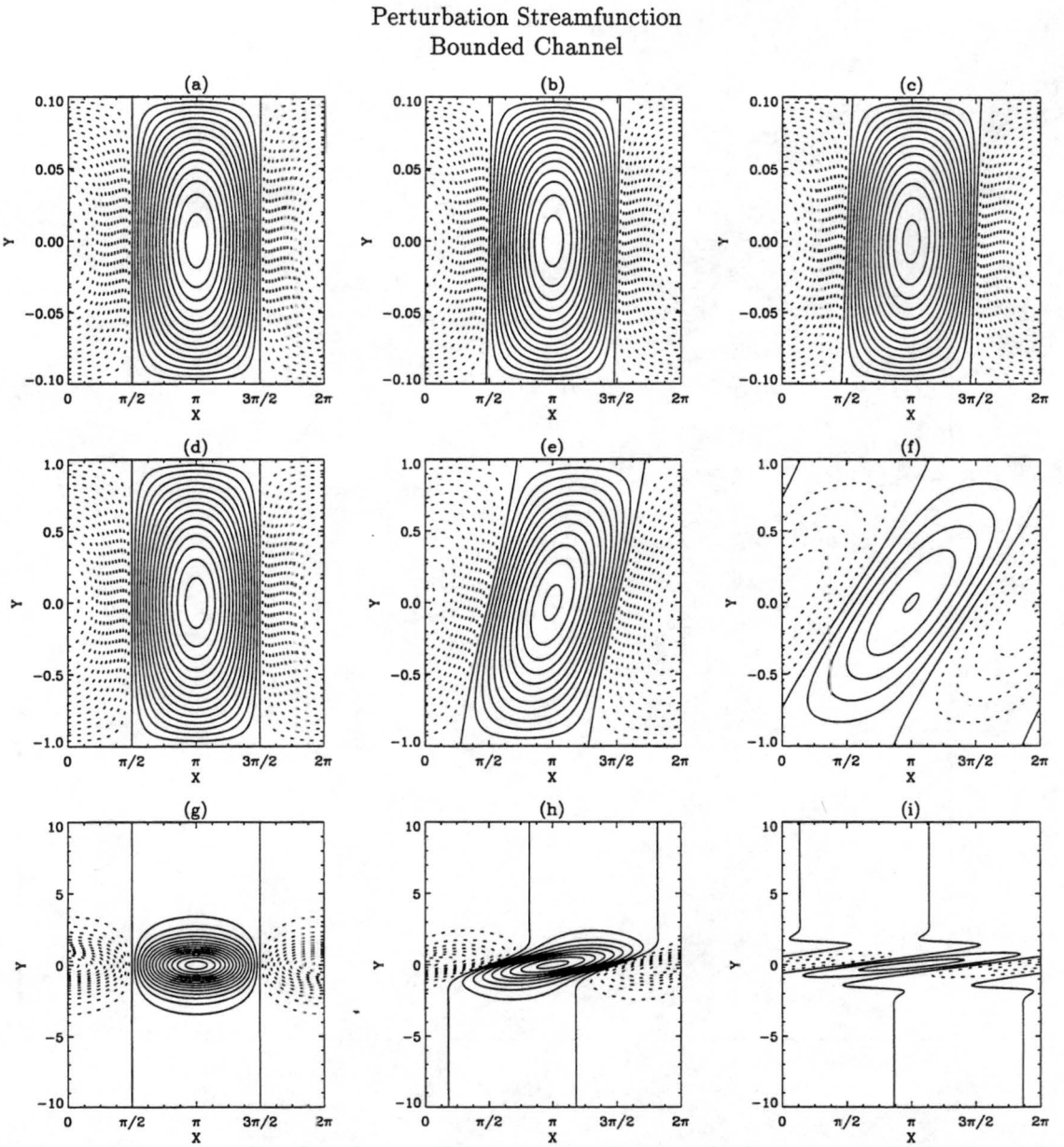

Fig. 3.3: Perturbation streamfunction contours for zonal wavenumber $k = 1$ and initial vorticity $\hat{\zeta}_o = \exp(-y^2)$. Panels (a)-(c) are for boundaries at $a = -0.1$, $b = 0.1$. The contour interval is 3.43×10^{-4}. Panels (d)-(f) are for boundaries at $a = -1.0$, $b = 1.0$. The contour interval is 2.11×10^{-2}. Panels (g)-(i) are for boundaries at $a = -10.0$, $b = 10.0$. The contour interval is 3.76×10^{-2}. The columns denote time $t = 0.0$, 2.0, and 4.0, respectively. Solid lines are $\psi_k \geq 0$, dotted lines $\psi_k < 0$.

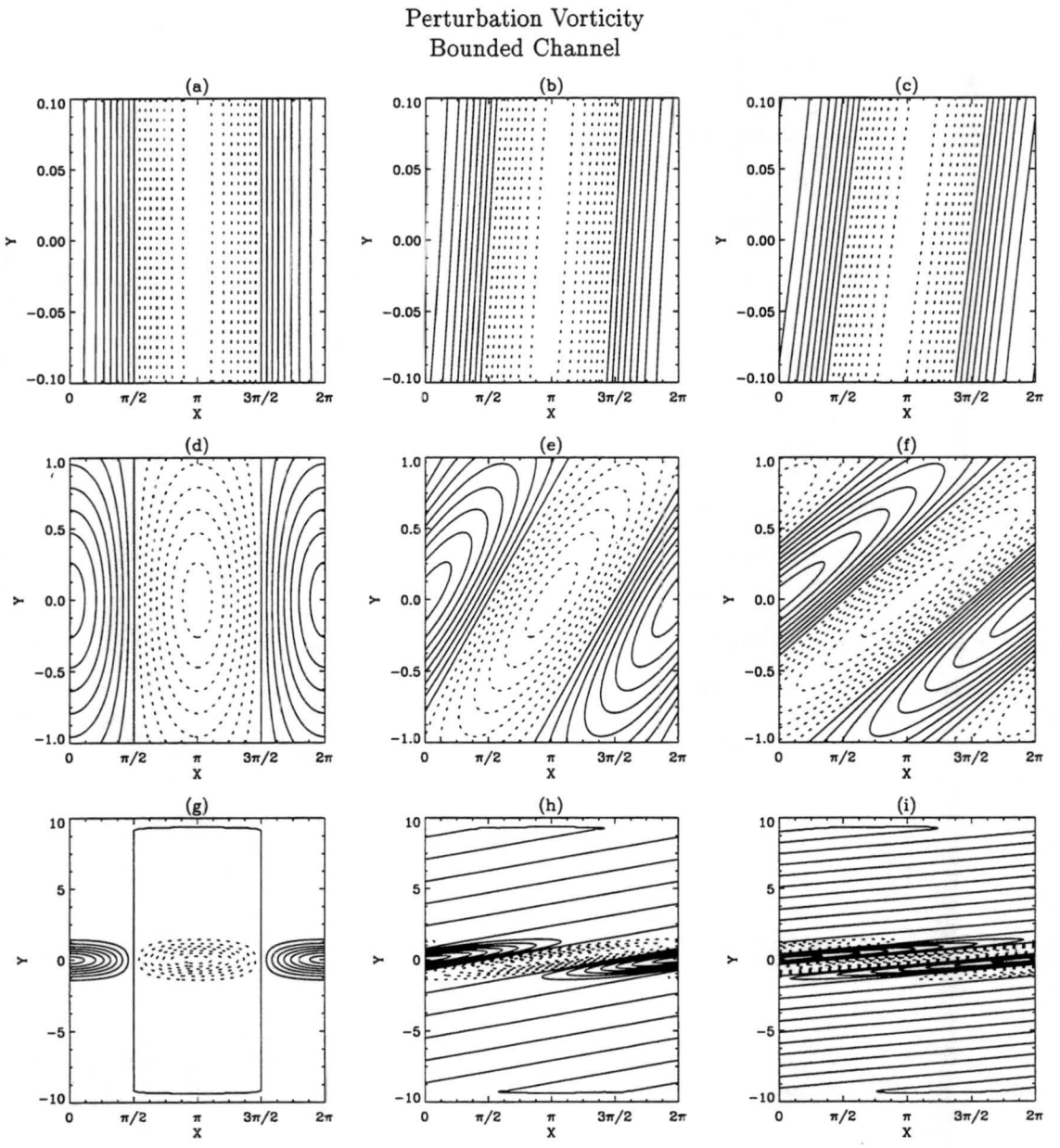

Fig. 3.4: Perturbation vorticity contours for zonal wavenumber $k = 1$ and initial vorticity $\hat{\zeta}_o = \exp(-y^2)$. The panels are the same as in figure 3.3. The contour interval is 1.33×10^{-1} in all panels.

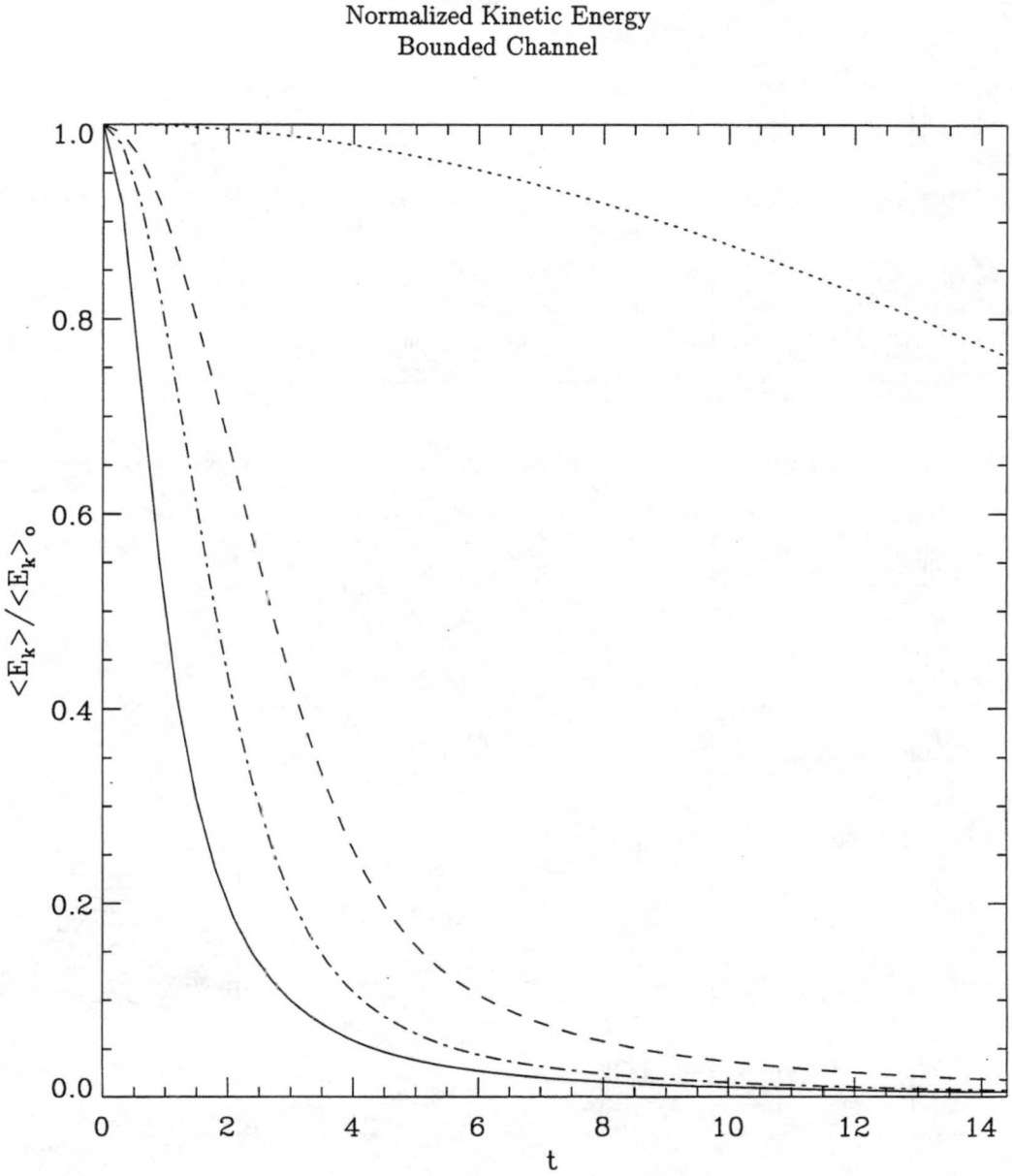

Fig. 3.5: Normalized kinetic energy for $k = 1$ and initial vorticity $\hat{\zeta}_o = \exp(-y^2)$. The curves are the energy decay for boundaries at $a = -0.1$, $b = 0.1$ (dot); $a = -1.0$, $b = 1.0$ (dash); and $a = -10.0$, $b = 10.0$ (dot dash) . The solid curve is the energy decay for the upright plane wave.

CHAPTER 4

AXISYMMETRIZATION IN SWIRLING FLOW

4.1 Introduction

The purpose of this chapter is to study the axisymmetrization process in a vortex. The objective is to extend the results of the previous chapters to a rapidly rotating fluid with radially varying shear. The dependence of asymmetric evolution on the azimuthal wavenumber and the radial structure of an initial vorticity profile is of particular interest. As in previous chapters, the model employed is the inviscid incompressible Euler equations on an f-plane, but here a cylindrical coordinate system is chosen to represent the problem. Consistent with observations (SM), linear perturbation theory is used to decompose the flow into a circularly symmetric basic state of swirl and small-amplitude asymmetries.

In formulating the asymmetric vortex model, an appropriate coordinate system must be chosen. A natural coordinate system is one that moves with the center of the vortex, i.e., a storm-relative coordinate. Following Willoughby (1979), SM showed that in storm-relative coordinates, vortex motion on an f-plane merely modifies the definition of pressure while preserving the form of the momentum equations. Since the model adopted below is ultimately formulated at the level of the vorticity equation, the storm motion is no longer explicit in the vorticity dynamics and only appears in the boundary conditions at infinity. In a Fourier azimuthal representation, storm motion projects only onto the azimuthal wavenumber one component. For the simple case of a resting environment, the associated winds must coincide with the motion at infinity. All other azimuthal components must vanish at infinity. The more common choice of coordinates is the ground-based system. Here, vortex motion is explicit in the vorticity dynamics and, for a quiescent environment, all asymmetries must vanish at infinity. Unless otherwise stated, a ground-based coordinate system will be adopted.

4.2 Swirling Model

The radial and tangential momentum equations and continuity equation in cylindrical coordinates are, respectively,

$$\frac{\partial u}{\partial t} + u\frac{\partial u}{\partial r} + \frac{v}{r}\frac{\partial u}{\partial \lambda} - fv - \frac{v^2}{r} = -\frac{\partial p}{\partial r}, \tag{4.1a}$$

$$\frac{\partial v}{\partial t} + u\frac{\partial v}{\partial r} + \frac{v}{r}\frac{\partial v}{\partial \lambda} + fu + \frac{uv}{r} = -\frac{1}{r}\frac{\partial p}{\partial \lambda}, \tag{4.1b}$$

$$\frac{1}{r}\frac{\partial (ru)}{\partial r} + \frac{1}{r}\frac{\partial v}{\partial \lambda} = 0, \tag{4.1c}$$

where r and λ are the radius and azimuth, u and v are the radial and azimuthal winds, f is the constant Coriolis parameter, and p is the pressure divided by constant density. Explicit dependence on the pressure and Coriolis parameter may be removed by taking the horizontal curl of $(B4.1a)$ and $(B4.1b)$. The result is the vorticity equation, given by

$$\frac{\partial \zeta}{\partial t} + u\frac{\partial \zeta}{\partial r} + \frac{v}{r}\frac{\partial \zeta}{\partial \lambda} = 0 \tag{B4.2}$$

Here ζ is the vertical component of the vorticity, defined by

$$\zeta = \frac{1}{r}\frac{\partial (rv)}{\partial r} - \frac{1}{r}\frac{\partial u}{\partial \lambda} \tag{B4.3}$$

Equation $(B4.3)$ states that vorticity is conserved following the fluid particles.

Since intense atmospheric vortices often exhibit weak asymmetries, linear perturbation theory is applied about an axisymmetric basic state of swirl. Let $u = u'$, $v = \bar{v}(r) + v'$, and $p = \bar{p} + p'$ where an overbar denotes the basic state and a prime denotes an asymmetry. Neglecting products of primed quantities, equations $(B4.1a)$-$(B4.1c)$ become

$$\frac{\partial u'}{\partial t} + \frac{\bar{v}}{r}\frac{\partial u'}{\partial \lambda} - f\bar{v} - fv' - \frac{\bar{v}^2}{r} - \frac{2\bar{v}}{r}v' = -\frac{\partial}{\partial r}(\bar{p} + p'), \tag{4.4a}$$

$$\frac{\partial v'}{\partial t} + \frac{\bar{v}}{r}\frac{\partial v'}{\partial \lambda} + u'\frac{dv'}{dr} + fu' + \frac{\bar{v}}{r}u' = -\frac{1}{r}\frac{\partial}{\partial \lambda}(\bar{p} + p'), \tag{4.4b}$$

$$\frac{\partial (ru')}{\partial r} + \frac{\partial v'}{\partial \lambda} = 0. \tag{4.4c}$$

Noting from $(B4.3)$ that the basic state vorticity is only a function of r, the vorticity equation $(B4.2)$ is

$$\frac{\partial \zeta'}{\partial t} + \frac{\bar{v}}{r}\frac{\partial \zeta'}{\partial \lambda} + u'\frac{d\bar{\zeta}}{dr} = 0. \tag{B4.5}$$

Since the basic state variables alone must satisfy (4.1), the momentum equations imply

$$-f\bar{v} - \frac{\bar{v}^2}{r} = -\frac{\partial \bar{p}}{\partial r}, \tag{4.6a}$$

$$\frac{\partial \bar{p}}{\partial \lambda} = 0, \tag{4.6b}$$

while the continuity and vorticity conservation equations are trivially satisfied. Substituting the basic state relations back into (4.4) gives

$$\frac{\partial u'}{\partial t} + \frac{\bar{v}}{r}\frac{\partial u'}{\partial \lambda} - \left(f + \frac{2\bar{v}}{r}\right)v' = -\frac{\partial p'}{\partial r}, \tag{4.7a}$$

$$\frac{\partial v'}{\partial t} + \frac{\bar{v}}{r}\frac{\partial v'}{\partial \lambda} + \left(f + \frac{1}{r}\frac{\partial (r\bar{v})}{\partial r}\right)u' = -\frac{1}{r}\frac{\partial p'}{\partial \lambda}, \tag{4.7b}$$

$$\frac{\partial (ru')}{\partial r} + \frac{\partial v'}{\partial \lambda} = 0. \tag{4.7c}$$

Defining $\bar{\xi} = f + 2\bar{v}/r$, $\bar{\eta} = f + \bar{\zeta}$, and recalling that f is constant allows the equations of motion and the vorticity equation to be written as

$$\frac{\partial u'}{\partial t} + \frac{\bar{v}}{r}\frac{\partial u'}{\partial \lambda} - \bar{\xi}v' = -\frac{\partial p'}{\partial r}, \tag{4.8a}$$

$$\frac{\partial v'}{\partial t} + \frac{\bar{v}}{r}\frac{\partial v'}{\partial \lambda} + \bar{\eta}u' = -\frac{1}{r}\frac{\partial p'}{\partial \lambda}, \tag{4.8b}$$

$$\frac{\partial (ru')}{\partial r} + \frac{\partial v'}{\partial \lambda} = 0, \tag{4.8c}$$

$$\frac{\partial \zeta'}{\partial t} + \frac{\bar{v}}{r}\frac{\partial \zeta'}{\partial \lambda} + u'\frac{d\bar{\eta}}{dr} = 0. \tag{4.8d}$$

The quantities $\bar{\eta}$ and $\bar{\xi}$ represent the absolute vorticity and the effective Coriolis parameter of the symmetric vortex. For notational simplicity, the primes will now be dropped. All quantities will be perturbations unless they have an overbar. Attention is now restricted to ($B4.8d$).

Equation ($B4.8d$) is nondimensionalized by defining $r = R_m\tilde{r}$, $(u, \bar{v}) = V_m(\tilde{u}, \tilde{v})$, $t = R_m/V_m\tilde{t}$, $(\zeta, \bar{\eta}) = V_m/R_m(\tilde{\zeta}, \tilde{\eta})$, and $\lambda = \tilde{\lambda}$ where V_m is the maximum azimuthal wind, R_m is the radius of maximum winds, and tildes denote dimensionless quantities. Substituting these definitions back into equation ($B4.8d$), the factor V_m^2/R_m^2 is found common to every term. On dividing out this term, the nondimensional vorticity equation is formally identical to equation ($B4.8d$). Dropping the tildes for notational simplicity, the nondimensional linear vorticity equation is

$$\frac{\partial \zeta}{\partial t} + \frac{\bar{v}}{r}\frac{\partial \zeta}{\partial \lambda} + u\frac{d\bar{\eta}}{dr} = 0 \tag{$B4.9$}$$

Unlike the rectilinear problem in simple shear where there was no gradient of the basic state absolute vorticity, the perturbation vorticity in a swirling flow is generally not conserved following the basic state flow.

For the rectilinear problem in simple shear, the meridional gradient of the basic state zonal wind controlled the perturbation decay. The vorticity tendency was directly related to the advection of the vorticity by the basic state zonal wind. For the swirling problem, the vorticity tendency is proportional to the advection of the vorticity by the symmetric vortex. The basic state angular velocity is playing an analogous role in the swirling environment that the basic state zonal wind played in the rectilinear environment. It is therefore anticipated that the radial gradient of the basic state angular velocity will control the decay of asymmetries in the swirling vortex.

Before equation ($B4.9$) can be solved, boundary conditions must be specified. Since observations show that the rotation of a hurricane inside the radius of maximum winds is in approximate solid body rotation, the angular velocity gradient is small in that region and little symmetrization is expected there. To isolate the basic decay process, a boundary is placed at the radius of maximum winds. While this approach is justified on observational grounds, it also has the mathematical advantage of avoiding the geometric singularity associated with the vortex center. Since observations also show that asymmetries become comparable to the symmetric azimuthal wind several hundred kilometers from the storm center, the linear assumption is adequately satisfied for an outer boundary placed so that $\bar{v} \gg (u', v')$. In nondimensional coordinates, $r = a$ denotes the boundary at the radius of maximum winds while $r = b$ gives the location of the environmental boundary. The boundaries are assumed to be slippery walls at which the normal velocity vanishes. Thus, $u(a) = u(b) = 0$.

To ensure that solutions to the vorticity equation ($B4.9$) satisfy continuity ($B4.8c$), define a perturbation streamfunction such that

$$u = -\frac{1}{r}\frac{\partial \psi}{\partial \lambda}, \qquad v = \frac{\partial \psi}{\partial r}. \tag{$B4.10$}$$

Equation ($B4.3$) becomes

$$\zeta = \nabla^2 \psi \tag{$B4.11$}$$

where the Laplacian operator is given by

$$\nabla^2 = \left[\frac{1}{r}\frac{\partial}{\partial r}\left(r\frac{\partial}{\partial r}\right) + \frac{1}{r^2}\frac{\partial^2}{\partial \lambda^2}\right].$$

The vorticity equation ($B4.9$) is then

$$\left(\frac{\partial}{\partial t} + \frac{\bar{v}}{r}\frac{\partial}{\partial \lambda}\right)\left[\frac{1}{r}\frac{\partial}{\partial r}\left(r\frac{\partial}{\partial r}\right) + \frac{1}{r^2}\frac{\partial^2}{\partial \lambda^2}\right]\psi - \frac{1}{r}\frac{d\bar{\eta}}{dr}\frac{\partial \psi}{\partial \lambda} = 0. \qquad (B4.12)$$

Equation ($B4.12$) describes the evolution of the system subject to the constraint that the azimuthal gradient of the streamfunction vanish on the boundaries. Further transformation of this equation is desired to facilitate finding its solutions. Because the azimuthal variable is periodic by definition, the azimuthal dependence may be represented by a Fourier series where the Fourier transform pair is

$$\hat{f}(n) = \frac{1}{2\pi}\int_0^{2\pi} f(\lambda)e^{-in\lambda}\,d\lambda; \qquad n = \pm 1, \pm 2, \pm 3, \ldots \qquad (4.13a)$$

$$f(\lambda) = \sum_{n=-\infty}^{\infty} \hat{f}(n)e^{in\lambda}; \qquad n \neq 0 \qquad (4.13b)$$

and n is the azimuthal wavenumber. The wavenumber zero contribution is excluded from the above definitions because it represents the symmetric component which does not change in the linear problem. The Fourier transform will hereafter be applied to asymmetric quantities. As in chapter 2, the initial-value problem associated with ($B4.12$) is considered. This is done by using the Laplace transform pair, given by

$$f^{(q)}(q) = \int_0^{\infty} f(t)e^{-qt}\,dt \qquad (4.14a)$$

$$f(t) = \frac{1}{2\pi i}\oint_C f^{(q)}(q)e^{qt}\,dq \qquad (4.14b)$$

where q and C are the same as defined in chapter 2.

The Fourier transform of ($B4.12$) is

$$\left(\frac{\partial}{\partial t} + in\frac{\bar{v}}{r}\right)\left[\frac{1}{r}\frac{\partial}{\partial r}\left(r\frac{\partial}{\partial r}\right) - \frac{n^2}{r^2}\right]\hat{\psi} - \frac{in}{r}\frac{d\bar{\eta}}{dr}\hat{\psi} = 0 \qquad (B4.15)$$

while the Laplace transform of ($B4.15$) is

$$\left(q + in\frac{\bar{v}}{r}\right)\left[\frac{1}{r}\frac{\partial}{\partial r}\left(r\frac{\partial}{\partial r}\right) - \frac{n^2}{r^2}\right]\hat{\psi}^{(q)} - \frac{in}{r}\frac{d\bar{\eta}}{dr}\hat{\psi}^{(q)} = \left[\frac{1}{r}\frac{\partial}{\partial r}\left(r\frac{\partial}{\partial r}\right) - \frac{n^2}{r^2}\right]\hat{\psi}_o \qquad (B4.16)$$

with $\hat{\psi}_o$ the radial structure of the initial streamfunction for wavenumber n. The right side of equation ($B4.16$) is the initial vorticity for wavenumber n. Upon dividing by $q+in\bar{v}/r$, this equation can be rewritten

$$\left[\frac{1}{r}\frac{\partial}{\partial r}\left(r\frac{\partial}{\partial r}\right)-\frac{n^2}{r^2}\right]\hat{\psi}^{(q)}-\frac{in}{r}\frac{d\bar{\eta}}{dr}\frac{\hat{\psi}^{(q)}}{(q+in\bar{v}/r)}=\frac{\hat{\zeta}_o}{(q+in\bar{v}/r)}. \qquad (B4.17)$$

Unlike the rectilinear problem with zero vorticity gradient, the inverse Laplace transform of ($B4.17$) does not simply result in a differential equation for $\hat{\psi}$ (cf. ($B2.22$)). Rather, the direct inversion of the second term on the left side of ($B4.17$) requires the convolution theorem and yields $\hat{\psi}$ as the argument of a time integral. An alternative solution method for the analogous rectilinear problem is described by Case (1960) which requires evaluation of a contour integral in the complex plane involving a Green's function for ($B4.17$) multiplied by the right side. Ultimately, numerical schemes are needed to obtain explicit solutions. Such procedures, and thus the general solution to ($B4.17$), are beyond the scope of this thesis.

Here, attention is restricted to a specific class of vortices that admit simple solutions. If the second term on the left side of the equation is zero, the solution to ($B4.17$) is readily constructed. For the geometry considered in this chapter, the Rankine profile (see figure 4.1) given by

$$\bar{v}=a/r, \qquad r\geq a \qquad (B4.18)$$

satisifes this requirement since $\bar{\eta}(r)=f$. Equation ($B4.18$) then becomes

$$\left[\frac{1}{r}\frac{\partial}{\partial r}\left(r\frac{\partial}{\partial r}\right)-\frac{n^2}{r^2}\right]\hat{\psi}^{(q)}=\frac{\hat{\zeta}_o}{q+ian/r^2}. \qquad (B4.19)$$

Noting that the Laplace transform of $\exp(-iant/r^2)$ is $1/(q+ian/r^2)$, the inverse Laplace transform of ($B4.19$) yields

$$\left[\frac{1}{r}\frac{\partial}{\partial r}\left(r\frac{\partial}{\partial r}\right)-\frac{n^2}{r^2}\right]\hat{\psi}=\hat{\zeta}_o e^{-iant/r^2}. \qquad (B4.20)$$

The Green's function method will now be used to solve ($B4.20$). The equation is first put in standard form by multiplying by r, giving

$$\left[\frac{\partial}{\partial r}\left(r\frac{\partial}{\partial r}\right)-\frac{n^2}{r}\right]\hat{\psi}=r\hat{\zeta}_o e^{-iant/r^2}. \qquad (B4.21)$$

Recalling that the azimuthal gradient of the streamfunction must vanish on the boundaries in physical space, the corresponding Fourier-space boundary conditions are then $\hat{\psi}(a) = \hat{\psi}(b) = 0$.

The Green's function is defined as the solution to

$$\left[\frac{\partial}{\partial r}\left(r\frac{\partial}{\partial r}\right) - \frac{n^2}{r}\right] G(r,\rho) = \delta(r-\rho). \tag{B4.22}$$

If $r \neq \rho$, equation (B4.22) is the homogeneous Euler's equation and the general solution in each region is

$$G(r,\rho) = \begin{cases} Ar^n + Br^{-n}, & a \leq r < \rho \\ Cr^n + Dr^{-n}, & \rho < r \leq b. \end{cases} \tag{B4.23}$$

Thus far, only two conditions have been specified for the problem. Two more are needed to uniquely determine $G(r,\rho)$. Since $\hat{\psi}$ is continuous, the Green's function is required to be continuous at $r = \rho$. On integrating over a small interval about ρ, equation (B4.22) becomes

$$(\rho+\epsilon)\frac{\partial G}{\partial r}(\rho+\epsilon,\rho) - (\rho-\epsilon)\frac{\partial G}{\partial r}(\rho-\epsilon,\rho) - \int_{\rho-\epsilon}^{\rho+\epsilon} \frac{n^2}{r} G(r,\rho)\, dr = 1. \tag{B4.24}$$

Since $G(r,\rho)$ is bounded on the integration interval, the integral in (B4.24) vanishes as ϵ goes to zero, yielding

$$\frac{\partial G}{\partial r}(\rho^+,\rho) - \frac{\partial G}{\partial r}(\rho^-,\rho) = \frac{1}{\rho}. \tag{B4.25}$$

The Green's function is uniquely determined by imposing the slippery boundary conditions, continuity of $G(r,\rho)$ at $r = \rho$, and the jump condition (B4.22). This gives

$$G(r,\rho) = \frac{1}{2nr^n(a^{2n} - b^{2n})} \begin{cases} (\rho^n - b^{2n}\rho^{-n})(a^{2n} - r^{2n}), & a \leq r \leq \rho \\ (\rho^n - a^{2n}\rho^{-n})(b^{2n} - r^{2n}), & \rho \leq r \leq b. \end{cases} \tag{B4.26}$$

It is easily verified that $G(r,\rho) = G(\rho,r)$. Thus, in an analogous manner to chapter 2, the solution to (B4.21) is

$$\hat{\psi}(r) = \int_a^b G(r,\rho)\hat{\zeta}_o(\rho) e^{-iant/\rho^2}\, \rho d\rho. \tag{B4.27}$$

In the previous chapters, only initial vorticity profiles of the form $\hat{\zeta}_o = f(y)\delta(k_* - k)$ were considered. This allowed examination of the perturbation evolution on a wavenumber by wavenumber basis. A similar strategy is employed here. The initial vorticity will be restricted to functions of the form $\hat{\zeta}_o = f(r)\delta(n_* - n)$ where δ is the Kronecker delta. The effect on the integration will be

the same as in the previous chapters. The δ maps n into n_* when the inverse Fourier transform is applied. For notational simplicity, the variable n is used to refer to the wavenumber in both physical and Fourier space. With this convention, the inverse Fourier transform of equation (B4.27) is

$$\psi_n = e^{in\lambda} \int_a^b G(r,\rho)\hat{\zeta}_o e^{-iant/\rho^2}\, \rho d\rho. \tag{B4.28}$$

Since exact solutions to (B4.28) cannot generally be found, the trapezoidal rule is used as the solution method throughout the remainder of the chapter. Note also that the initial condition in (B4.28) is expressed in terms of the initial vorticity. Hereafter, the terms initial vorticity and initial condition will be used interchangeably. Finally, the locations of the boundaries are set at $a = 1$ and $b = 10$.

4.3 Initial Conditions

In order to gain insight into the asymmetric dynamics that are applicable to hurricanes and other rapidly rotating vortices, initial vorticity profiles are needed that represent physical processes relevant in such vortices. CW motivate four classes of initial conditions. Their analysis is outlined below. Consider two-dimensional incompressible inviscid vorticity dynamics on a β-plane. In ground-based coordinates, the governing equation is

$$\frac{\partial \zeta}{\partial t} + \vec{V} \cdot \nabla(\zeta + f) = 0 \tag{B4.29}$$

where ζ is the vertical component of the vorticity, $\vec{V}$ is the horizontal wind vector, and f is the Coriolis parameter given by

$$f = f_o + \beta y. \tag{B4.30}$$

Here β is the linearized latitudinal derivative of the Coriolis parameter at a reference latitude and f_o is the reference value of f. Equation (B4.29) may be transformed into a coordinate system moving with the storm center through

$$\nabla = \nabla', \tag{B4.31}$$

$$\frac{\partial}{\partial t} = \frac{\partial'}{\partial t} - \vec{C} \cdot \nabla', \tag{B4.32}$$

where $\vec{C}(t)$ is the storm motion vector and the primes denote operations with respect to coordinates in the moving frame.

The velocity is now partitioned into three parts

$$\vec{V} = \vec{V}_s + \vec{V}_e + \vec{V}_a \tag{B4.33}$$

subject to the following definitions: (a) $\vec{V}_s$ is a known symmetric flow that is steady in the moving reference frame, (b) $\vec{V}_e$ is a known zonal environmental flow that depends only on latitude and is steady in the stationary reference frame, and (c) $\vec{V}_a$ is an asymmetric flow that represents unknown perturbations to the symmetric flow. Using these definitions, the vorticity equation in the moving reference frame is

$$\frac{\partial' \zeta_a}{\partial t} + (\vec{V}_s + \vec{V}_e - \vec{C}) \cdot \nabla' \zeta_a + (\vec{V}_a - \vec{C}) \cdot \nabla' \zeta_s + \vec{V}_a \cdot \nabla' (\zeta_a + \zeta_e + f') = -\vec{V}_s \cdot \nabla' (\zeta_e + f') - \vec{V}_e \cdot \nabla' \zeta_s. \tag{B4.34}$$

The terms have been grouped so that external processes which act to generate ζ_a appear as forcing terms on the right side of (B4.34).

The initial vorticity perturbations are obtained by examining the forcing terms in component form. CW define the vectors as follows:

$$\vec{V}_s = v_s(r)\vec{\lambda}, \tag{4.35a}$$

$$\vec{V}_e = u_e(y)\vec{i}, \tag{4.35b}$$

$$\vec{C} = C[\cos(\lambda - \alpha)\vec{r} - \sin(\lambda - \alpha)\vec{\lambda}], \tag{4.35c}$$

where $\vec{i}$, $\vec{r}$, and $\vec{\lambda}$ are the zonal, radial, and azimuthal unit vectors, respectively. The angle α is the direction of the storm's motion following the convention of Willoughby (1988). CW note that asymmetries can be forced by the term $-\vec{C} \cdot \nabla' \zeta_s$ which is the advection of the symmetric vorticity by the storm's motion. Grouping this term with the other forcing terms, the vorticity tendency in Cartesian coordinates due to these forcings is

$$\frac{\partial' \zeta_a}{\partial t} \propto -v_s \left(\frac{\partial \zeta_e}{\partial y} + \beta \right) \cos\lambda - (u_e - c_x) \frac{\partial \zeta_s}{\partial r} \cos\lambda + c_y \frac{\partial \zeta_s}{\partial r} \sin\lambda \tag{B4.36}$$

where $c_x = C\cos\alpha$ and $c_y = C\sin\alpha$. To assess the radial structure of the forced response, consider the truncated Taylor series expansion of u_e about the position of storm's center

$$u_e(y) = u_e(0) + S_e y - \frac{1}{2}\beta_e y^2 \tag{B4.37}$$

where

$$S_e = \left.\frac{\partial u_e}{\partial y}\right|_{y=0}, \tag{4.38a}$$

$$\beta_e = -\left.\frac{\partial^2 u_e}{\partial y^2}\right|_{y=0}. \tag{4.38b}$$

The scaling for v_s and $d\zeta_s/dr$ may be identified by examining the modified Rankine profile

$$v_s = V_m\left(\frac{R_m}{r}\right)^X. \tag{B4.39}$$

The radial derivative of ζ_s is then

$$\frac{\partial\zeta_s}{\partial r} = (X^2-1)\frac{V_m R_m^X}{r^{X+2}}. \tag{B4.40}$$

The Rankine profile used in this chapter is recovered by setting $X = 1$ in (B4.39). In order to have a nontrivial scaling on (B4.40), however, X cannot be exactly one. It is assumed that for X very close to one, the vorticity gradient will be sufficiently small that the perturbation evolution will be essentially unaffected. Thus, equation (B4.40) becomes

$$\frac{\partial\zeta_s}{\partial r} \approx (X^2-1)\frac{V_m R_m}{r^3}. \tag{B4.41}$$

Examining the first term on the right side of (B4.36), substituting (B4.38b) and (B4.39) gives

$$\frac{\partial\zeta_a}{\partial t} \propto -\frac{V_m R_m}{r}(\beta+\beta_e)\cos\lambda. \tag{B4.42}$$

This represents the generation of wavenumber one asymmetry due to the advection of absolute environmental vorticity (the β terms) by the symmetric vortex. CW refer to this as the 'β-induced asymmetry'. An equivalent nondimensional intial condition is then

$$\hat{\zeta}_o = -\frac{1}{r}, \qquad n = 1. \tag{B4.43}$$

Examining the second term on the right side of (B4.36), substituting the first two terms of (B4.37) and (B4.41) gives

$$\frac{\partial \zeta_a}{\partial t} \propto (1 - X^2) V_m R_m \left[\frac{(u_e - c_x)}{r^3} \cos\lambda + \frac{S_e}{2r^2} \sin 2\lambda \right] \tag{B4.44}$$

where the identities $y = r\sin\lambda$ and $2\sin\lambda\cos\lambda = \sin 2\lambda$ have been used. This represents the generation of a wavenumber one asymmetry due to the vortex motion relative to the environmental wind and a wavenumber two asymmetry due to the linear shearing of the symmetric vortex by the relative environmental wind. CW refer to these as the 'motion-induced' and 'shear-induced' asymmetries, respectively. Equivalent nondimensional initial conditions are then

$$\hat{\zeta}_o = \frac{1}{r^3}, \qquad n = 1; \tag{B4.45}$$

$$\hat{\zeta}_o = -\frac{i}{r^2}, \qquad n = 2. \tag{B4.46}$$

The last initial condition used by CW was motivated by a desire to have exact solutions to (B4.28). By making the substitution $\mu = 1/\rho^2$, it can be shown that an initial vorticity profile of the form

$$\hat{\zeta}_o = 1/r^{n+4} \tag{B4.47}$$

admit analytical solutions to the integration (cf. equations (30) and (31) in CW). These initial vorticity perturbations are radially confined to the inner boundary and may be physically interpreted as asymmetries forced by convection in the eyewall of tropical cyclones. CW refer to these as 'convection-induced' asymmetries.

4.4 Model Results

Since one of the objectives of this thesis was to address some of the unresolved issues of the CW paper, a necessary first step was to be able to reproduce their results. Although their stream-function fields were easily reconstructed, the integrated kinetic energy plots associated with the four initial conditions developed in the previous section were not reproduced exactly. Figure 4.2 is a reproduction of figure 4a from CW while figure 4.3 shows the results from this work. Although the

trends are the same, the magnitudes and shapes of the curves are different. Specifically, CW show a more rapid energy decay for 'convection-induced' initial conditions and a more abrupt transition to the asymptotic behavior. The conclusions CW draw from their figure, however, are essentially qualitative in nature and can still be obtained from figure 4.3.

CW provide little information about the numerical model used to generate their results. It is likely, then, that the conditions of their experiments have not been exactly duplicated. However, we are confident that the results presented in this thesis are robust. The numerical results here have been verified to satisfy the momentum and mass conservation equations to within the discretization error associated with the trapezoidal rule. Moreover, as the model resolution was increased, the results were quadratically convergent (see Appendix B).

In their paper, CW restrict attention to the initial vorticity profiles developed in the previous section. While physically motivated, they change both the radial structure and the azimuthal wavenumber simultaneously. Using the CW initial conditions as a reference, initial vorticity profiles where only one parameter changes at a time are considered.

Figure 4.4 shows the streamfunction fields for an upright initial vorticity distribution $\hat{\zeta}_o = 1/r^3$ and figure 4.5 shows the corresponding vorticity fields. The rows represent wavenumbers $n = 1$, 2, and 3, respectively, while the columns designate times $t = 0.0$, 3.6, and 7.2, respectively. These figures show that, with respect to increasing the time or the wavenumber, the rectilinear and swirling problems behave similarly. This is not surprising as the Green's function and the phase function are formally identical between the rectilinear and swirling cases.

While the mathematical solutions are qualitatively similar between the rectilinear and swirling cases, there are physical differences in the disturbance evolution between the two systems. Figure 4.6 shows the energy decay in the rectilinear problem for the initial condition $\hat{\zeta}_o = -1/(y-11)^3$. Figure 4.7 shows the energy decay in the swirling problem for $\hat{\zeta}_o = 1/r^3$. These plots show that, on a wavenumber by wavenumber basis, the energy decays more slowly in the swirling problem than in the rectilinear case. In addition, the figures suggest that the difference between the wavenumber one disturbance and the higher wavenumber disturbances is more pronounced in the swirling problem.

These differences are explained by examining how the shear acts in each system.

In the rectilinear problem considered in chapter 2, the shear is constant an defines limiting values for the energy decay of the perturbation. In particular, the limiting energy decay is given by $1/[1+(St)^2]$. Thus, the limiting time for a perturbation to decay to half its initial energy is $t = 1/S$, the half-life time. In the swirling problem, however, the shear varies radially and is only a local measure of the flow. In order to investigate the limiting integrated energy decay of asymmetries, a global measure of the shear is required.

In simple shear and in the bounded Rankine vortex, the physical process governing disturbance evolution is the conservation of vorticity following the basic state flow. In the rectilinear problem of chapter 2, the perturbation vorticity is advected by $\bar{u}$, the basic state zonal wind. The corresponding shear is thus $d\bar{u}/dy$. Since the shear is constant, the meridional scale of the perturbation qualitatively describes the decay rate for a constant zonal wavenumber. The change in the zonal wind across a large-scale perturbation is greater than the corresponding change across a small-scale perturbation. Thus, the large-scale disturbances decay more rapidly.

In the swirling problem, the disturbance vorticity is advected by $\bar{v}/r$, the basic state angular velocity. The corresponding local shear is $rd\bar{\Omega}/dr$ (SM) where $\bar{\Omega} = \bar{v}/r$. In a Rankine vortex, $\bar{\Omega}$ is equal to $1/r^2$ and the local shear is equal to $-2/r^2$. Since the angular velocity does not describe solid body rotation, both the radial location and the radial structure of the asymmetry are needed to describe the decay rate. A plausible candidate for an effective shear that satisfies these conditions is

$$S_{\text{eff}} = \frac{\int_a^b r\frac{d\bar{\Omega}}{dr}\hat{\zeta}_o\,dr}{\int_a^b \hat{\zeta}_o\,dr}. \qquad (B4.48)$$

The analogous expression in the rectilinear problem reduces to the simple shear definition if $d\bar{u}/dy$ is constant. For initial conditions of the form $1/r^\alpha$, the effective shear is found to be

$$S_{\text{eff}} = -\frac{2(\alpha-1)}{ab^2(\alpha+1)}\left[\frac{a^{\alpha+1}-b^{\alpha+1}}{a^{\alpha-1}-b^{\alpha-1}}\right], \qquad \alpha \neq 1; \qquad (4.49a)$$

$$S_{\text{eff}} = \frac{a^2-b^2}{ab^2\ln(b/a)}, \qquad \alpha = 1. \qquad (4.49b)$$

Appealing to the rectilinear case, the effective shear should define limiting values for the decay rate

of asymmetries. In particular, the limiting energy decay should be given by $1/[1 + (S_{\text{eff}}t)^2]$. Thus, the limiting asymmetry half-life time should be $t = -1/S_{\text{eff}}$. The limiting energy decay curve is the solid line in figure 4.7.

Figure 4.8 shows the integrated energy as a function of time for azimuthal wavenumber $n = 1$ and vorticity profiles $\hat{\zeta}_o = 1/r^\alpha$ where $\alpha = 3$, 4, 5, and 6. Figure 4.8 confirms the expected behavior for the $1/r^3$ and $1/r^4$ asymmetries. However, the decay rates for the $1/r^5$ and $1/r^4$ asymmetries are nearly identical until $t \approx 5.5$. In addition, the decay rate for the $1/r^6$ asymmetry is less than that for the $1/r^4$ asymmetry until $t \approx 8.0$ and is less than the decay rate for the $1/r^5$ asymmetry for the times plotted. Thus, for initial conditions tightly confined to the inner boundary, there is a transient period when the decay rate decreases with decreasing disturbance scale. This resembles the rectilinear problem. The decay rate eventually reverts back to increasing with decreasing disturbance scale though the cross-over time is later for smaller-scale disturbances.

This duality may be qualitatively explained as follows. Initially, most of the kinetic energy in the asymmetry is concentrated near the inner boundary. The radial change in the energy is so large that the basic state angular velocity appears constant in a first approximation. Thus, as in the rectilinear problem, decreasing the disturbance scale results in a decrease of the decay rate. However, the inner portion of the asymmetry is symmetrized more rapidly than that farther out in the vortex. The kinetic energy near the inner boundary is transferred to the basic state much faster than the kinetic energy in the storm's environment. The cross-over time occurs when the inner core energy decays to the same magnitude as the environmental energy. At this time, the basic state angular velocity no longer appears constant. The cross-over time is later for smaller-scale disturbances because it takes longer for the inner core kinetic energy to decay to environmental kinetic energy values.

The initial vorticity profiles considered thus far represent forcings that act nearly continuously in a hurricane. It is also of interest to investigate transient forcings that act in hurricanes, such as an upper-level short-wave trough or a tropical easterly wave. As a proxy for such forcings, consider a Gaussian initial vorticity profile of fixed radial scale. As the vorticity maximum is moved toward the vortex center, the effective shear and the decay rate increases due to the increase in the differential

rotation.

The Gaussian initial vorticity profiles considered in this work have been initially upright with respect to the local shear. Consequently, such disturbances have only had a decay phase. However, migratory short-wave troughs, upon encountering a tropical system, are generally not upright with respect to the local shear. As an example, consider a trough positioned 300 km east of a tropical cyclone in the Northern Hemisphere. Let the trough axis be oriented 30 degrees east of north such that the trough leans against the local shear. Recall from chapter 2 that disturbances leaning against the shear grow at the expense of the basic state. Thus, while the trough leans against the shear, the trough will intensify and the tropical cyclone will weaken. As the trough grows, it rotates counter clockwise and becomes maximum when it is oriented north-south. Once the trough is upright with respect to the local shear, further evolution results in the trough weakening and the tropical cyclone intensifying.

Figures 4.9, 4.10, and 4.11 show the asymmetry half-life times for initial vorticity profiles of $1/r^2$, $1/r^3$, and $1/r^5$. For each of these profiles, the $n = 1$ asymmetry clearly decays more slowly than all higher wavenumber asymmetries. The dotted line in each plot is the asymmetry half-life time $-1/S_{\text{eff}}$ for the given initial condition. For the lower wavenumbers, $-1/S_{\text{eff}}$ significantly underestimates the asymmetry half-life time. For the $1/r^3$ and $1/r^5$ profiles, the $-1/S_{\text{eff}}$ line adequately defines the asymptotic limit of the half-life time for the higher wavenumbers. This suggests that the S_{eff} definition of this chapter is applicable to asymmetries which fall off in radius more rapidly than the basic state angular velocity. This conclusion has been verified for Gaussian initial conditions.

The above results refute an assertion made by CW. Based on closed form solutions obtained for the convection-induced asymmetries (cf. CW equations (30) and (31)), CW argue that the asymmetry damping rate should be proportional to the square of the wavenumber. If their assertion was correct, then as $n \to \infty$, the damping rate should also become infinite. Thus, the half-life time should asymptote to zero. However, the asymmetry half-life plots show that for increasing n, the time required for the energy to decay to half its initial value approaches a nonzero constant and does not decrease as $1/n^2$.

4.5 Application to Hurricanes

The definition for the effective shear presented in the previous section need not be restricted to the Rankine vortex. Here the effective shear is evaluated for the analytical profiles $\bar{v} = 1/r^{\alpha}$ where $\alpha = 1/3$, $1/2$, and $2/3$. These profiles are better approximations of the symmetric tangential winds typically observed in hurricanes than is the Rankine vortex. The effective shear is also calculated for the observed 700 mb winds in hurricane Gloria (Montgomery, personal communication, 1994) which occurred in 1985. The Gloria data are nondimensionalized using $V_m = 57.91$ ms^{-1} and $R_m = 20$ km corresponding to Gloria's maximum tangential wind and radius of maximum winds, respectively. The Gloria winds are given at 10 km intervals and are considered out to 500 km from the storm center. Thus, for a nondimensional inner boundary set at $a = 1$, the corresponding outer boundary is at $b = 25$. Figure 4.12 shows the Gloria and analytical symmetric tangential winds.

Since the effective shear calculation also requires the specification of initial vorticity profiles, three types of initial conditions are considered here. The first is a convectively forced asymmetry and is confined tightly to the radius of maximum winds. The second is shear-induced asymmetry which is also confined to the inner boundary but extends farther out into the vortex than the convection-induced asymmetry. The final initial condition corresponds to a trough in the environment of the vortex several hundred kilometers from the vortex center. Mathematically, these initial conditions are given by $\hat{\zeta}_o = 1/r^5$, $1/r^2$, and $\exp(-(r-15)^2)$, respectively.

Table 4.1 shows values of S_{eff} and $-1/S_{\text{eff}}$ for the initial voticity profiles and symmetric wind profiles above. The values have been dimensionalized using the Hurricane Gloria data cited above. The asymmetry half-life times given by $-1/S_{\text{eff}}$ are underestimates of the decay rate. Examination of figures 4.9, 4.10, and 4.11 indicate the $n = 1$ asymmetry decays approximately seven times slower than the limiting time-scale. Assuming that the $n = 1$ decay rate approximates the decay rate for an atmospheric disturbance, the asymmetries forced in the inner region of a hurricane give up half their initial energy in 35-70 minutes for the analytical symmetric winds. The table suggests that similar asymmetries in Hurricane Gloria gave up half their initial energy in 40-60 minutes. The Gaussian initial vorticity here represents a trough 300 km from the storm center. This feature decays to half

its initial energy in 17-35 hours for the analytical symmetric winds. The table suggests that similar asymmetries in Hurricane Gloria gave up half their initial energy in 14 hours.

4.6 Summary

Wave disturbances on a symmetric vortex have been shown to favor the lower wavenumber asymmetries. Disturbances evolve in a similar fashion to their rectilinear counterparts for changes in the wavenumber and in time. However, the disturbance evolution for changing radial structure is complicated by the change in the basic state angular velocity with radius. In addition to the radial scale, the radial location of the initial asymmetry must be known.

For asymmetries forced in the inner core region of the vortex, decreasing the radial scale of the asymmetry increases the effective shear and the decay rate when the environmental portion of the kinetic energy is comparable to the inner core portion. When the asymmetry is tightly confined to the inner boundary, the kinetic energy near the inner core dominates. The effective shear appears constant and further narrowing of the radial scale results in a decreasing decay rate. This transient behavior lasts until the kinetic energy near the inner core is reduced to levels comparable to the environmental kinetic energy. For asymmetries forced in the environment of the vortex, increasing the radial scale of the asymmetry or moving a fixed scale asymmetry towards the inner boundary results in an increase of the effective shear and the decay rate.

Since the shear varies with radius, an integrated measure of the shear is needed to estimate the global evolution of asymmetries. The shear definition presented here considers both the basic state angular velocity and the initial vorticity profile. Noting that the reciprocal of the rectilinear shear defined the limiting time for a perturbation to decay to half its initial energy, the reciprocal of the effective shear was expected to define the limiting asymmetry half-life time. This time scale significantly underestimated the decay rate for the lower azimuthal wavenumbers for all initial conditions considered. However, the decay time scale $-1/S_{\text{eff}}$ reasonably represented the asymptotic limit of the asymmetry half-life times for the higher wavenumbers as long as the initial condition fell off in radius more rapidly than the basic state angular velocity.

Table 4-1: Effective shear values and limiting asymmetry half-life times for various symmetric wind profiles. Symmetric wind data from the 700 mb level of Hurricane Gloria are also considered. All values have been dimensionalized using Gloria's maximum azimuthal wind (57.91 ms^{-1}) and the radius of maximum winds (20 km).

		$\hat{\zeta}_o$		
		$1/r^5$	$1/r^2$	$e^{(r-15)^2/10}$
$\bar{v}$	$1/r^{1/3}$	-2.81×10^{-3} s^{-1}	-1.77×10^{-3} s^{-1}	-1.09×10^{-4} s^{-1}
		5.94 min	9.44 min	2.56 hr
	$1/r^{1/2}$	-3.06×10^{-3} s^{-1}	-1.86×10^{-3} s^{-1}	-7.83×10^{-5} s^{-1}
		5.45 min	8.96 min	3.55 hr
	$1/r^{2/3}$	-3.29×10^{-3} s^{-1}	-1.94×10^{-3} s^{-1}	-5.59×10^{-5} s^{-1}
		5.07 min	8.58 min	4.97 hr
	Gloria	-2.89×10^{-3} s^{-1}	-1.81×10^{-3} s^{-1}	-1.29×10^{-4} s^{-1}
		5.76 min	9.23 min	2.15 hr

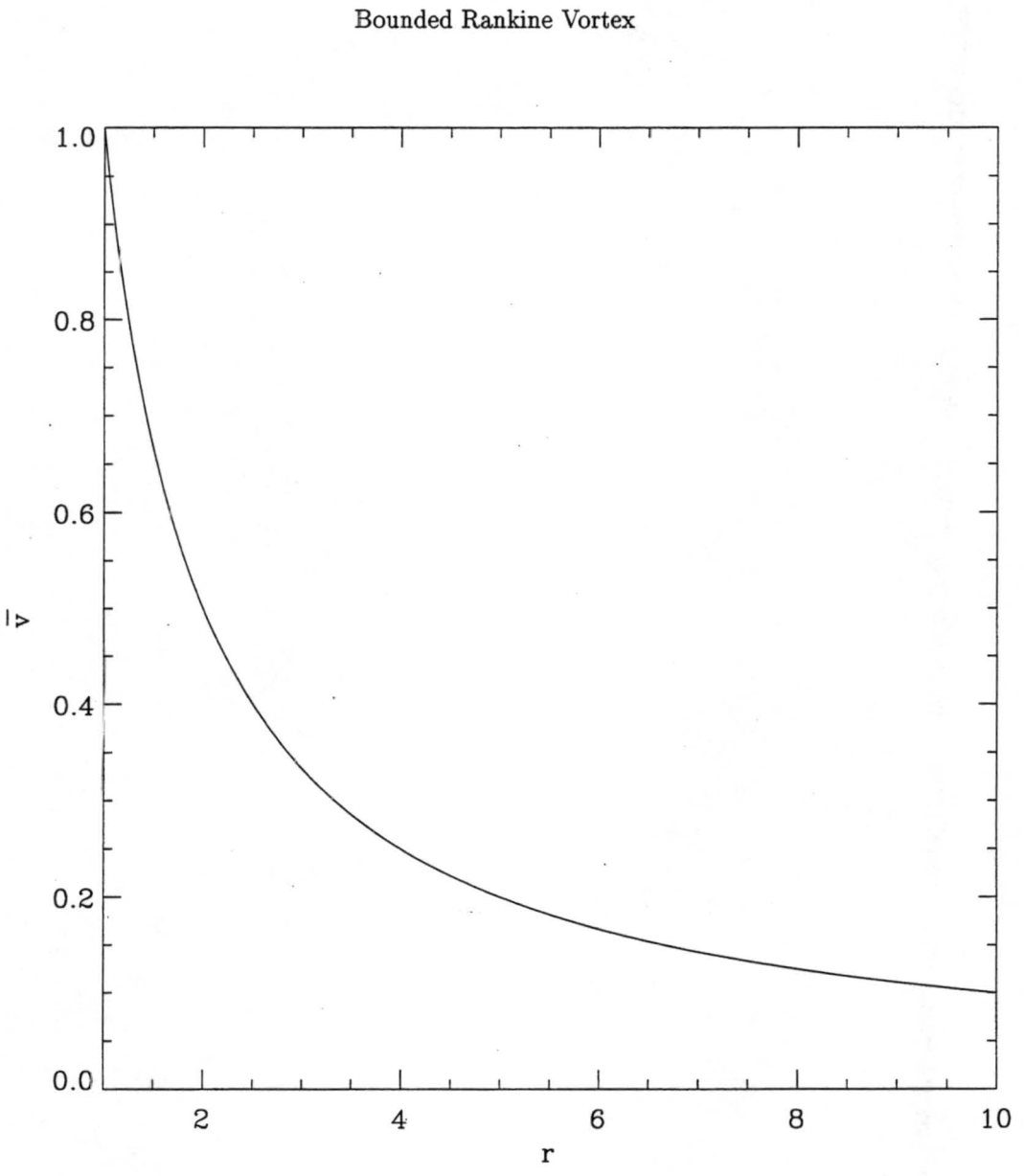

Fig. 4.1: The nondimensionalized bounded Rankine vortex.

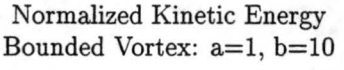

Fig. 4.2: Figure 4.(a) from the Carr and Williams (1989) paper. It is a plot of the normalized kinetic energy as a function of time for the four initial conditions developed in their paper. The curves are the energy decay for: convection-induced ($n = 2$, dot; $n = 1$ dash), motion-induced (chaindot), and shear-induced (chaindash) asymmetries.

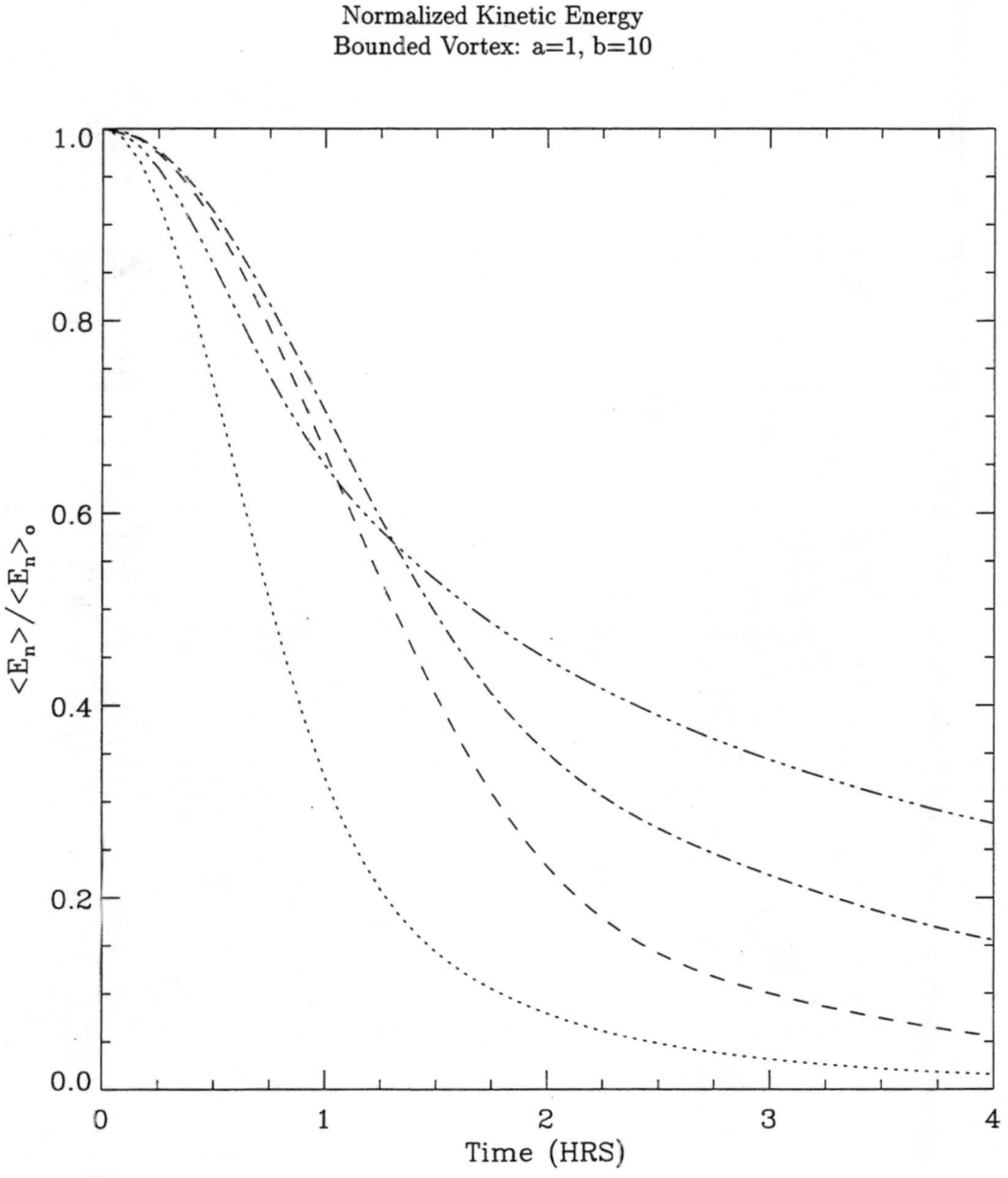

Fig. 4.3: Normalized kinetic energy as a function of time for the four initial conditions developed by Carr and Williams (1989). The curves are the energy decay for: convection-induced ($n = 2$, dot; $n = 1$, dash), motion-induced (dot dash), and shear-induced (dot dot dot dash) asymmetries.

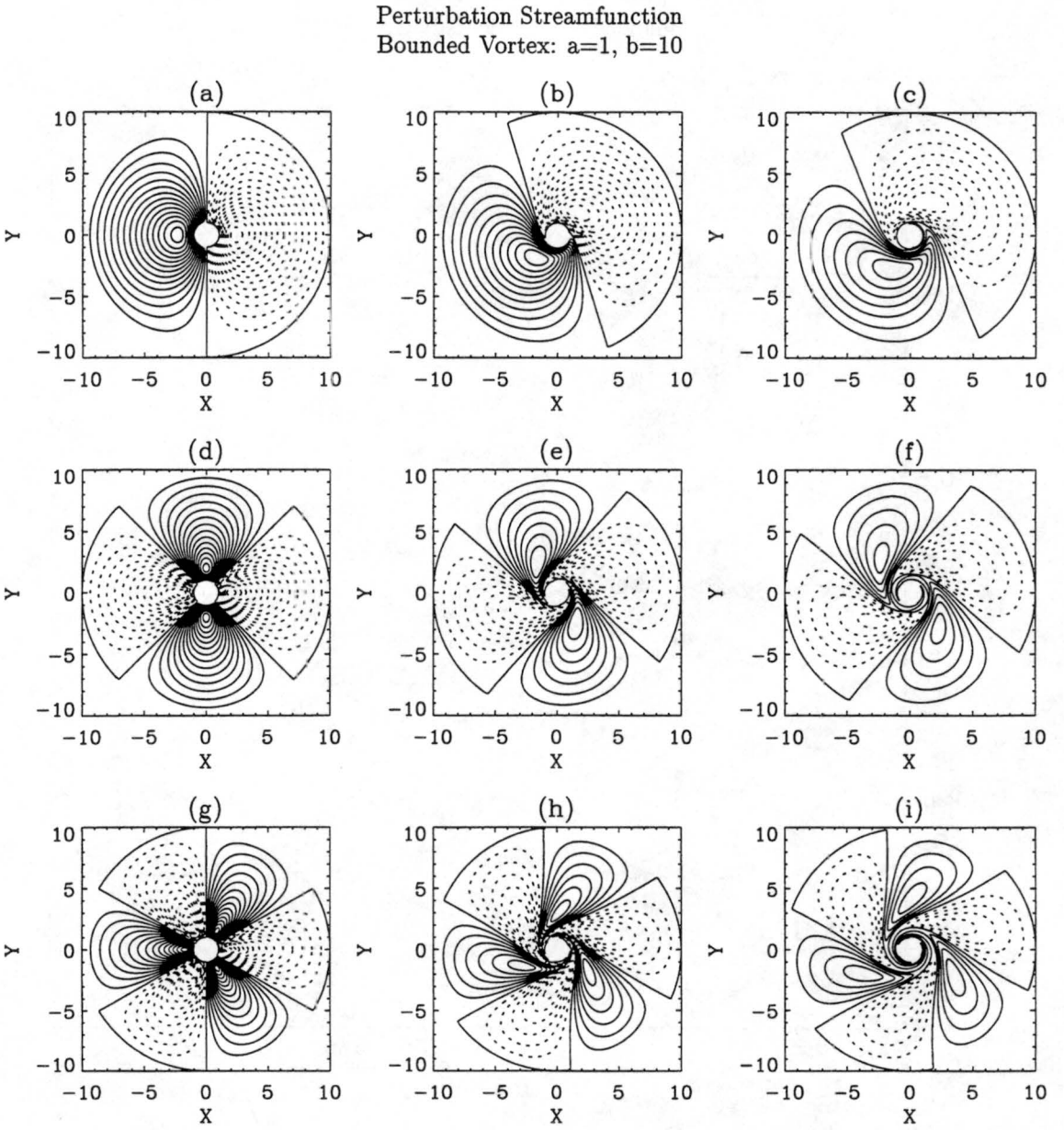

Fig. 4.4: Perturbation streamfunction field for $\hat{\zeta}_o = 1/r^3$ for the bounded Rankine vortex. The columns show contours at times $t = 0.0$, $t = 3.6$, and $t = 7.2$, respectively. Panels (a)-(c) show contours for $n = 1$ where the contour interval is 1.10×10^{-2}. Panels (d)-(f) show contours for $n = 2$ where the contour interval is 5.67×10^{-3}. Panels (g)-(i) show contours for $n = 3$ where the contour interval is 3.31×10^{-3}.

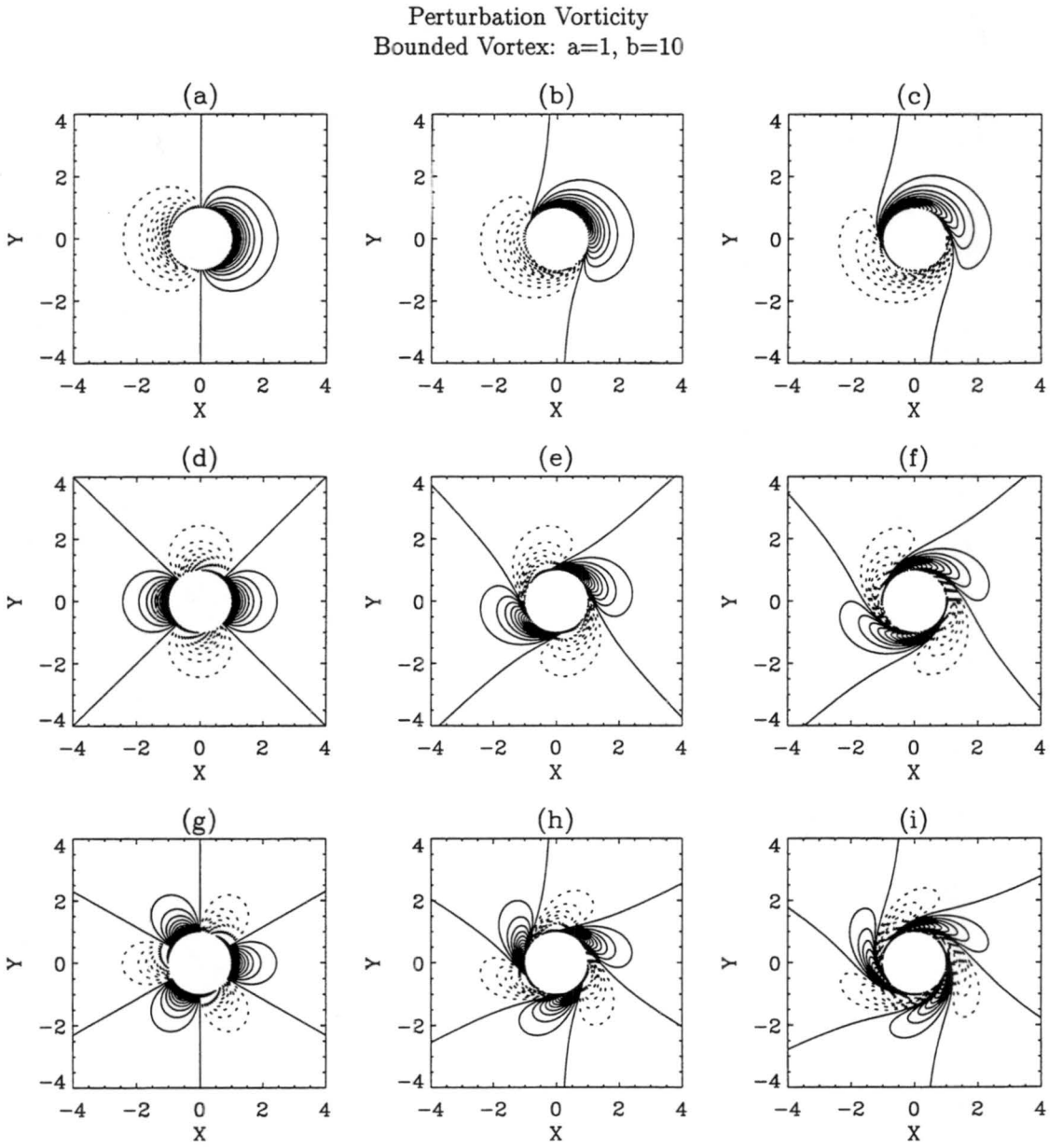

Fig. 4.5: Perturbation vorticity field corresponding to figure 4.4. Note the different axis scales. The contour interval is 6.90×10^{-2}.

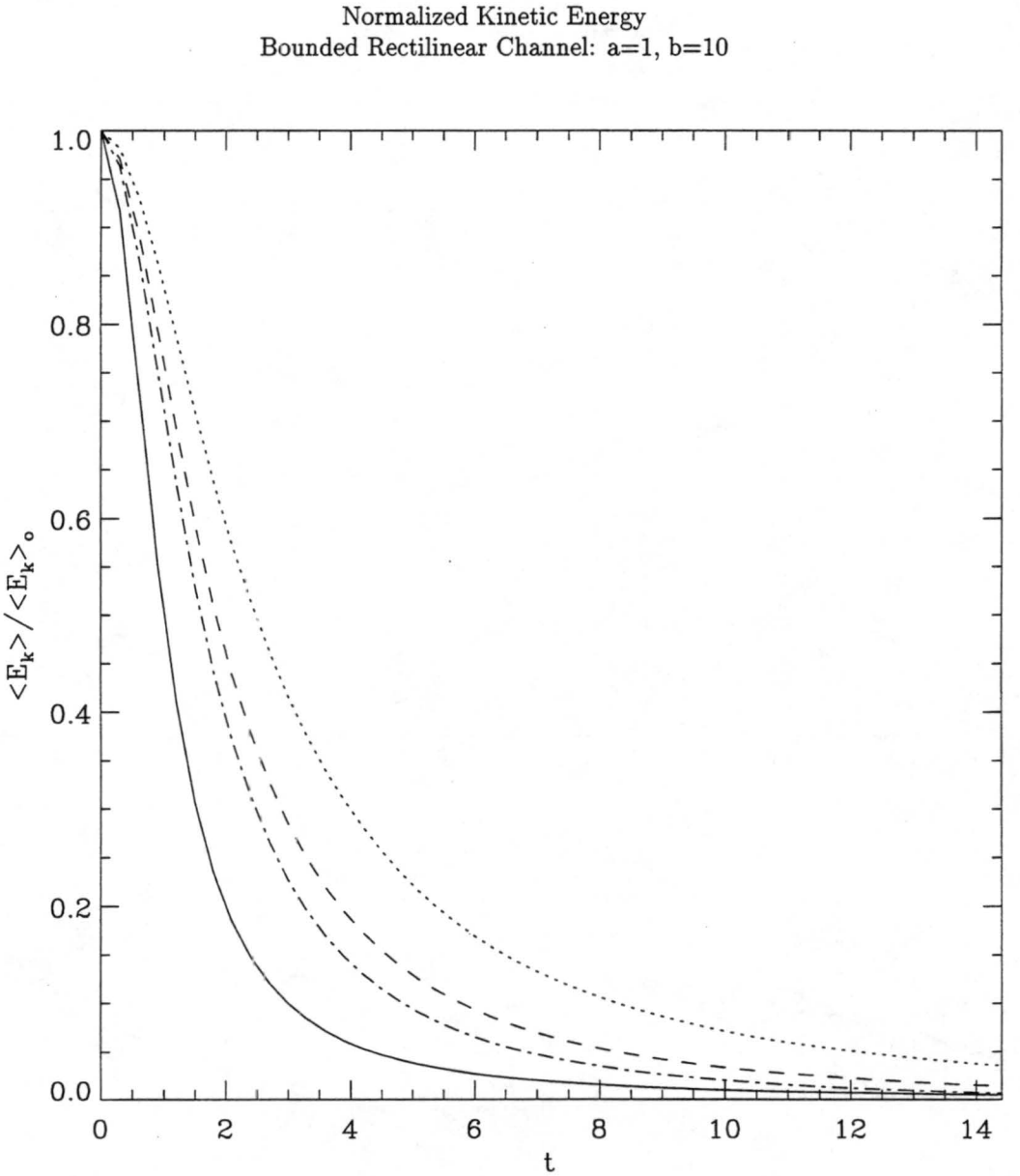

Fig. 4.6: Normalized kinetic energy for the rectilinear problem with $\hat{\zeta}_o = -1/(y-11)^3$. The curves are the energy decay for: $k = 1$ (dot), $k = 2$ (dash), $k = 3$ (dot dash). The solid curve is the energy decay for the upright plane wave given by $1/(1+t^2)$.

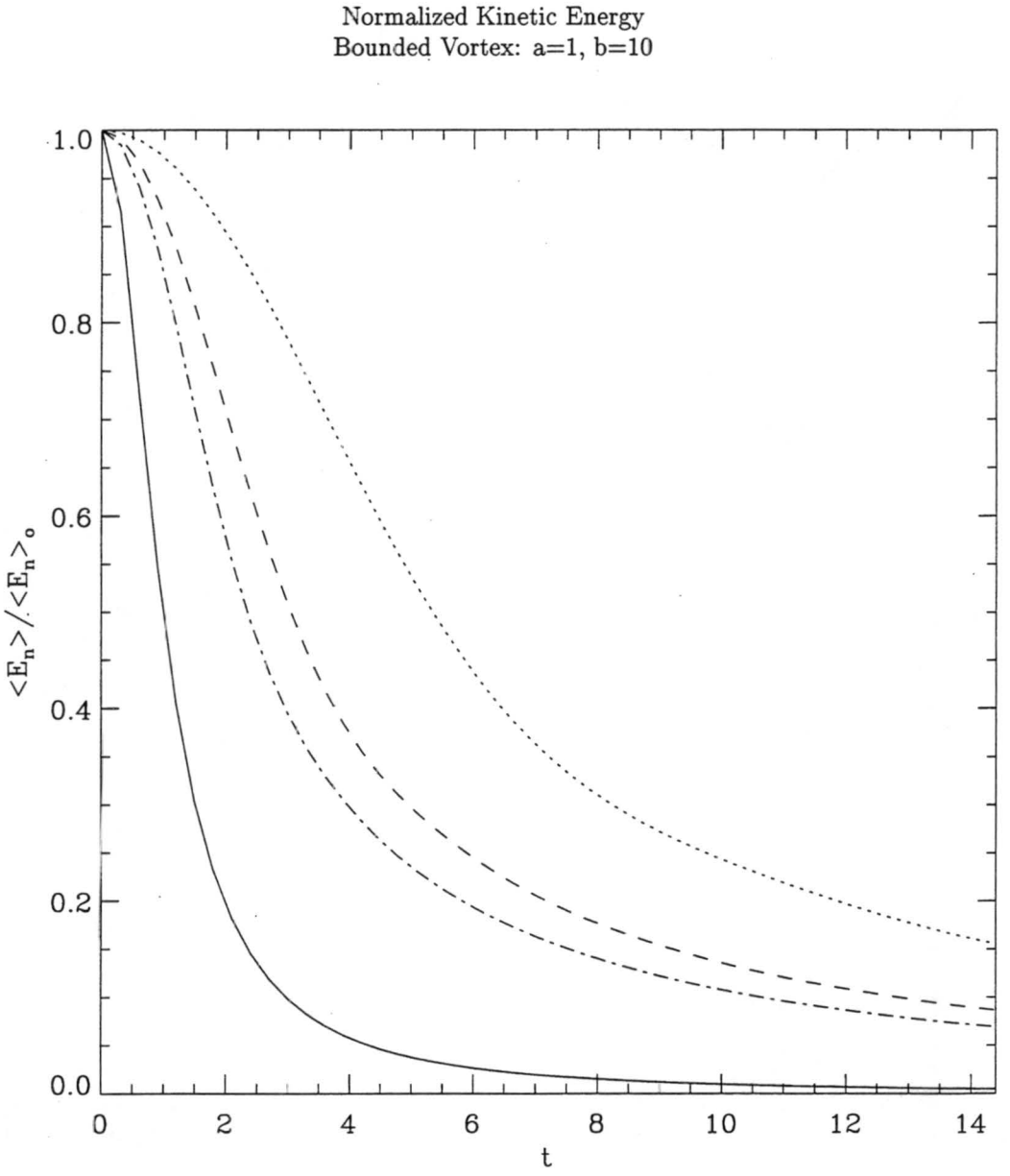

Fig. 4.7: Normalized kinetic energy for the bounded Rankine vortex with $\hat{\zeta}_o = 1/r^3$. The curves are the energy decay for: $n = 1$ (dot), $n = 2$ (dash), $n = 3$ (dot dash). The solid curve is the limiting energy decay given by $1/[1 + (S_{\text{eff}}t)^2]$ where $S_{\text{eff}} = -1.01$.

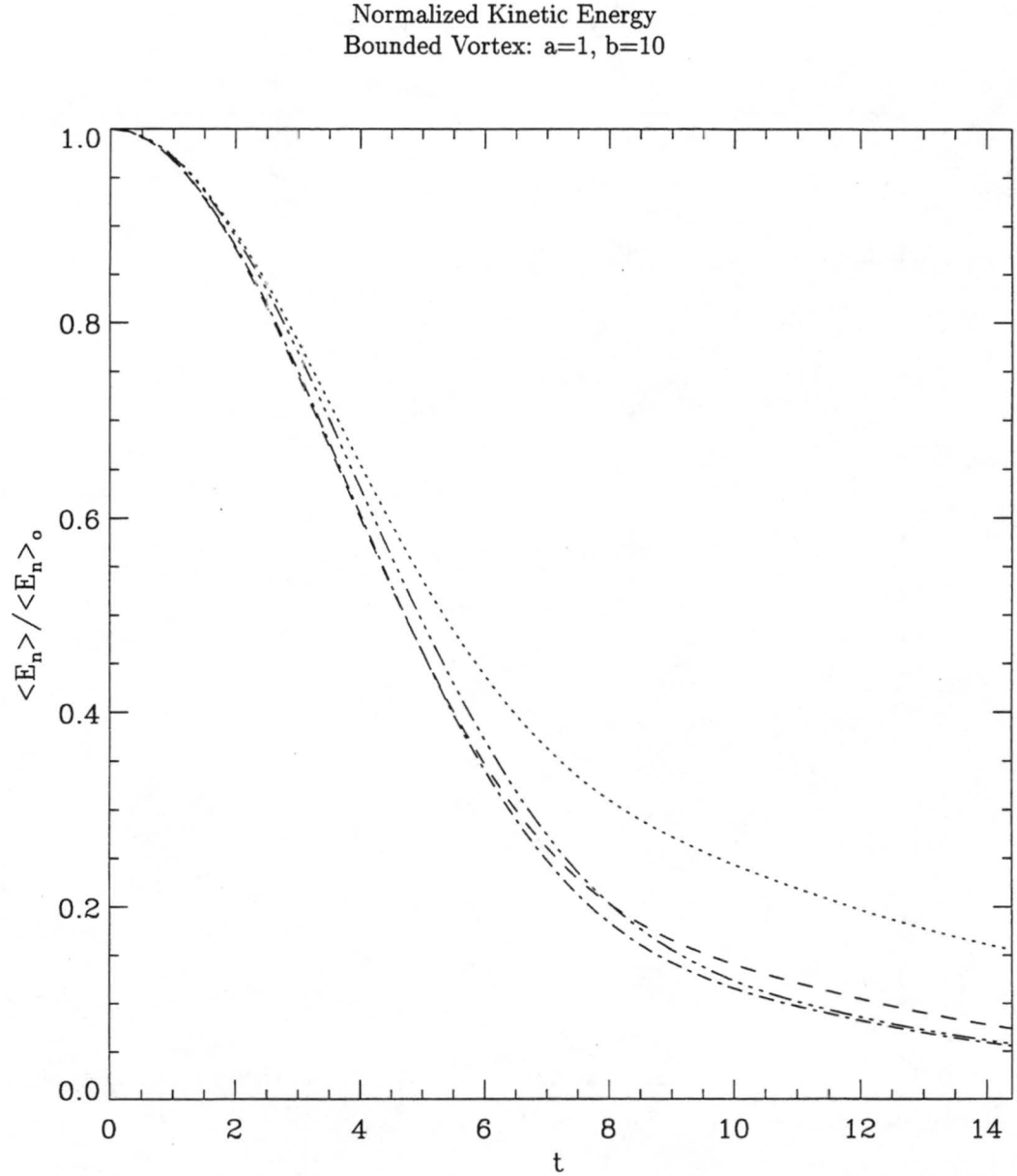

Fig. 4.8: Normalized kinetic energy for the bounded Rankine vortex for $n = 1$. The curves are the energy decay for: $\hat{\zeta}_o = 1/r^3$ (dot), $\hat{\zeta}_o = 1/r^4$ (dash), $\hat{\zeta}_o = 1/r^5$ (dot dash), and $\hat{\zeta}_o = 1/r^6$ (dot dot dot dash).

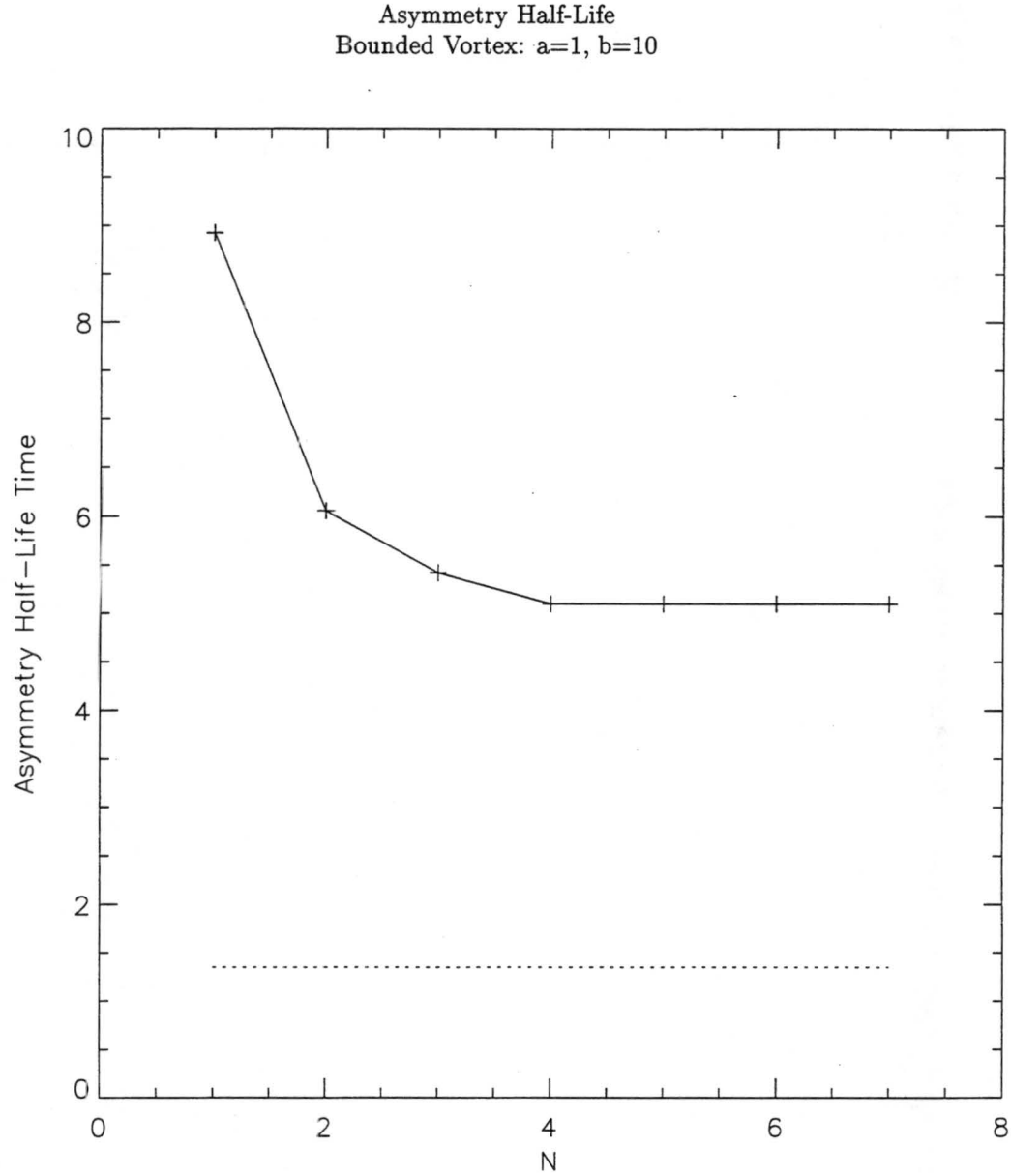

Fig. 4.9: Time required for an asymmetry to decay to half its initial energy as a function of wavenumber for $\hat{\zeta}_o = 1/r^2$. The dotted line is the limiting case given by $-1/S_{\text{eff}}$ where $S_{\text{eff}} = -0.74$.

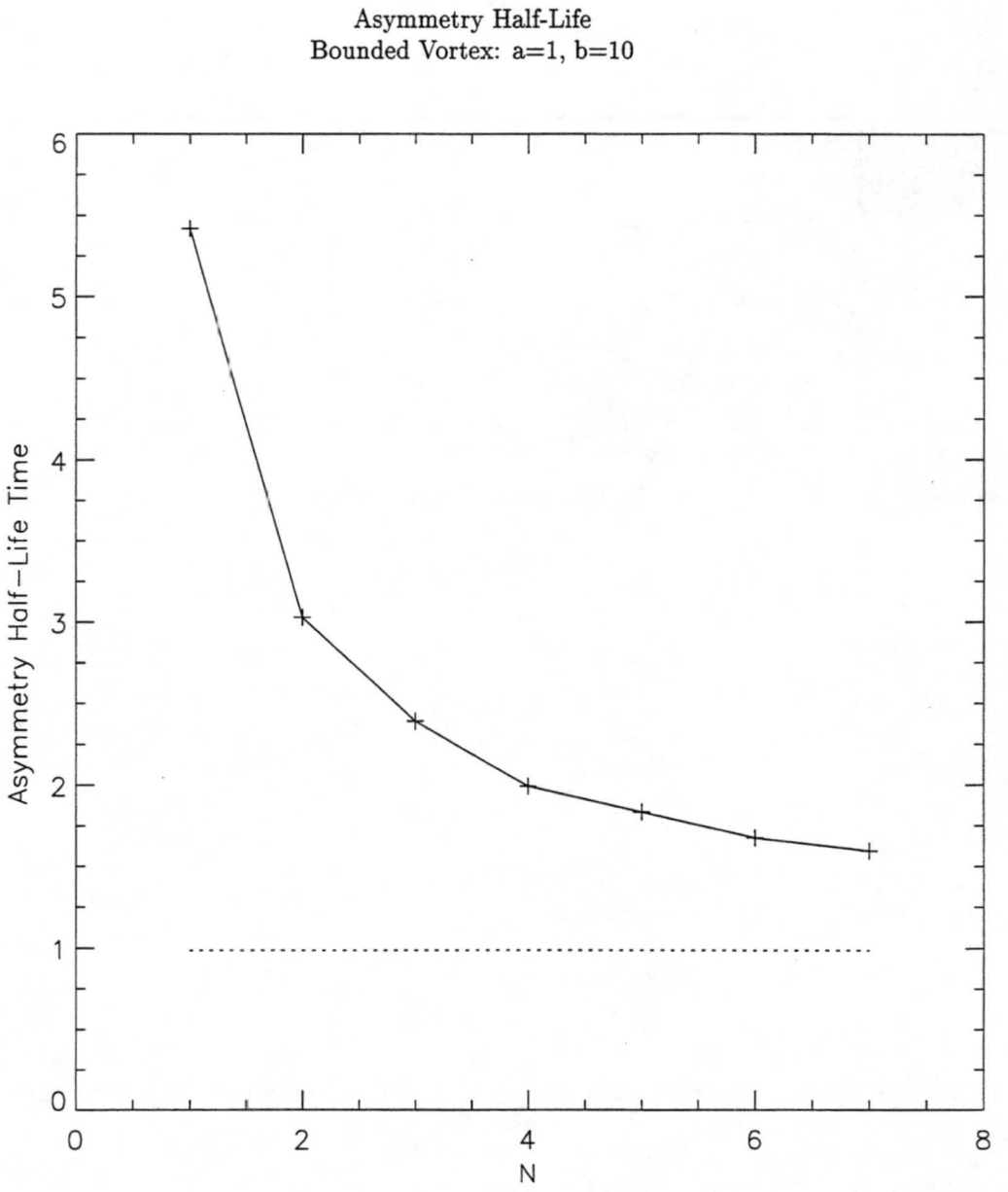

Fig. 4.10: Same as figure 4.9 except $\hat{\zeta}_o = 1/r^3$ and $S_{\text{eff}} = -1.01$.

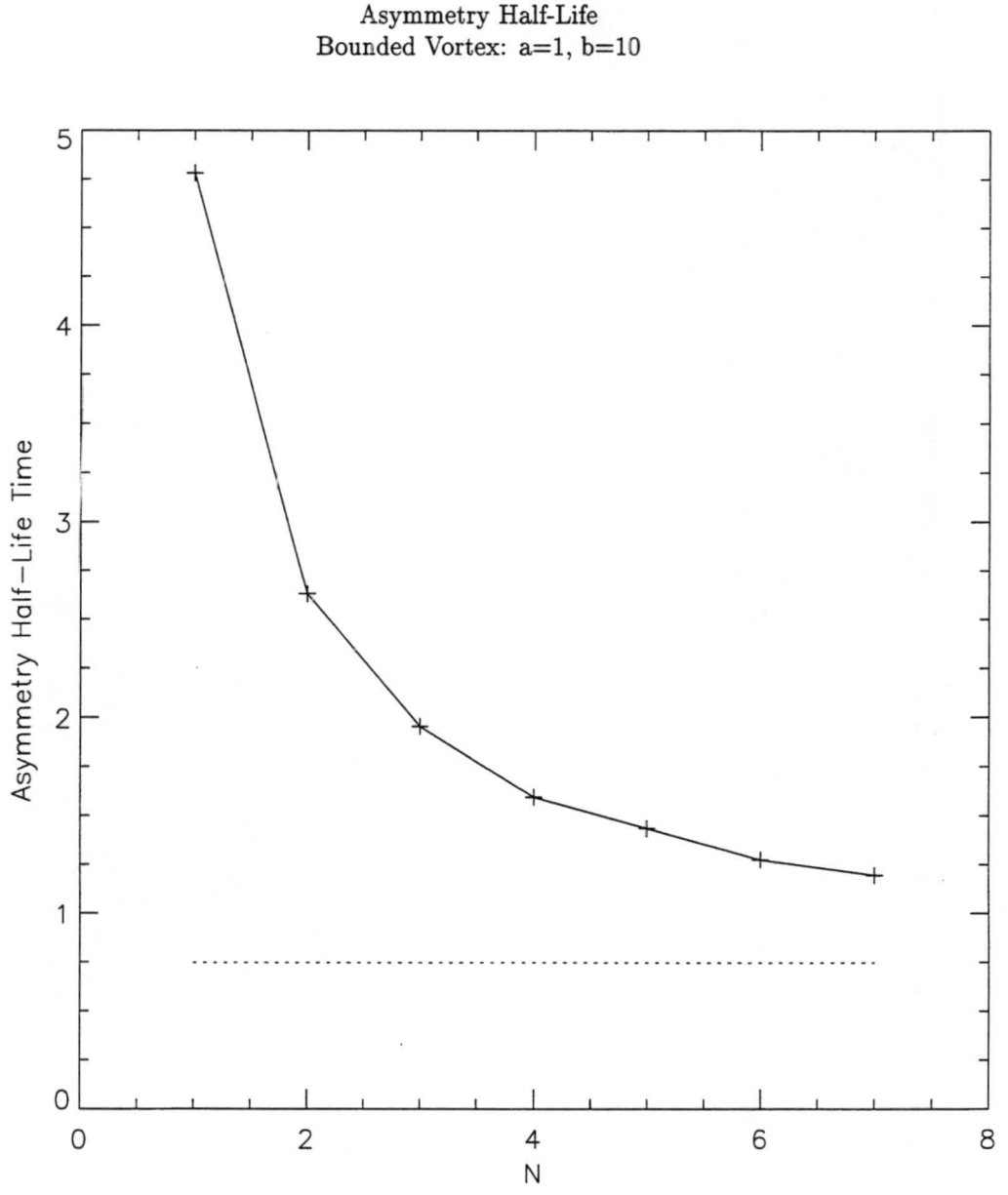

Fig. 4.11: Same as figure 4.9 except $\hat{\zeta}_o = 1/r^5$ and $S_{\text{eff}} = -1.34$.

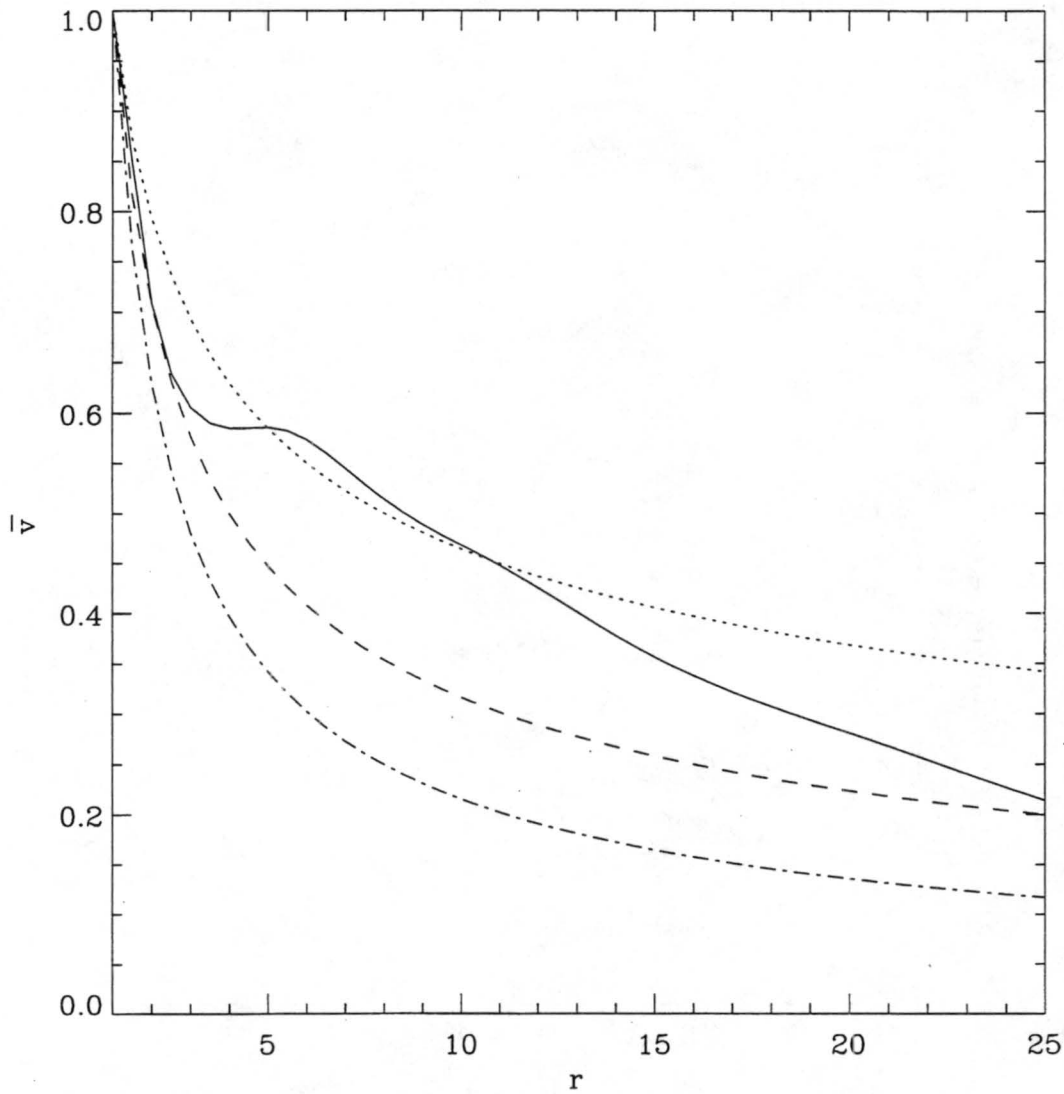

Fig. 4.12: The nondimensionalized Gloria and analytical tangential wind profiles. The analytical winds are given by $\bar{v} = 1/r^{\alpha}$ where $\alpha = 1/3$ (dot), $1/2$ (dash), and $2/3$ (dot dash).

CHAPTER 5

CONCLUSION

5.1 Summary

The inviscid nature of disturbance evolution in sheared flows has been investigated. The problem has been studied within the framework of nondivergent vorticity dynamics. Particular emphasis has been placed on understanding the wavenumber and spatial structure dependencies in perturbation evolution.

A truly inviscid mechanism which favors the decay of high wavenumber perturbations over low wavenumber perturbations was identified. Further, the wavenumber one perturbation decayed significantly slower than all other perturbations. In the development of AB theory, SM appealed to both observational and computational evidence of a wavenumber selection mechanism as the basis for the theory. The results presented here further elucidate the wavenumber selection mechanism and provide further theoretical support for the validity of AB theory.

The spatial structure of the initial conditions was shown to play a significant role in disturbance evolution. The spatial scale controlled how rapidly a disturbance sheared and subsequently decayed. In the swirling problem, the radial location of the initial condition was an important consideration as the shear decreased from the radius of maximum winds. These factors led to the definition of an effective shear which accounted for the interaction of the symmetric basic state and the initial vorticity profile. As defined here, the effective shear was shown to be an adequate estimate for the higher wavenumbers as long as the radial variation of the initial condtion was greater than that of the symmetric basic state. However, the effective shear was a significant underestimate for the lower wavenumbers.

Using the effective shear, decay half-life times were estimated on a wavenumber by wavenumber

basis. The results clearly demonstrated that the decay half-life times do not decrease as $1/n^2$ which refuted the CW assertion that the damping rate is proportional to the square of the azimuthal wavenumber. The effective half-life times for wavenumber one were found to be approximately seven times slower than those forecast by the effective shear. This was used to estimate half-life times for tangential wind profiles that are more representative of hurricanes outside their radius of maximum winds. These half-life times seemed to be reasonable estimates for the asymmetric forcings simulated.

5.2 Suggested Further Work

The wind profiles considered did not have a basic state vorticity gradient and, thus, excluded discrete normal modes from the solution set. While the interaction of the continuous spectrum and the discrete normal modes has been considered for the Eady model (Pedlosky, 1964; Farrell, 1984), this topic requires further investigation in rapidly rotating vortices. An analytical method that extends the Rankine vortex into a uniformly rotating core is briefly considered in Appendix A. In addition, a basic state vorticity gradient may be viewed as an effective vortex β. CW suggested that this effective β would introduce a retrogression that could counteract the rate of perturbation tilting induced by the differential rotation. Further work is needed to examine this hypothesis.

Sutyrin characterized the transfer of energy from the azimuthal perturbations to the circularly symmetric basic state as being analogous to the energy cascade to larger scales in two-dimensional turbulence. Moreover, he associated the growth of the basic state potential vorticity gradient with the transfer of enstrophy to smaller scales. These ideas merit further investigation and quantification.

APPENDIX A

AXISYMMETRIZATION IN UNBOUNDED RANKINE FLOW

In this appendix, the asymmetric dynamics of an unbounded Rankine vortex are briefly considered. The nondimensional linearized vorticity equation from chapter 4 is again used to represent the system. The inner boundary is now at the origin while the outer boundary is removed to infinity. It is assumed that all quantities are bounded at the origin and vanish at infinity.

When including the region inside the radius of maximum winds, the Rankine profile is given by

$$\bar{v} = \begin{cases} r/a, & r \leq a; \\ a/r, & r \geq a; \end{cases} \tag{A.1}$$

where a is the nondimensional radius of maximum winds and r is the nondimensional radius. The corresponding basic state vorticity profile is

$$\bar{\zeta} = \begin{cases} 2/a, & r < a; \\ 0, & r > a; \end{cases} \tag{A.2}$$

while the absolute vorticity profile is given by

$$\bar{\eta} = \begin{cases} R_o^{-1} + 2/a, & r < a; \\ R_o^{-1}, & r > a. \end{cases} \tag{A.3}$$

The quantity R_o^{-1} is the inverse Rossby number defined by $R_o^{-1} = fR_m/V_m$ where f is the Coriolis parameter and V_m is the symmetric wind at the radius of maximum winds (R_m). Figure A.1 shows $\bar{v}$ and $\bar{\eta}$ for the full Rankine vortex.

The discontinuity in the mean state vorticity at $r = a$ effectively introduces another boundary to the system. Since this boundary is interior to the fluid, the kinematic and dynamic boundary conditions must be satisfied at the disturbed interface $r = a+\epsilon$, where ϵ is the interface displacement. The kinematic boundary condition requires that the normal velocity be continuous while the dynamic boundary condition requires that the pressure be continuous at $r = a + \epsilon$, respectively. Consistent

with the linearization employed below the matching conditions will be evaluated at $r = a$. The evolution of the disturbed interface may still be determined by integrating

$$\left(\frac{\partial}{\partial t} + \frac{\bar{v}}{r}\frac{\partial}{\partial \lambda}\right)\epsilon = u' \tag{A.4}$$

at $r = a$ once u' is found.

For the full Rankine profile (A.2) the linearized vorticity equation of chapter 4 is modified to

$$\left(\frac{\partial}{\partial t} + \frac{\bar{v}}{r}\frac{\partial}{\partial \lambda}\right)\zeta = 0, \qquad r \neq a. \tag{A.5}$$

To solve (A.5), the discontinuity in the basic state vorticity at $r = a$ must be accounted for. Since the problem is linear, the superposition principle may be used to decompose the solution into two parts by letting $\zeta = \zeta_s + \zeta_1$ where ζ_s is defined to be smooth for all r and ζ_1 accounts for the discontinuity in the basic state vorticity at $r = a$. The vorticity equation (A.5) is then split into two parts

$$\left(\frac{\partial}{\partial t} + \frac{\bar{v}}{r}\frac{\partial}{\partial \lambda}\right)\zeta_s = 0, \qquad \forall r; \tag{A.6a}$$

$$\left(\frac{\partial}{\partial t} + \frac{\bar{v}}{r}\frac{\partial}{\partial \lambda}\right)\zeta_1 = 0, \qquad r \neq a. \tag{A.6b}$$

Equation (A.6a) is formally identical to the system solved in chapter 4, but with the boundary conditions cited above. The corresponding solution in Fourier space is

$$\hat{\psi}_s(r,t) = \int_0^\infty G(r,\rho)\hat{\zeta}_{so}(\rho)e^{-in\bar{v}t/\rho}\,\rho d\rho \tag{A.7}$$

where the appropriate Green's function is

$$G(r,\rho) = -\frac{1}{2n}\begin{cases} \rho^{-n}r^n, & 0 \leq r \leq \rho \\ \rho^n r^{-n}, & \rho \leq r < \infty, \end{cases} \tag{A.8}$$

and $\hat{\zeta}_{so}(\rho)$ is the smooth component of $\hat{\zeta}$ at time $t = 0$.

The Fourier space equivalent to (A.6b) is

$$\left(\frac{\partial}{\partial t} + \frac{in\bar{v}}{r}\right)\hat{\zeta}_1 = 0, \qquad r \neq a. \tag{A.9}$$

Anticipating that the solution to ($A.9$) will yield the discrete normal modes which are irrotational on both sides of the discontinuity, $\hat{\zeta}_1$ is assumed separable of the form

$$\hat{\zeta}_1 = \gamma(t)\delta(r-a). \tag{A.10}$$

Here, γ is an undetermined temporal multiplier for $\hat{\zeta}_1$ and $\delta(r-a)$ is the Dirac delta function. In terms of the streamfunction, equation ($A.10$) is written

$$\nabla^2\hat{\psi}_1 = \gamma(t)\delta(r-a). \tag{A.11}$$

The streamfunction is also assumed separable of the form $\hat{\psi}_1 = \gamma(t)\hat{\Psi}_1(r)$. Thus, equation ($A.11$) becomes

$$\left(\frac{d^2}{dy^2} - k^2\right)\hat{\Psi}_1 = \delta(r-a). \tag{A.12}$$

For $r \neq a$, equation ($A.12$) is Euler's equation. Two conditions are needed to match the solutions in each region across $r = a$. The first is the kinematic boundary condition requiring that the radial velocity, u, be continuous at $r = a$. Thus, the Fourier streamfunction amplitude must be continuous across $r = a$. The second condition results from integrating ($A.12$) over a small interval that includes $r = a$. This yields the following jump condition for $\hat{\Psi}_1$

$$\frac{\partial\hat{\Psi}_1}{\partial r}(a^+) - \frac{\partial\hat{\Psi}_1}{\partial r}(a^-) = 1. \tag{A.13}$$

Applying the boundary conditions, and the continuity and jump conditions at $r = a$, yields

$$\hat{\Psi}_1 = -\frac{a}{2n}\begin{cases} a^{-n}r^n, & 0 \leq r \leq a \\ a^n r^{-n}, & a \leq r < \infty. \end{cases} \tag{A.14}$$

To complete the derivation, γ must be determined. The remaining constraint is the dynamic boundary condition which requires that the pressure be continuous at $r = a$. In Fourier space, the azimuthal momentum equation is given by

$$\frac{\partial\hat{v}}{\partial t} + \frac{in\bar{v}}{r}\hat{v} + \bar{\eta}\hat{u} = -\frac{in}{r}\hat{p}. \tag{A.15}$$

Evaluating ($A.15$) on each side of $r = a$ and subtracting gives

$$\frac{\partial}{\partial t}[\hat{v}(a^+) - \hat{v}(a^-)] + \frac{in}{a}[\hat{v}(a^+) - \hat{v}(a^-)] - \frac{2}{a}\hat{u}(a) = 0. \tag{A.16}$$

In terms of the total streamfunction, equation ($A.16$) becomes

$$\frac{\partial}{\partial t}\left[\frac{\partial\hat{\psi}}{\partial r}(a^+)-\frac{\partial\hat{\psi}}{\partial r}(a^-)\right]+\frac{in}{a}\left[\frac{\partial\hat{\psi}}{\partial r}(a^+)-\frac{\partial\hat{\psi}}{\partial r}(a^-)\right]+\frac{2in}{a^2}\hat{\psi}(a)=0. \tag{$A.17$}$$

Now, from the superposition principle, $\hat{\psi}=\hat{\psi}_s+\gamma\hat{\Psi}_1$, where $\hat{\psi}_s$ and its derivatives are everywhere smooth by construction. Since $\hat{\Psi}_1$ is continuous but has a unit jump in its derivative across $r=a$, equation ($A.17$) simplifies to

$$\frac{d\gamma}{dt}+\frac{i}{a}(n-1)\gamma=-\frac{2in}{a^2}\hat{\psi}_s(a,t), \tag{$A.18$}$$

a first-order linear differential equation for γ. Upon multiplying through by the integrating factor $\exp[i(n-1)t/a]$ and substituting for $\hat{\psi}_s(a,t)$, equation ($A.18$) becomes

$$\frac{d}{dt}\left[\gamma e^{i(n-1)t/a}\right]=-\frac{2in}{a^2}\int_0^\infty G(a,\rho)\hat{\zeta}_{so}e^{[i(n-1)/a-in\bar{v}/\rho]t}\,\rho d\rho. \tag{$A.19$}$$

Integrating in time and then multiplying through by $\exp[-i(n-1)t/a]$ gives

$$\gamma(t)=-\frac{2n}{a}\int_0^\infty\frac{G(a,\rho)\hat{\zeta}_{so}}{(n-1-an\bar{v}/\rho)}e^{-in\bar{v}t/\rho}\,\rho d\rho+c_1e^{-i(n-1)t/a} \tag{$A.20$}$$

where c_1 is the constant of integration at $t=0$. Equation ($A.20$) then yields

$$\begin{aligned}\gamma(t)=&-\frac{2n}{a}\int_0^\infty\frac{G(a,\rho)\hat{\zeta}_{so}}{(n-1-an\bar{v}/\rho)}e^{-in\bar{v}t/\rho}\,\rho d\rho\\&+\left[\gamma_o+\frac{2n}{a}\int_0^\infty\frac{G(a,\rho)\hat{\zeta}_{so}}{(n-1-an\bar{v}/\rho)}\,\rho d\rho\right]e^{-i(n-1)t/a}\end{aligned} \tag{$A.21$}$$

where γ_o is the initial amplitude of the normal-mode (Rossby) wave. The Fourier streamfunction amplitude, $\hat{\psi}$, is thus

$$\begin{aligned}\hat{\psi}=&\int_0^\infty G(r,\rho)\hat{\zeta}_{so}e^{-in\bar{v}t/\rho}\,\rho d\rho\\&+\hat{\Psi}_1\int_0^\infty\frac{G(a,\rho)\hat{\zeta}_{so}}{(n-1-an\bar{v}/\rho)}e^{-in\bar{v}t/\rho}\,\rho d\rho\\&-\hat{\Psi}_1\left[\frac{a\gamma_o}{2n}+\int_0^\infty\frac{G(a,\rho)\hat{\zeta}_{so}}{(n-1-an\bar{v}/\rho)}\,\rho d\rho\right]e^{-i(n-1)t/a}.\end{aligned} \tag{$A.22$}$$

where G is given by ($A.8$) and $\hat{\Psi}_1$ is given by ($A.14$). To obtain the physical space streamfunction, the inverse Fourier transform must be applied to ($A.22$).

Equation ($A.22$) is interpreted as follows. The first line may be tentatively identified with the continuous spectrum solution and is the analogue of the solution presented in chapter 4. The second line is a conversion term that transfers some of the energy in the continuous spectrum solution into the discrete mode, which is the third line of the equation. Interestingly, even with no normal mode component initially ($\gamma_o = 0$), the continuous spectrum solution will always project onto the normal mode at later times (cf. Farrell, 1982). Note that for $n = 1$, the discrete mode does not rotate on the vortex, but rather represents the translation of the basic state vortex. For $n \neq 1$, the discrete modes rotate slower than the vortex and represent retrogressing Rossby waves at $r = a + \epsilon$.

Edwards (1994) demonstrated that this model can be extended to an arbitrary number of regions of constant basic state vorticity. Sutyrin (1989) developed the quasi-geostrophic shallow water equivalent of the multi-region model. However, his formulation did not explicitly describe the interaction between the continuous and discrete spectrum solutions. Extension of the above model to a quasi-geostrophic shallow water system is of interest as it may prove useful in idealized studies of hurricane track.

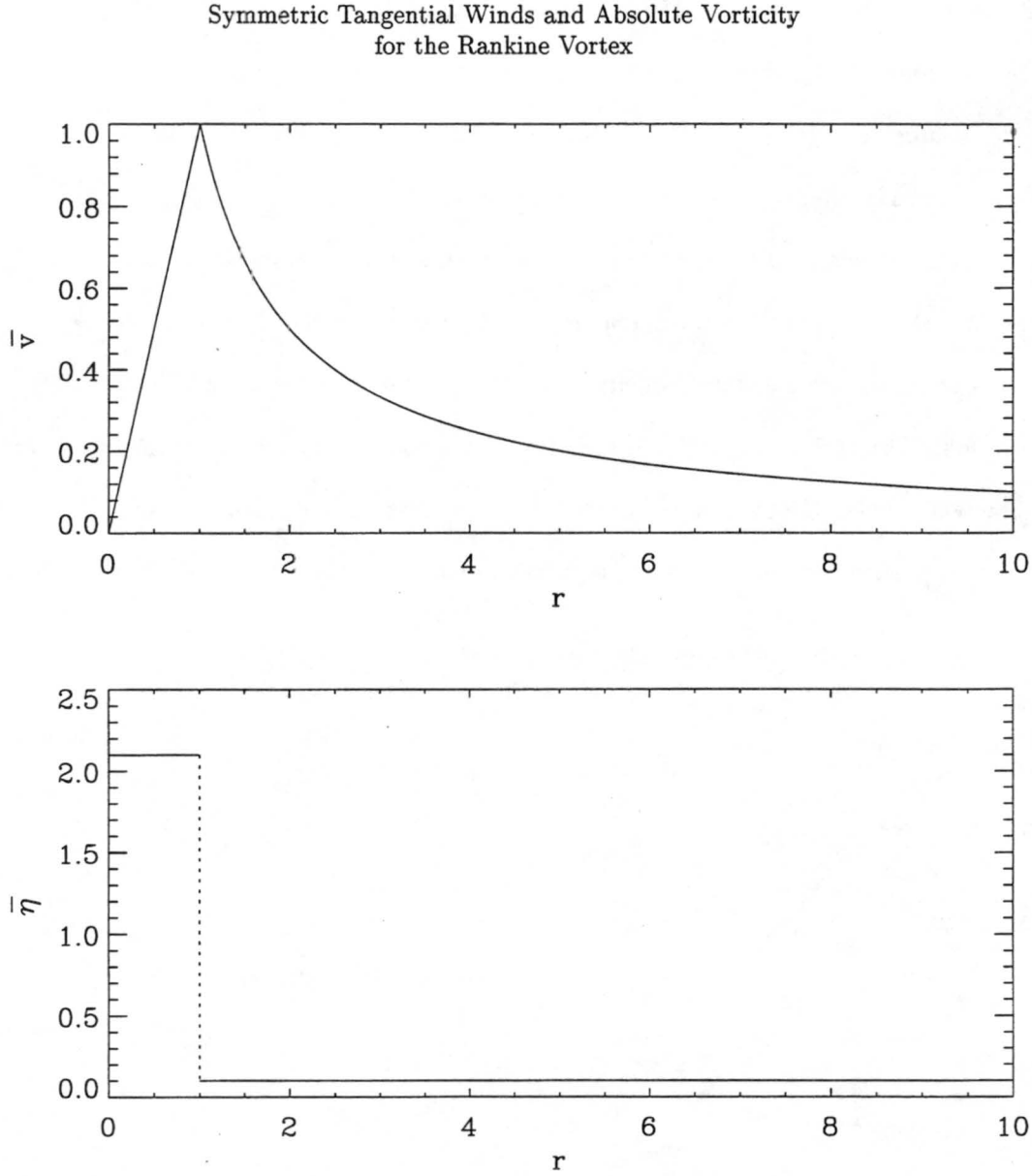

Figure A.1: Panel (a) shows the symmetric tangential winds for the full Rankine vortex. Panel (b) is the corresponding absolute vorticity using an inverse Rossby number of 0.1.

APPENDIX B

MODEL VERIFICATION

In this appendix, the verification of the numerical model is briefly considered. Since the meridional or radial disturbance scale generally changes with time, an estimate of when the disturbance scale becomes smaller than the model resolution is desired. In the rectilinear problem of chapter 2, the meridional wavenumber of an upright plane wave perturbation was found to be $l = -kSt$. Thus, a meridional wavelength was given by $2\pi/kSt$. Assuming the model resolves perturbations that have scales greater than or equal to twice the grid spacing, the model no longer resolves the perturbations when

$$\frac{2\pi}{kSt} \leq 2\Delta y \tag{B.1}$$

where Δy is the grid spacing, k is the zonal wavenumber, and S is the shear. Thus,

$$St \geq \frac{\pi}{k\Delta y} \tag{B.2}$$

gives an estimate of when the perturbations are no longer resolvable. In chapter 2 and 3, the worst model resolution was $\Delta y = 0.056$, corresponding to 361 grid points and integration limits at ± 10. For $k = 3$, the model resolution starts becoming inadequate for $St \approx 20$.

For the swirling problem, SM have shown that the change in the radial wavenumber with time is

$$\frac{dk}{dt} = -n\frac{d\bar{\Omega}}{dr}. \tag{B.3}$$

Here, k is the local radial wavenumber, n is the azimuthal wavenumber, and $\bar{\Omega}$ is the basic state angular velocity. For the Rankine profile $(A.1)$, equation $(B.3)$ is

$$\frac{dk}{dt} = -\frac{2n}{r^3}. \tag{B.4}$$

Thus, for a locally upright asymmetry

$$k = -\frac{2nt}{r^3}. \tag{B.5}$$

The model resolution, then, starts becoming inadequate when

$$\frac{2\pi}{k} \leq 2\Delta r \tag{B.6}$$

or, when

$$t \geq \frac{\pi r^3}{2n\Delta r}. \tag{B.7}$$

In chapter 4, the worst model resolution was $\Delta r = 0.05$, corresponding to boundaries $a = 1$ and $b = 10$ with 181 grid points. Thus, at the radius of maximum winds for $n = 3$, the asymmetries start becoming smaller than the model resolution when $t \approx 10$. However, at $r = 5$ and $n = 3$, the asymmetries start becoming unresolvable when $t \approx 1300$.

To be consistent with the analytical system, the model results must satisfy the momentum equations to within discretization error. Since the trapezoidal rule was used in this work, the discretization error should be proportional to the model resolution squared, i.e., model output must be at least quadratically convergent. The procedure used to evaluate the model output for the swirling problem is briefly presented below.

For the bounded Rankine vortex ($B4.18$), model verification was performed with the Fourier space representation of the momentum equations ($B4.8a$) and ($B4.8b$)

$$\frac{\partial \hat{u}}{\partial t} + \frac{in}{r^2}\hat{u} - \bar{\xi}\hat{v} = -\frac{\partial \hat{p}}{\partial r}, \tag{B.8a}$$

$$\frac{\partial \hat{v}}{\partial t} + \frac{in}{r^2}\hat{v} + \bar{\eta}\hat{u} = -\frac{in}{r}\hat{p}. \tag{B.8b}$$

From ($B.8b$), $\hat{p}$ was found for all radial values at a fixed time. Using centered difference approximations for all differentiated quantities, the radial gradient of $\hat{p}$ was calculated and compared to the left side of ($B.8a$). For the shear-induced asymmetry from CW ($\hat{\zeta}_o = -i/r^2, \quad n = 2$) and model resolutions of $\Delta r = \Delta t = 5 \times 10^{-2}$ at $t = 9$, the difference between the left and right sides of ($B.8a$) at $r = 2.3$ was -2.54×10^{-5}. For double and quadruple the above model resolution, the difference was -6.34×10^{-6} and -1.59×10^{-6}, respectively. In each case, as the model resolution doubled, the difference decreased by a factor of 4. For the same model resolutions at $r = 1.7$ and $t = 5.9$, the differences were 9.02×10^{-6}, 2.01×10^{-6}, and 4.87×10^{-7}, respectively. The model output was

checked for a variety of times, radial locations, and initial vorticity profiles. In all cases, the model output was found to be quadratically convergent.

REFERENCES

Carr, L. E. III, and R. T. Williams, 1989: Barotropic vortex stability to perturbations from axisymmetry. *J. Atmos. Sci.*,**46,** 3177-3191.

Case, K. M., 1960: Stability of inviscid plane Couette flow. *Phys. Fluids,* **3,** 143-148.

Edwards, J. P., 1994: Barotropic instability in the inner core of tropical cyclones. Atmospheric Science Paper No. 552, Colorado State University, Fort Collins, CO.

Eliassen, A., 1951: Slow thermally or frictionally controlled meridional circulation in a circular vortex. *Astrophys. Norv.,* **5,** 19-60.

Farrell, B., 1982: The initial growth of disturbances in a baroclinic flow. *J. Atmos. Sci.,* **39,** 1663-1686.

Farrell, B., 1984: Modal and non-modal baroclinic waves. *J. Atmos. Sci.,* **41,** 668-673.

Farrell, B., 1987: Developing disturbances in shear. *J. Atmos. Sci.,* **40,** 2191-2199.

Guinn, T. A. and W. H. Schubert, 1993: Hurricane spiral bands. *J. Atmos. Sci.,* **50,** 3380-3403.

McCalpin, J. D., 1987: On the adjustment of azimuthally perturbed vortices. *J. Geophys. Res.,* **92,** 8213-8225.

Melander, M. V., J. C. McWilliams, and N. J. Zabusky, 1987: Axisymmetrization and vorticity-gradient intensification of an isolated two-dimensional vortex through filamentation. *J. Fluid Mech.,* **178,** 137-159.

Molinari, J., 1992: Environmental controls on eye wall cycles and intensity change in Hurricane Allen (1980). *ICSU/WMO International Symposium on Tropical Cyclone Disasters,* October 12-16, 1992, Beijing, 328-337.

Pedlosky, J., 1964: An initial-value problem in the theory of baroclinic instability. *Tellus,* **16,** 12-17.

Shapiro, L. J., and K. V. Ooyama, 1990: Barotropic vortex evolution on a beta plane. *J. Atmos. Sci.,* **47,** 170-187.

Shapiro, L. J., 1992: Hurricane vortex motion and evolution in a three-layer model. *J. Atmos. Sci.,* **49,** 140-153.

Shapiro, L. J., and M. T. Montgomery, 1993: A three-dimensional balance theory for rapidly rotating vortices. *J. Atmos. Sci.,* **50,** 3322-3335.

Smith, R. K., and H. C. Weber, 1993: An extended analytic theory of tropical-cyclone motion in a barotropic shear flow. *Quart. J. Roy. Meteor. Soc.,* **119,** 1149-1166.

Sutyrin, G. G., 1989: Azimuthal waves and symmetrization of an intense vortex. *Sov. Phys. Dokl.*, **34,** 104-106.

Willoughby, H. E., 1977: Inertia-buoyancy waves in hurricanes. *J. Atmos. Sci.*, **34,** 1028-1039.

Willoughby, H. E., 1979: Excitation of spiral bands in hurricanes by interaction between the symmetric mean vortex and a shearing environmental steering current. *J. Atmos. Sci.*, **36,** 1226-1235.

Willoughby, H. E., 1988: Linear motion of a shallow-water, barotropic vortex. *J. Atmos. Sci.*, **45,** 1906-1928.